

**Scanning Tunneling Microscopy
Studies on Model Systems Relevant
for Heterogeneous Catalysis**



**Stig Helveg
Institute of Physics and Astronomy
University of Aarhus, Denmark**

Scanning Tunneling Microscopy
Studies on Model Systems Relevant
for Heterogeneous Catalysis

Stig Helveg

July 2000

Preface

This thesis is submitted to the Faculty of Science, University of Aarhus, Denmark, in order to fulfil the requirements for obtaining the PhD degree in physics. The experimental work presented was carried out in the scanning tunneling microscopy (STM) group at the Institute of Physics and Astronomy from the summer of 1996 to the summer of 2000.

Throughout this period, a large number of people has been involved, directly or indirectly, in my work and their contributions are gratefully acknowledged. First of all, I would like to thank the three founders of the group: Flemming Besenbacher, for his ceaseless support, guidance and enthusiastic interest in my projects, Ivan Stensgaard, for numerous well-founded advices, and Erik Lægsgaard for his admirably ingenious technical solutions, which continuously improve the Århus STM.

In the work concerning adsorbates on the Pt(110)-(1×2) surface presented in chapter 3 and 4, the collaboration with Sebastian Horch on experiments and data-analysis is highly appreciated. Morten Schønning is acknowledged for his contributions to the investigations of the nanostructures in chapter 3. Recently, it has also been a pleasure to take part in Peter Thostrup's studies on surface reactions on Pt(110)-(1×2).

The hydrodesulfurization (HDS) model catalyst studies described in chapter 5 were initiated in the autumn of 1999. In this work, I have enjoyed very much a fruitful collaboration with Jeppe Vang Lauritsen, both in the laboratory and on the data-analysis. Also thanks to Anders Rønnau, who attended the project for a short period.

The interaction with the theory group at the Technical University of Denmark, headed by Jens K. Nørskov, has been very fruitful, and a close interplay between STM experiments and theoretical studies represent a cornerstone in the present work. It is therefore a great pleasure to acknowledge Henrik T. Lorentsen, for many contributions to the adsorption studies on Pt(110)-(1×2), and Line S. Byskov and Mikkel Bollinger for

their efforts on HDS model catalyst systems.

The HDS project is a result of a very stimulating interaction with the catalyst company Haldor Topsøe A/S. I would like to thank Bjerne S. Clausen and Henrik Topsøe for many good discussions and inputs to the experiments. Advices and ideas from Lars P. Nielsen are also acknowledged.

It has been a great pleasure to be part of the STM group. I would like to express my gratitude to the numerous people, who has passed the STM group in the time-period where I have been part of it, for contributing scientifically and socially to the unique, stimulating and enthusiastic atmosphere in the group. With some, the overlap has been more extensive and I would especially like to thank Kim Hansen, Kim Højrup Hansen, Trolle Linderøth, Morten Ø. Pedersen, Lars Petersen, Bernhard Schäfer, Ebbe Kruse Vestergaard and Lars Österlund for inspiring discussions and countless humorous remarks.

Finally, I am grateful to Jeanette Dandanell for correcting the thesis for linguistic errors and typos.

The STM group is part of the Center for Atomic-scale Materials Physics, which is funded by the Danish National Research Foundation. During the last two years my stipend has been financed jointly by the Danish Research Academy and Haldor Topsøe A/S through the Interdisciplinary Center for Catalysis (ICAT).

Stig Helveg
Århus, July 2000

List of Publications

In the thesis, the following references are referred to with capital roman numerals. Other references are cited using arabic numerals and are listed in the end of each section.

Publications related to the thesis

- [I] *Oxygen adsorption on Pt(110)-(1×2): new high-coverage structures.*
S. Helveg, H. T. Lorensen, S. Horch, E. Lægsgaard, I. Stensgaard, K. W. Jacobsen, J. K. Nørskov and F. Besenbacher. *Surface Science* **430**, L533 (1999).
- [II] *STM studies of oxygen adsorption on the Pt(110)-(1×2) surface.*
S. Helveg, S. Horch, E. Lægsgaard, I. Stensgaard, and F. Besenbacher. In preparation.
- [III] *The formation of oxygen nanostructures on Pt(110)-(1×2).*
S. Helveg, S. Horch, M. Schønning, E. Lægsgaard, I. Stensgaard, and F. Besenbacher. In preparation.
- [IV] *Enhancement of surface self-diffusion of platinum atoms by adsorbed hydrogen.*
S. Horch, H. T. Lorensen, S. Helveg, E. Lægsgaard, I. Stensgaard, K. W. Jacobsen, J. K. Nørskov and F. Besenbacher. *Nature* **398**, 134 (1999).
- [V] *Adsorbate-enhanced self-diffusion on Pt(110)-(1×2).*
S. Helveg, S. Horch, E. Lægsgaard, I. Stensgaard, and F. Besenbacher. In preparation.

- [VI] *Atomic-scale structure of single-layer MoS₂ nanoclusters.*
S. Helveg, J. V. Lauritsen, E. Lægsgaard, I. Stensgaard, J. K. Nørskov,
B. S. Clausen, H. Topsøe, and F. Besenbacher. *Physical Review Letters* **84**, 951 (2000).
- [VII] *STM studies of MoS₂ nanocrystals.*
S. Helveg, J. V. Lauritsen, E. Lægsgaard, I. Stensgaard, B. S. Clausen,
H. Topsøe, and F. Besenbacher. In preparation.
- [VIII] *Atomic-scale structure of CoMoS nanocrystals.*
J. V. Lauritsen, S. Helveg, E. Lægsgaard, I. Stensgaard, B. S. Clausen,
H. Topsøe, and F. Besenbacher. In preparation.

Other publications

- [IX] *How a gold substrate can increase the reactivity of a Pt overlayer.*
M. Ø. Pedersen, S. Helveg, A. Ruban, I. Stensgaard, E. Lægsgaard,
J. K. Nørskov and F. Besenbacher. *Surface Science* **426**, 395 (1999).
- [X] *Novel mechanism for diffusion of one-dimensional clusters:
Pt/Pt(110)-(1×2).*
T. R. Linderoth, S. Horch, L. Petersen, S. Helveg, E. Lægsgaard,
I. Stensgaard, F. Besenbacher. *Physical Review Letters* **82**, 1494
(1999).
- [XI] *Energetics and dynamics of Pt dimers on Pt(110)-(1×2).*
T. R. Linderoth, S. Horch, L. Petersen, S. Helveg, M. Schønning,
E. Lægsgaard, I. Stensgaard and F. Besenbacher. *Physical Review
B*, **61**, R2448 (2000).
- [XII] *Adsorption of CO on Pt(110)-(1×2).*
P. Thostrup, S. Helveg, E. Lægsgaard, I. Stensgaard and F. Besen-
bacher. In preparation.

Contents

Preface	i
List of Publications	iii
1 Introduction	1
1.1 Heterogeneous catalysis and STM	1
1.2 Outline of the thesis	4
2 Scanning Tunneling Microscopy	9
2.1 Principle of STM	9
2.2 STM theory	10
2.3 Experimental implementation	14
2.3.1 The Århus STM	14
2.3.2 Variable-temperature STM	17
2.3.3 STM movies	17
2.4 Concluding remarks	19
3 Adsorption: O/Pt(110)-(1×2)	23
3.1 Pt(110)-(1×2) and experimental details	24
3.2 Oxygen-induced surface structures	26
3.3 Atomic details of the oxygen structures	31
3.3.1 Experimental results	31
3.3.2 Theoretical results	38
3.3.3 A coherent picture of O/Pt(110)-(1×2)	42
3.3.4 Comparison with other studies	45
3.3.5 Stabilizing high-coverage structures	47
3.4 The self-assembled oxygen nanostructure	51
3.4.1 Experimental results	51
3.4.2 Discussion	58

3.5	Summary and outlook	61
4	Adsorbate-enhanced self-diffusion	69
4.1	Self-diffusion on Pt(110)-(1×2)	70
4.2	H-enhanced self-diffusion on Pt(110)	73
4.2.1	Experimental details	75
4.2.2	Experimental results	76
4.2.3	Discussion	81
4.3	O-enhanced self-diffusion on Pt(110)	87
4.4	Summary and outlook	89
5	HDS model catalysts	95
5.1	Hydrodesulfurization catalysis	96
5.1.1	Hydrodesulfurization process	96
5.1.2	Catalyst structure	98
5.2	MoS ₂ nanoclusters	102
5.2.1	Experimental details	102
5.2.2	Preparation of MoS ₂ nanoclusters	104
5.2.3	Characterisation	110
5.2.4	Morphology	113
5.2.5	Edge structures	120
5.2.6	Conclusion	126
5.3	Edge vacancies	126
5.3.1	Sulfur vacancy formation and structure	126
5.4	CoMoS nanoclusters	129
5.4.1	Preparation of CoMoS nanoclusters	130
5.4.2	Cluster structures	130
5.4.3	Model for the CoMoS clusters	133
5.5	Summary and outlook	137
6	Danish summary	145

Chapter 1

Introduction

With the advent of the scanning tunneling microscope (STM) in the 1980s, scientists now have a tool to directly image surfaces with atomic resolution. This has provided unprecedented new insight into surface science and related research areas, such as condensed matter physics, chemistry, biology, materials science and nanotechnology [1, 2]. The STM studies presented in this thesis address three different topics of fundamental relevance for heterogeneous catalysis. The larger context to which these studies belong and an outline of the investigations are given in this introductory chapter.

1.1 Heterogeneous catalysis and STM

Catalysis plays an almost ubiquitous role in chemical industries and oil refineries and is assuming an increasing interest in areas like environmental protection, biotechnology, power production, agrochemistry and pharmacy. Many of the major problems encountered in modern society, including the reduction polluting emissions and a better use of fossil fuels, require solutions in which new and optimized catalysts play an important role. The vital impact of catalysis on society is perhaps best illustrated by the fact that catalysis is involved in 10-15% of the gross national products in the industrialized countries [3-5].

In the vast majority of these applications, the chemical transformation of reactants in a gas (liquid) phase is catalyzed heterogeneously at solid surfaces. Whereas the catalyst technology has been well-established for decades, it is only recent progress in surface science which has opened up for the attainment of a detailed molecular level understanding of the

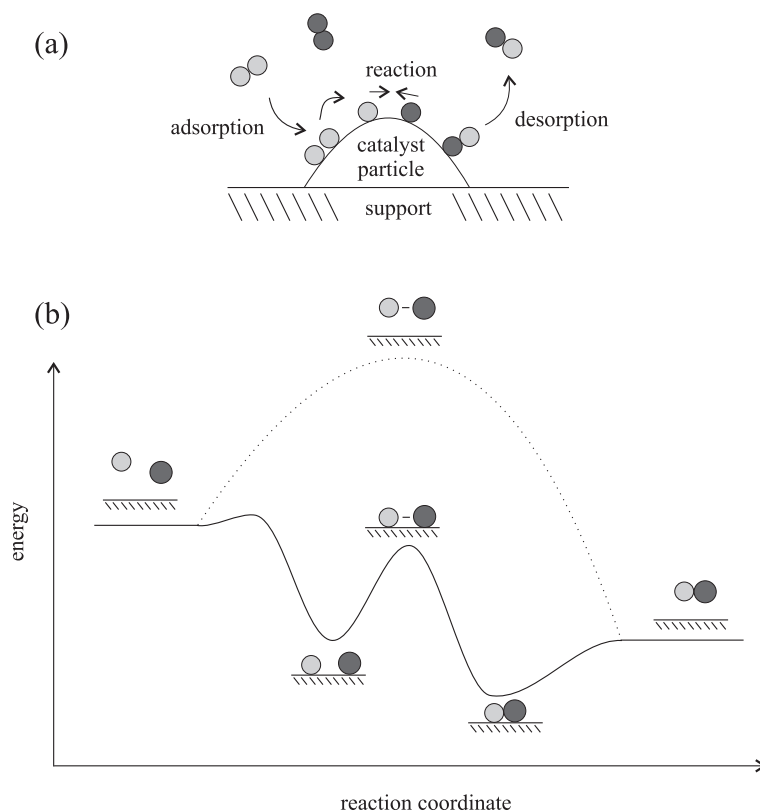


Figure 1.1: (a) A sketch of elementary processes in the gas-surface interaction at the surface of a supported catalyst particle. (b) The free energy diagram for the sketched reaction. The dotted curve shows the free energy as a function of reaction coordinate for the reaction in the gas phase, and the full curve shows the free energy for the reaction at the surface. The surface catalyzes the reaction since the energy barriers are lower along the path on the surface than for gas phase reaction.

gas-surface interactions involved in catalytic reactions.

The catalytical processes typically occur in flow reactors when reactants pass through. Often, the reaction conditions are extreme with total pressures up to several hundreds bars and temperatures of some hundreds degrees Celsius. The heterogeneous catalysts used in today's technologies

are typically very complex materials consisting of porous pellets of a high surface area ($\sim 100\text{ m}^2/\text{g}$) oxide support, onto which the catalytically active material (e.g. a metal) is dispersed in nanometer-sized particles. This complexity of the catalyst systems hampers a detailed characterization of the elementary processes and explains why catalyst developments and improvements are largely based on “trial and error” experimentations [3, 4].

In the general picture of a catalytic reaction, the reactants are offered an alternative and more rapid path to the final products by the catalyst surface (figure 1.1). The overall process usually consists of a series of elementary steps including the adsorption of reactants on the catalyst surface, breaking of some adsorbate bonds, adsorbate diffusion and reaction to form products, which eventually desorb from the surface. The activation energy barriers for the separate steps in the catalyzed reaction are all significantly lower than for the uncatalyzed reaction, which is the reason for the increase in the reaction rate [6].

To obtain a detailed description and understanding of such processes, scientists approach heterogeneous catalysis by well-characterized model systems. The active parts of the catalysts are usually represented by single-crystal surfaces kept under ultrahigh vacuum conditions (corresponding to a pressure $\sim 1 \times 10^{-10}$ mbar). This allows clean model catalyst surfaces to be prepared, to be exposed to gases of well-defined composition and to be characterized by a multitude of surface-sensitive analytical techniques [7]. This fundamental and highly idealized surface science approach has provided much valuable information about heterogeneously catalyzed reactions [3, 4], and it has been demonstrated that insight gained from such studies can be applied to guide the catalyst development [8]. Currently, this stimulates very lively activities in the field.

Among the surface-sensitive techniques, STM has become an indispensable tool due to its exceptionally high real-space resolution. Lately, STM has provided many new and fascinating discoveries regarding gas-surface interactions, including information about adsorbate binding sites and structures [9–12], quantitative information about diffusion of adsorbates [13–19] and their mutual interaction [20, 21], direct views of active sites for surface chemical reactions and determinations of reaction mechanisms on the atomic scale [22–29]. Furthermore, STM is also a very promising tool in the attempts to bridge the material gap and pressure gap that exist between the model systems in ultrahigh vacuum environments and the real catalysts. It has very recently been shown that insight into the morphology and the detailed atomic-scale structure of nanoclusters deposited on suitable flat model supports [30–32] can be obtained, even *in situ* under

higher pressures up to ~ 1 bar [33, 34]. It should be added, that in several occasions these contributions have, however, only become possible by an interplay with other surface science techniques.

The studies presented in this thesis address some fundamental questions utilizing STM to monitor atomic-scale structures and dynamic processes on model catalyst surfaces. The work should therefore be seen as a part of the unified efforts aiming at exploring the basics for heterogeneous catalysis.

1.2 Outline of the thesis

The thesis is structured in the following way:

Chapter 2 describes scanning tunneling microscopy. The basic theory of STM imaging is presented, and the experimental implementation used in the present studies is briefly described.

The chapters 3 to 5 cover STM studies of three different topics. These chapters are structured similarly and can be read independently. Each chapter is introduced by a short motivation for the topic in question. The experimental results are then presented and discussed. Finally, the main results are briefly summarized and an outlook is provided in the end.

Chapter 3 treats the dissociative adsorption of oxygen on the Pt(110)-(1 \times 2) surface. STM results are presented, and from an interplay with density functional theory (DFT) calculations, a comprehensive picture is obtained from single, isolated oxygen atoms to the formation of a new oxide-like structural element. It will be shown that these structures are stabilized by a strong coupling between the oxygen adsorption and distortions of the platinum lattice. Long-range interactions cause the oxide-like structures to spontaneously self-organize into a well-ordered nanostructure extending over a mesoscopic length scale. These results form the basis for further studies of simple surface chemical reactions.

In chapter 4, STM is used to explore the influence of co-adsorbed hydrogen on the diffusivity of Pt atoms deposited onto Pt(110)-(1 \times 2). The STM directly images Pt-H complexes with an increased diffusivity of two orders of magnitude. These are the first observations of a such complex formation, and the results explain in part why sintering and reshaping of dispersed catalyst particles are sensitive to the gas composition.

Chapter 5 describes a new way of obtaining atomic-scale information on hydrodesulfurization catalysts. A model system consisting of MoS₂ nanoclusters is synthesized on Au(111), and STM is used to scrutinize

their atomic-scale structure. The first images of catalytically active sites in the form of S vacancies at the cluster edges are presented, and the addition of Co promoter atoms to the MoS₂ clusters is investigated.

At the end of the thesis, a summary of the work is presented in Danish.

References

- [1] R. Wiesendanger, *Scanning Probe Microscopy and Spectroscopy* (Cambridge University Press, Cambridge, 1994).
- [2] *Scanning Probe Microscopy 1-3*, edited by R. Wiesendanger and H.-J. Güntherodt (Springer-Verlag, Berlin, 1995).
- [3] G. A. Somorjai, *Introduction to surface chemistry and catalysis* (John Wiley & Sons, Inc., New York, 1994).
- [4] *Handbook of Heterogeneous Catalysis*, edited by G. Ertl, H. Knözinger, and J. Weitkamp (VHC Verlagsgesellschaft mbH, Weinheim, Germany, 1997).
- [5] G. Ertl and H.-J. Freund, *Physics Today* **52**, 32 (1999).
- [6] R. A. van Santen and J. W. Niemantsverdriet, *Chemical Kinetics and Catalysis* (Plenum Press, New York, 1995).
- [7] H. Lüth, *Surfaces and Interfaces of Solid Materials* (Springer-Verlag, Berlin, 1995).
- [8] F. Besenbacher, I. Chorkendorff, B. S. Clausen, B. Hammer, A. M. Molenbroek, J. K. Nørskov, and I. Stensgaard, *Science* **279**, 1913 (1998).
- [9] P. J. Feibelman, S. Esch, and T. Michely, *Phys. Rev. Lett.* **77**, 2257 (1996).
- [10] M. Morgenstern, T. Michely, and G. Comsa, *Phys. Rev. Lett.* **77**, 703 (1996).
- [11] F. Besenbacher and J. K. Nørskov, *Prog. in Surf. Sci.* **44**, 5 (1993).
- [12] F. Besenbacher, *Rep. Prog. Phys.* **59**, 1737 (1996).
- [13] M. Ø. Pedersen, L. Österlund, J. J. Mortensen, M. Mavrikakis, L. B. Hansen, I. Stensgaard, E. Lægsgaard, J. K. Nørskov, and F. Besenbacher, *Phys. Rev. Lett.* **84**, 4898 (2000).
- [14] S. Renisch, R. Schuster, J. Wintterlin, and G. Ertl, *Phys. Rev. Lett.* **82**, 3839 (1999).
- [15] J. Wintterlin, R. Schuster, and G. Ertl, *Phys. Rev. Lett.* **77**, 123 (1996).

- [16] J. V. Barth, T. Zambelli, J. Wintterlin, R. Schuster, and G. Ertl, *Phys. Rev. B* **55**, 12902 (1997).
- [17] B. G. Briner, M. Doering, H.-P. Rust, and A. M. Bradshaw, *Phys. Rev. Lett.* **78**, 1516 (1997).
- [18] B. G. Briner, M. Doering, H.-P. Rust, and A. M. Bradshaw, *Science* **278**, 257 (1997).
- [19] U. Diebold, W. Hebenstreit, G. Leonardelli, M. Schmid, and P. Varga, *Phys. Rev. Lett.* **81**, 405 (1998).
- [20] L. Österlund, M. Ø. Pedersen, I. Stensgaard, E. Lægsgaard, and F. Besenbacher, *Phys. Rev. Lett.* **83**, 4812 (1999).
- [21] J. Trost, T. Zambelli, J. Wintterlin, and G. Ertl, *Phys. Rev. B* **54**, 17850 (1996).
- [22] T. Zambelli, J. Wintterlin, J. Trost, and G. Ertl, *Science* **273**, 1688 (1996).
- [23] J. Wintterlin, S. Völkening, T. W. Janssens, T. Zambelli, and G. Ertl, *Science* **278**, 1931 (1997).
- [24] S. Völkening, K. Bedürftig, K. Jacobi, J. Wintterlin, and G. Ertl, *Phys. Rev. Lett.* **83**, 2672 (1999).
- [25] W. W. Crew and R. J. Madix, *Surf. Sci.* **319**, L34 (1994).
- [26] R. A. Bennett, S. Poulston, and M. Bowker, *J. Chem. Phys.* **108**, 6916 (1998).
- [27] P. T. Sprunger, Y. Okawa, F. Besenbacher, I. Stensgaard, and K. Tanaka, *Surf. Sci.* **344**, 98 (1995).
- [28] I. Stensgaard, E. Lægsgaard, and F. Besenbacher, *J. Chem. Phys.* **103**, 9825 (1995).
- [29] H. Over, Y. D. Kim, A. P. Seitsonen, S. Wendt, E. Lundgren, M. Schmid, P. Varga, A. Morgante, and G. Ertl, *Science* **287**, 1474 (2000).
- [30] M. Bäumer and H.-J. Freund, *Prog. Surf. Sci.* **61**, 127 (1999).

- [31] K. H. Hansen, T. Worren, S. Stempel, E. Lægsgaard, M. Bäumer, H.-J. Freund, F. Besenbacher, and I. Stensgaard, *Phys. Rev. Lett.* **83**, 4120 (1999).
- [32] C. R. Henry, *Surf. Sci. Rep.* **31**, 231 (1998).
- [33] E. Lægsgaard, P. Thostrup, L.Österlund, P. B. Rasmussen, I. Stensgaard, and F. Besenbacher, in preparation.
- [34] J. Jensen, K. B. Rieder, M. Salmeron, and G. A. Somorjai, *Phys. Rev. Lett.* **80**, 1228 (1998).

Chapter 2

Scanning Tunneling Microscopy

The present chapter describes the basic principles and concepts of scanning tunneling microscopy (STM) as well as the instrumental implementation used in the STM group at the University of Aarhus [1]. A more extensive introduction to STM and to the many impressive areas of application can be found in several textbooks, e.g. [2–4].

2.1 Principle of STM

The principle behind the STM is strikingly simple. A sharp metallic tip (often tungsten) is brought into such close proximity ($z \sim 5 \text{ \AA}$) of a conducting sample that the conducting electrons obtain an appreciable probability for tunneling through the vacuum gap separating the two electrodes. For electrons at the Fermi level, the vacuum gap constitutes an energy barrier roughly corresponding to the average of the work functions of the tip and the sample and with a width determined by the tip-sample separation. By applying a bias voltage ($V_t \sim 1 \text{ mV} - 1 \text{ V}$) between the tip and the sample, the Fermi levels are shifted by a corresponding amount of energy, so that a net current is established of electrons tunneling from filled sample states into empty tip states, or vice versa, depending on the polarity of the bias voltage. The resulting tunnel current is of the order of $I_t \sim 1 \text{ nA}$ and has a strong (exponential) dependence on the tip-sample separation. As a rule of thumb, an increase in separation of 1 \AA results in to a drop in the

tunnel current of one order of magnitude. This is also the reason why one might reasonably expect to achieve atomic resolution in the STM. If e.g., a tip atom protrudes half a bond length further toward the surface than any other atoms in the tip, this apex atom will carry almost the entire tunnel current, and hence the tip is to be considered as a very localized probe.

Normally, STM imaging is done in the constant current mode. The tip is raster-scanned over the surface by means of a "piezo-robot" (figure 2.1). An electronic feedback circuit compares the actual tunnel current (I_t) with a preset value (I_0) and regulates the vertical height of the tip above the surface by adjusting the voltage applied to the z -translator on the piezo-robot to maintain the demanded tunnel current, as atoms, or more generally protrusions or depressions, are traversed. Recording the vertical height of the tip (or, in reality, the feedback signal) as a function of the lateral tip position during raster scanning yields the STM image of the surface.

2.2 STM theory

The interpretation of STM images requires a theoretical description of the tunneling process. Unlike the simple principle underlying STM, a detailed description of the STM images is extremely difficult, since the images represent a complicated convolution of the electronic structure of both the surface and the tip.

In principle, a calculation of the tunnel current requires knowledge about the electronic structure of both the tip and the surface as well as a description of the decaying electronic wave functions and the electron potential in the tunnel gap region. In general, this is a considerable task mainly due to the poorly characterized tip, but also because the interaction between the tip and the surface might be so pronounced that they have to be treated as one complete system and not as two separate and weakly interacting electrodes.

Several theoretical approaches have been developed in which various levels of approximations are used for calculating the tunnel current (see [5] for a review). Tersoff and Hamann (TH) [6, 7] have provided a simplified treatment based on the "pertubative-transfer Hamiltonian" approach developed by Bardeen [8].

The formalism by Bardeen applies to cases in which the interaction between the two electrodes is sufficiently weak to be neglected. The tunnel

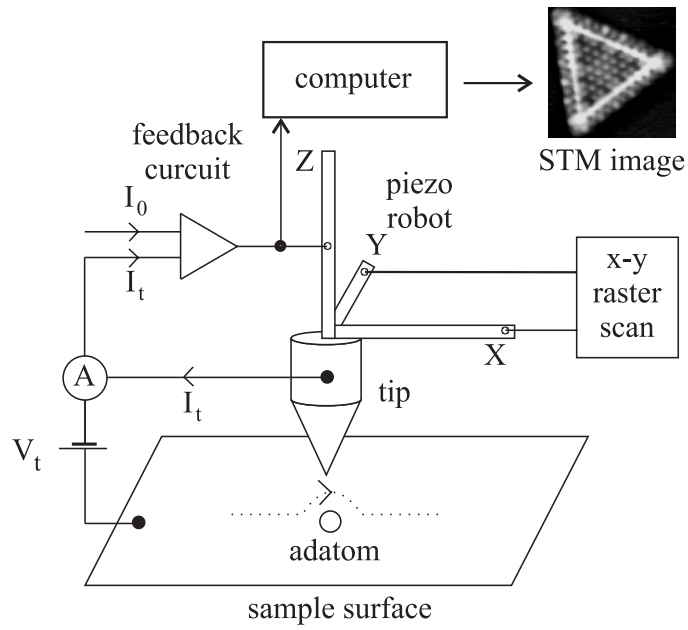


Figure 2.1: The operational principle of an STM. A robot constructed from piezoelectric ceramics raster-scans a sharp metallic tip across a conducting surface. The tunnel bias voltage is V_t . The feedback circuit compares the actual (I_t) and the preset value (I_0) of the tunnel current and adjusts the voltage applied to the z-translator on the robot to maintain the demanded current I_0 .

current is calculated from the overlap of the eigenfunctions ψ_μ and ψ_ν in the tunnel gap with the eigenenergies E_μ and E_ν for the tip and surface, respectively, evaluated for each electrode in absence of the other. Based on Fermi's golden rule, the tunnel current from the tip to the sample is obtained by summation over tip and sample states

$$I_t = \frac{2\pi e}{\hbar} \sum_{\mu\nu} f(E_\mu)[1 - f(E_\nu + eV_t)] |M_{\mu\nu}|^2 \delta(E_\mu - E_\nu), \quad (2.1)$$

where the Fermi-Dirac distributions, $f(E)$, take into account that tunneling occurs from filled tip states to empty sample states, and the delta function ensures elastic tunneling. The energy shift eV_t results from the tunnel bias voltage V_t between the tip and the sample. The tunnel matrix element $M_{\mu\nu}$ is given by the current density integrated over a surface, S_0 , lying entirely within the tunnel gap region

$$M_{\mu\nu} = \frac{\hbar^2}{2m} \int_{S_0} d\mathbf{S} (\psi_\mu^* \nabla \psi_\nu - \psi_\nu \nabla \psi_\mu^*), \quad (2.2)$$

where $*$ means complex conjugation. To calculate the tunnel matrix element, Tersoff and Hamann model the tip with a spherical symmetric s -type wave function centred on a point \vec{r}_0 . In the limit of low temperatures and bias voltages, the total tunnel current is then expressed as

$$I_t \propto V_t \sum_{\nu} |\psi_\nu(\vec{r}_0)|^2 \delta(E_\nu - E_F), \quad (2.3)$$

in which the sum extends over sample states, ψ_ν , evaluated at \vec{r}_0 , and the delta function ensures that only states at the Fermi level contribute.

The expression shows that the tunnel current is proportional to the local density of states (LDOS) of the sample at the Fermi level evaluated at the tip centre \vec{r}_0 . This LDOS is equivalent to the electronic charge density of the sample per energy unit at \vec{r}_0 at the Fermi level only (and not for all occupied states). Thus, an STM image reflects contours of constant surface LDOS during constant current imaging.

For clean metal surfaces, the LDOS generally resembles the total electron density of the sample surface, and the STM images are therefore to be interpreted as simple topographic maps of the surface. On the contrary, on semiconductor surfaces, localized states and dangling bonds are important for the contrasts in the STM images, which therefore do not necessarily reflect the geometrical arrangement of the atoms in the surface [3, 7].

Since the electronic states decay exponentially into the vacuum, expression (2.3) shows that the tunnel current depends on the tip-sample separation (z) according to $I_t \propto e^{-2\kappa z}$, where κ is the decay length of the electronic states. Since $\kappa \sim 1 \text{ \AA}^{-1}$ for most metal surfaces, $I_t(z)$ has a strong z -dependence.

Within the TH model adsorbates are imaged according to their way of perturbing the LDOS of the surface: If the LDOS at the Fermi level is depleted (enhanced) in the vicinity of the adsorbate, the tip must move closer to (further away from) the surface to keep the tunnel current constant, and hence the adsorbate is imaged as a depression (protrusion). This picture is further corroborated by calculations by Lang [9, 10]. In these calculations, e. g., O and S adsorbed on a jellium surface are imaged as a hole and a protrusion, respectively.

To summarize, STM images are to a first approximation to be viewed as contour maps of constant surface LDOS. The TH theory is probably the most widely used model for interpretation of STM images, and it works well in some cases [11, 12]. However, the model assumes that the tip-surface interaction is negligible and that the atomic structure of the tip has no influence on the image contrasts. Therefore, STM images simulated within the TH model should always be interpreted with great care. The advantage is that STM images are easily generated once the electronic and ionic structure of the surface are known. The discussion of some of the experimental results will include results from density functional theory (DFT) calculations, which compute surface structures fairly accurately and usually without large efforts. It is therefore straightforward to include simulated TH images in the discussions. The following chapters will demonstrate examples where the TH model is sufficient to account for the experimental observations.

In general, more elaborate and detailed theories (going beyond the perturbative TH approach) may be required for a more detailed and even quantitative simulation of the experimental STM images. One method is the Electron Scattering Quantum Chemistry (ESQC) formalism developed by Sautet [5]. In the ESQC model, the tunneling process is considered as a scattering phenomenon, where electrons originating from the interior of one of the STM electrodes either reflect at or tunnel through the tunnel junction. Specifically, the influence of imaging conditions like tip structure, bias voltage dependence and strong tip-surface interaction are included in this type of STM simulations. Such calculations have in some cases allowed quantitative structural information to be extracted from experimentally recorded images [13–15]. The major drawback of these more elaborate

simulations is that they are fairly complicated and time consuming. So far, the ESQC calculations have been based on the electronic structure obtained from the semi-empirical Hückel technique, which in general is less accurate than the DFT method. An upgraded source code will however soon be available which includes the electronic structure from DFT calculations [16].

2.3 Experimental implementation

2.3.1 The Århus STM

The inherent problem in the mechanical design of an STM is that the position of a tip has to be controlled on a sub-Ångström scale both laterally and vertically to the surface by construction elements of a centimeter-range size. This size-mismatch of approximately nine orders of magnitude makes the decoupling of external vibrations and the elimination of thermal drift from the microscope a technical challenge. The STM developed and used in our laboratory overcomes these complications by a small, compact and rigid scannertube-based design [1].

A cross-sectional sketch of the Århus STM is shown in figure 2.2. A crystal (A) is mounted on a plate of tantalum (B), which is inserted into the instrument and placed under copper-beryllium springs (C) holding (B) rigidly to the topplate (D) on the cylindrical scannerhouse. The topplate is fixed to the scannerhouse by three quartz balls (E) and is therefore electrically as well as thermally isolated. The tip (F) is made from a tungsten wire and is mounted at the end of the piezoelectric scannertube (G) used for raster-scanning the tip across the sample surface. The scannertube is glued onto a ceramic SiC rod (H) that runs through yet another piezoelectric tube (I) fastened inside the scannerhouse. The rod (H) and the tube (I) together constitute a linear motor used for coarse approaching of the scannertube and tip assembly towards the sample surface.

The compact design of the microscope has a high resonance frequency (~ 8 kHz) of vibrations of the tip relative to the surface. The scannerhouse (J) is placed on a stainless steel block (K) suspended in soft springs (O) (resonance frequency ~ 2 Hz) during scanning. This arrangement reduces the coupling to external vibrations so well that no other vibrational damping is needed. Furthermore, the high resonance frequency of the scannerhouse makes high sampling frequencies possible without excitation of vibrations in the mechanical parts. This is crucial for obtaining a fast STM.

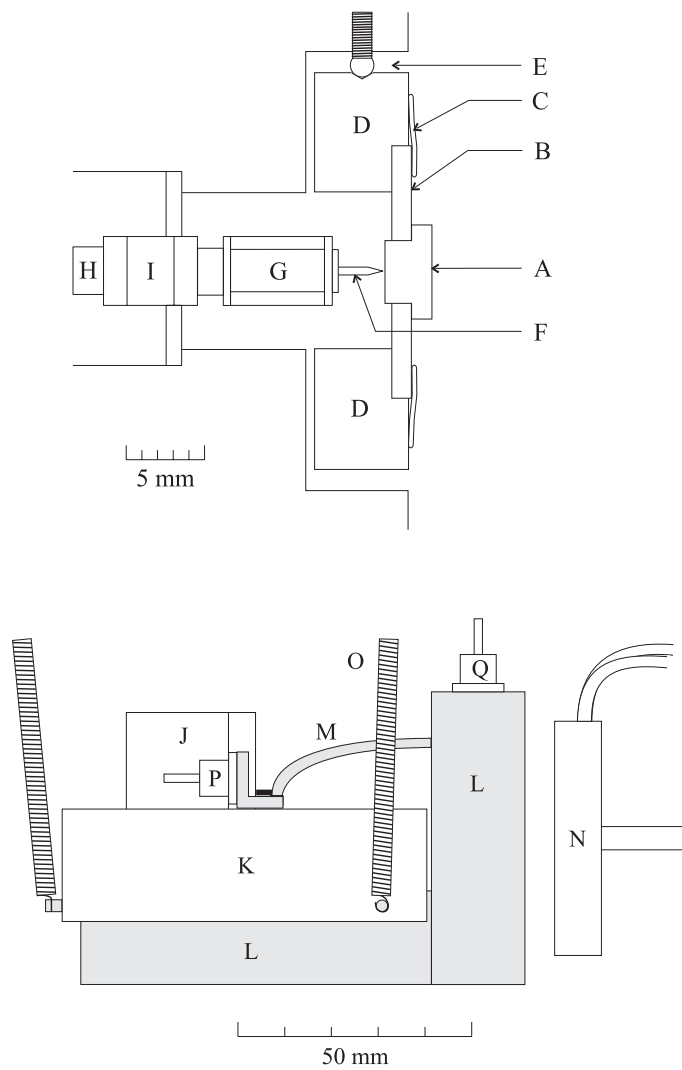


Figure 2.2: Sketch of the Århus STM. At the top, a cross-section of the STM scannerhouse (J) is illustrated. At the bottom, a sideview of the whole STM cradle is depicted. (A) Crystal. (B) Sample holder. (C) Springs. (D) Topplate. (E) Quartz ball. (F) STM tip. (G) Scannertube. (H), (I) Linear motor. (K) Stainless steel block. (L) Aluminium blocks. (M) Copper braid. (N) Dewar. (O) Suspension springs. (P), (Q) Zener diodes. Adapted from [17].

To prevent damaging both the tip and the surface during the insertion of a sample into the STM, the tip is retracted about 1 mm from tunneling distance. For coarse positioning of the tip, the linear motor moves the tip toward the sample until a tunnel current is established.

The piezoelectric tubes (both I and G) are silver-coated on the inside as well as on the outside. The motor tube (I) is, on the outside, divided into three electrodes perpendicular to the cylinder axis. On the inside, the two uttermost sections are equipped with bearings that ensure a very close fit with the rod (H). By appropriately biasing the end sections relative to the centre element, the tube clamps/unclamps to the rod at the ends, and the centre element expands or contracts along the tube axis. By repeatedly clamping one end, unclamping the other, elongating and/or contracting the centre, an "inchwormish" movement is established bringing the tip and scannertube assembly into or away from tunneling distance in roughly a minute.

The scannertube (G) controls the tip motion during image acquisition. The outside of the scannertube is divided into four equal electrodes along the cylinder axis. By applying antisymmetric voltages to opposite electrodes, one side lengthens, the other shortens, so the scannertube overall bends. In this way the lateral tip position is controlled with the four electrodes. By biasing the inner electrode, the whole scannertube elongates or contracts along its axis, providing control with the vertical tip motion, too.

The coarse approach and the scanning is fully automated and computer-controlled. The STM images consist typically of 256×256 pixels and are obtained by ramping the x - and y -deflection voltages on the scannertube, while a feedback circuit adjusts the z -voltage to keep I_t constant (figure 2.1). The z -voltages as a function of the lateral x - and y -voltages represent the STM image. The images are calibrated using atom-resolved STM images of clean metal surfaces. The STM images are shown as contour maps in which tip positions close to the surface are presented by darker grey colors as compared to positions further away.

Normally, the tip is not immediately in a state giving "good" resolution and an *in situ* modification of the tip is required. This is accomplished by indenting the tip into the surface or by applying pulses to the tunnel voltage (5 V for 0.1 s). In general, indentations leave the tip sharper while the voltage treatments stabilize the resolution. Of more radical character, a high voltage treatment, in which the sample is biased by up to ~ 1 kV through a $10 \text{ M}\Omega$ resistor with the tip placed $\sim 1 \mu\text{m}$ from the surface, can be applied to make a sort of field emission from the tip. However, there is

no guarantee that these modifications result in a "good" resolution, which is stable over extended periods. This depends on the experimentalist's experience and good luck.

2.3.2 Variable-temperature STM

The sample can be imaged at variable temperatures in the range from ~ 140 K up to at least 400 K. The temperature control is achieved by using two blocks of aluminum (L), mounted on the stainless steel plate (K) but thermally isolated from it, as heat reservoirs. The aluminum blocks are connected to the topplate (D) by two copperbraids (M).

When a sample temperature below room temperature is required, the Al blocks are cooled by pressing a liquid nitrogen cooled dewar (N) against them. Once the desired temperature is reached, the dewar is removed, so the cradle with the STM and the aluminum blocks is left in free suspension. The sample temperature is very stable and rises only by 4-5 K per hour due to the small heat conductivity through the quartz isolations and black body radiation. At this heating rate the thermal drift is reduced to a level that causes no problems for acquiring undistorted images. The temperature of the sample is measured by a chromel/alumel thermocouple mounted on the topplate about 1 cm from the sample. At low temperatures, a slow decrease in the temperature of the STM cannot be avoided. In order to keep the STM temperature constant at room-temperature, heat is dissipated in two reversely biased 70 V Zener diodes (P) mounted on (K). Due to the large voltage drop, only small currents (and thus thin wires) of ~ 2 mA are needed to deposit the necessary power.

Sample temperatures above room temperature can be obtained by passing a current through the two additional zener diodes (Q) mounted on the aluminum blocks (L).

2.3.3 STM movies

The STM not only allows surface structures to be explored on an atomic scale but provides also insight into how such surface structures develop in time [18]. Such an insight is obtained by acquiring many consecutive images over the same area. When played back, such a series of STM images, referred to as an STM movie, provides a direct visualization of the structural changes in time unveiling the dynamics in, e.g., reconstruction processes or surface chemical reactions [19–24]. Even quantitative, microscopic information concerning the diffusion of individual adatoms can be

extracted [25–29]. Obviously, dynamic studies like these require a characteristic frequency for the process, e.g. jump rate of the adatoms, which is comparable to or lower than the image sampling frequency.

In this thesis, STM movies are recorded to study the structural changes during adsorption of oxygen on Pt(110)–(1×2) (chapter 3) and to reveal how adsorbates modify self-diffusion on Pt(110)–(1×2) (chapter 4). The movies consist of up to several thousand images of an area of typically $200 \text{ \AA} \times 200 \text{ \AA}$. The acquisition time per image can be varied and is usually chosen in the range from 1 s to 20 s. The image acquisition time is the time-interval between the moments in which the tip probes I_t in the same pixel position in two successive images.

The acquisition of individual STM images with the sample thermally equilibrated with the instrument is not associated with a marked drift. But if a slight drift ($\sim 0.1 \text{ \AA/s}$) is left, the field of view can move far from the starting point, when images are recorded continuously over extended periods. To counteract this movement, a dynamic drift compensation routine is applied during the acquisition of STM movies. The routine is based on a pattern-recognition procedure, which for every new image localizes a characteristic and immobile feature on the surface (a kink or a vacancy). The necessary offset voltages, required to keep this feature on the same spot in the following image, are added by the routine to the scanning voltages applied to the scannertube. A stability of ± 1 pixel over several hours can hereby be achieved under favourable conditions.

The essential part of a quantitative analysis of the diffusion of adatoms is to map out, that is to track, the sites visited by the individual adatoms during an STM movie [25, 30]. This is usually a comprehensive work. To facilitate this, a semi-automatic software routine, based on the above mentioned pattern-recognition procedure, is developed in the group. Since the adatoms and their surroundings look very much alike on the different sites the adatoms visit, tracking simply means following a pre-defined pattern, e.g. an adatom, and logging its position versus time. In practice, this is done by saving height information in an area around an adatom as a template. In the following image, the template is moved around the previous adatom position until a maximum cross-correlation between the actual and the stored templates is obtained, thereby identifying the actual position. Repeating this procedure for every image in a movie (and for every adatom), the positions of an adatom are mapped during the movie. This works automatically as long as the adatom displacements are comparable to the size of the template. As a result, a record containing the pixel-positions through the movie is obtained for each adatom providing

the necessary information for quantifying the diffusion process. A slight lateral drift might be left in the movie. All tracked positions are therefore related to the position of a prominent and immobile feature, which is tracked in the same way. The tracked pixel positions are converted into adsorption sites. The distance calibration is obtained from atom-resolved images.

2.4 Concluding remarks

What sets the STM apart from most other surface sensitive techniques, is its ability to image in real space surface structures on the atomic scale. This has exerted an enormous impact on surface science and related research areas. At present, there are no signs that the importance of STM and other scanning probe techniques (e.g. AFM) will diminish. However, it is important to keep in mind that STM provides information about the electronic structure of the surface. STM lacks in principle the ability to specify the chemical identity of observed adsorbates or impurities from the STM images. Also the local character of STM may be a pitfall, if the observed features are not representative for the overall phenomenon being examined. Thus, relying too heavily and uncritically on STM alone may lead to erroneous conclusions, a fact often referred to as "tunnel vision". An interplay with complementary surface sensitive techniques providing crystallographic, subsurface, electronic and specific chemical information [31, 32] and/or theoretical studies is therefore of crucial importance.

References

- [1] E. Lægsgaard, F. Besenbacher, K. Mortensen, and I. Stensgaard, *J. Microsc.* **152**, 663 (1988).
- [2] C. J. Chen, *Introduction to Scanning Probe Microscopy* (Oxford University Press, Oxford, 1993).
- [3] R. Wiesendanger, *Scanning Probe Microscopy and Spectroscopy* (Cambridge University Press, Cambridge, 1994).
- [4] *Scanning Probe Microscopy 1-3*, edited by R. Wiesendanger and H.-J. Güntherodt (Springer-Verlag, Berlin, 1995).
- [5] P. Sautet, *Chemical Reviews* **97**, 1097 (1997).
- [6] J. Tersoff and D. R. Hamann, *Phys. Rev. Lett.* **50**, 1998 (1983).
- [7] J. Tersoff and D. R. Hamann, *Phys. Rev. B* **31**, 805 (1985).
- [8] J. Bardeen, *Phys. Rev. Lett.* **6**, 57 (1961).
- [9] N. D. Lang, *Phys. Rev. Lett.* **55**, 230 (1985).
- [10] N. D. Lang, *Phys. Rev. Lett.* **56**, 1164 (1986).
- [11] C. Klink, L. Olesen, F. Besenbacher, I. Stensgaard, E. Lægsgaard, and N. D. Lang, *Phys. Rev. Lett.* **71**, 4350 (1993).
- [12] D. M. Eigler, P. S. Weiss, E. K. Schwizer, and N. D. Lang, *Phys. Rev. Lett.* **66**, 1189 (1991).
- [13] M. Ø. Pedersen, M.-L. Bocquet, P. Sautet, E. Lægsgaard, I. Stensgaard, and F. Besenbacher, *Chem. Phys. Lett.* **299**, 430 (1999).
- [14] P. S. Weiss and D. M. Eigler, *Phys. Rev. Lett.* **71**, 3139 (1993).
- [15] P. Sautet and M.-L. Bocquet, *Phys. Rev. B* **53**, 4910 (1996).
- [16] M.-L. Bocquet and P. Sautet, private communication.
- [17] L. Olesen, PhD thesis, University of Aarhus, Denmark, 1996.
- [18] F. Besenbacher, *Rep. Prog. Phys.* **59**, 1737 (1996).
- [19] D. J. Coulman, J. Wintterlin, R. J. Behm, and G. Ertl, *Phys. Rev. Lett.* **64**, 1761 (1990).

- [20] F. Jensen, F. Besenbacher, E. Lægsgaard, and I. Stensgaard, *Phys. Rev. B* **41**, 10233 (1990).
- [21] P. T. Sprunger, Y. Okawa, F. Besenbacher, I. Stensgaard, and K. Tanaka, *Surf. Sci.* **344**, 98 (1995).
- [22] I. Stensgaard, E. Lægsgaard, and F. Besenbacher, *J. Chem. Phys.* **103**, 9825 (1995).
- [23] J. Wintterlin, S. Völkening, T. W. Janssens, T. Zambelli, and G. Ertl, *Science* **278**, 1931 (1997).
- [24] S. Völkening, K. Bedürftig, K. Jacobi, J. Wintterlin, and G. Ertl, *Phys. Rev. Lett.* **83**, 2672 (1999).
- [25] M. Ø. Pedersen, L. Österlund, J. J. Mortensen, M. Mavrikakis, L. B. Hansen, I. Stensgaard, E. Lægsgaard, J. K. Nørskov, and F. Besenbacher, *Phys. Rev. Lett.* **84**, 4898 (2000).
- [26] S. Renisch, R. Schuster, J. Wintterlin, and G. Ertl, *Phys. Rev. Lett.* **82**, 3839 (1999).
- [27] J. Wintterlin, R. Schuster, and G. Ertl, *Phys. Rev. Lett.* **77**, 123 (1996).
- [28] J. V. Barth, T. Zambelli, J. Wintterlin, R. Schuster, and G. Ertl, *Phys. Rev. B* **55**, 12902 (1997).
- [29] B. G. Briner, M. Doering, H.-P. Rust, and A. M. Bradshaw, *Science* **278**, 257 (1997).
- [30] T. R. Linderoth, S. Horch, E. Lægsgaard, I. Stensgaard, and F. Besenbacher, *Phys. Rev. Lett.* **78**, 4978 (1997).
- [31] A. Zangwill, *Physics at Surfaces* (Cambridge University Press, Cambridge, 1996).
- [32] H. Lüth, *Surfaces and Interfaces of Solid Materials* (Springer-Verlag, Berlin, 1995).

Chapter 3

Adsorption: O/Pt(110)–(1×2)

The interaction between solid surfaces and atoms and molecules impinging from a gas phase forms the basis for the most important heterogeneously catalyzed reactions. In general, a surface chemical reaction involves several elementary processes such as adsorption, surface diffusion, breaking of some adsorbate bonds, and the creation of new ones to form products, which eventually desorb from the surface. The gas–surface interaction may be so complex that even the basic mechanisms involved in the chemisorption of the individual reactants become hard to discern.

Platinum is one of the most versatile metal catalysts [1]. Technologically important chemical reactions catalyzed by platinum include the oxidation of CO and unburned hydrocarbons in car exhaust catalysts [1] and the water formation process in hydrogen-burning fuel cells [2]. A crucial step in these reactions is the interaction of oxygen with platinum, and knowledge about oxygen adsorption on platinum surfaces is therefore required to understand even such simple reactions in detail. This has spurred extensive studies of oxygen adsorption on low-indexed single-crystalline platinum surfaces as simple model catalysts using the arsenal of surface sensitive techniques [3, 4]. Although many studies have been carried out in the past (e.g. [5–11]), the O/Pt(110)–(1×2) system is, however, so complicated that no detailed models of the oxygen–induced structures have previously evolved.

By using the power of scanning tunneling microscopy (STM) to resolve structures on the atomic scale, the present chapter will give a com-

prehensive picture of oxygen adsorption on the Pt(110)-(1×2) surface, from single isolated oxygen atoms to a new high-coverage oxide-like structure, which self-organizes into a nanopattern extending over mesoscopic lengths. The outline of the chapter is as follows: First, the structure of the Pt(110)-(1×2) surface and the experimental procedures will be described briefly. An interplay between STM experiments and density functional theory (DFT) calculations is then presented, which establishes a microscopic picture of the oxygen-induced structures. Finally, the origin of the pattern formation will be discussed. The chapter includes results from [I], [II] and [III].

3.1 Pt(110)-(1×2) and experimental details

The Pt(110) surface belongs to the class of $5d$ metal surfaces which reconstruct in their clean state. For these surfaces, the driving mechanism for the reconstruction is related to a large excess tensile stress in the unreconstructed surface [12–14]. A number of experimental [15, 16] and theoretical [17] investigations finds that the more stable state of clean Pt(110) surface is a (1×2) missing-row reconstruction in which every second $[1\bar{1}0]$ row is missing. This implies that the surface consists of throughs stabilized by close-packed (111) micro-facets (see figure 3.1).

Concerning the surface morphology, the terraces are highly anisotropic, as shown in figure 3.1(b). Step edges oriented along the $[1\bar{1}0]$ direction can extend over thousands of lattice spacings. The density of such $[1\bar{1}0]$ oriented steps is high. Thus, the terraces become narrow along the $[001]$ direction and elongated along the $[1\bar{1}0]$ direction. Furthermore, the $[1\bar{1}0]$ oriented steps occur typically in either ascending or descending sequences, so the clean surface obtains oblonged $[1\bar{1}0]$ oriented ridges on a mesoscopic scale (figure 3.1(b)). Such ridges form a superstructure with a periodicity of $\sim 1000 \text{ \AA}$ along $[001]$, and they represent a height modulation with an amplitude of $\sim 30 \text{ \AA}$ (figure 3.1(c)). It has been suggested that the periodic self-organisation results from an intrinsic stress in the surface [18, 19]. The surface has no straight step edges oriented along the $[001]$ direction. Instead, another type of morphology is observed to terminate the terraces and the oblonged ridges along the $[1\bar{1}0]$ direction. This structure, often referred to as the “fish-scale” pattern [16, 18], is illustrated in figure 3.1(d) and is characterized as areas with a high kink density. Thus, the Pt(110)-(1×2) surface has an overall rough morphology, which makes it difficult to localize wide terraces. Terraces $\sim 200\text{--}500 \text{ \AA}$ wide in the $[001]$ direction

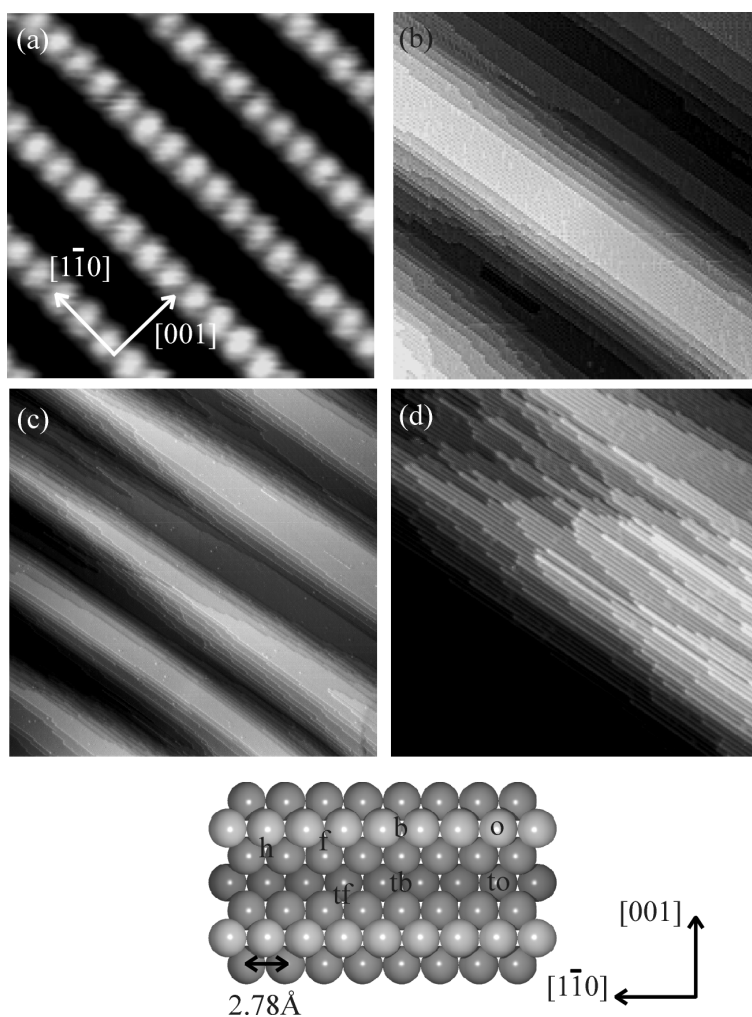


Figure 3.1: Four STM images of the $Pt(110)-(1 \times 2)$ surface. (a) An atom-resolved image of a terrace. Size $31 \times 34 \text{ \AA}^2$. (b) Terraces forming an oblonged ridge in the $[1\bar{1}0]$ direction. Size $861 \times 916 \text{ \AA}^2$. (c) The morphology on a mesoscopic scale. Size $2550 \times 2640 \text{ \AA}^2$. (d) The “fish-scale” pattern. Size $734 \times 759 \text{ \AA}^2$. The ball model indicates the different adsorption sites in the trough and at or near the ridges of the $Pt(110)-(1 \times 2)$ surface: the trough fcc (tf), the trough bridge (tb), the trough on-top (to), the hcp site (h), the fcc (f), the bridge (b) and the on-top (o) sites.

do, however, exist, and the STM measurements are carried out on those.

All the experiments on the single-crystalline Pt(110)-(1×2) surface are performed in an ultra-high vacuum (UHV) chamber with a base pressure less than 1×10^{-10} mbar. In addition to a home-built STM (described in section 2), the UHV chamber is equipped with standard facilities for cleaning the surface as well as facilities for Auger electron spectroscopy (AES) and low-energy electron diffraction (LEED), which are used to characterize the surface chemical composition and crystallinity, respectively. The residual gas composition and the purity of introduced gasses are analysed with a quadrupole mass spectrometer. (The nominal purity for O₂ is 99.999%, for H₂ 99.999% and for CO 99.997%. H₂ and CO is used in the studies reported in chapter 4).

After an opening of the UHV chamber, the surface is initially cleaned by repeated cycles of sputtering with 1.5 kV Ne ions for half an hour followed by an oxygen treatment consisting of annealing in 5×10^{-7} mbar O₂ at 750 K for 15 minutes and a subsequent flash to 980 K in vacuum (all ramps 2 K/s). This procedure is effective for removing contamination rising from the bulk or present as a result of air exposure. The cleaning is stopped when the surface is in its clean (1×2) reconstructed state as judged by AES, LEED and STM. On a daily basis the surface is cleaned by sputtering with 1.5 kV Ne ions for half an hour followed by annealing to 980 K in vacuum (ramp 2 K/s). On the day-to-day basis only STM is used for characterizing the sample cleanness due to its much higher sensitivity towards impurities.

3.2 Oxygen-induced surface structures

Previous isotope exchange studies using temperature-programmed desorption (TPD) spectroscopy find that oxygen adsorbs molecularly at substrate temperatures below 180 K, desorbs and dissociates in the range 180–220 K, and adsorbs dissociatively above 220 K [6]. In the following, all oxygen exposures are limited to substrate temperatures above 220 K, so oxygen is only present on the surface in its atomic state. Associative desorption of oxygen occurs above 650 K [6].

The results presented in the following are obtained in two types of STM experiments. The first kind monitors the dynamical changes on the surface during oxygen adsorption. An initially clean crystal is inserted into the STM at a temperature above 220 K, and a terrace is then sequentially imaged, i.e. an STM movie is acquired, while a background pressure of oxygen is introduced to the UHV chamber. The second type of experiments

reveals the atomic details of the static surface structures. In this case, the surface is preexposed to an amount of oxygen outside the STM given in Langmuir, $1\text{L} = 10^{-6} \text{ torr}\times\text{s}$. Afterwards the sample is transferred to the STM and scanned under UHV conditions at either room temperature (RT) or below 220 K.

The STM movies revealing the building up of structures during oxygen exposure are recorded at fixed substrate temperatures in the range from 230 K to 357 K and with oxygen partial pressures ranging from 1×10^{-8} mbar to 1×10^{-7} mbar. An STM movie normally extends over 1/2 – 1 hour. Due to the STM tip, a shadow effect may reduce the actual oxygen exposure in the scanned region. All oxygen exposures related to STM movies are therefore given in Langmuir with a subscript “f”, indicating the exposure which would occur without the presence of the tip.

Figure 3.2 shows four snap-shots from an STM movie. In the beginning, what appear as noise or spikes on the terraces show up in the recorded STM images (figure 3.2(a)). The noisy appearance of the Pt ridges is actually caused by extremely mobile oxygen atoms. When they pass by the tunneling region, they give rise to spikes in the tunnel current signal. Similar results are found in [20].

After an exposure of $\sim 10\text{--}20\text{L}_f$, stripes are observed to nucleate and subsequently grow along the $[1\bar{1}0]$ ridge, as shown in figure 3.2(b). Atom-resolved STM images reveal that such stripes consist of protrusions, which are localized on lattice positions of the underlying substrate and have a periodicity identical to that of clean Pt surface along the $[1\bar{1}0]$ direction (figure 3.3). The stripes protrude $\sim 0.4\text{--}0.5\text{Å}$ further outwards from the ridges, independent of the tunnel parameters. During the stripe formation, no mass transport of substrate atoms from either terraces or steps is observed.

Initially, the nucleation of these stripes occurs homogeneously on the terrace, but at a fairly low stripe coverage of $\sim 0.04\text{ML}^1$ the subsequently formed stripes tend to align along the $[001]$ direction (figure 3.2(b)). That is, bands of stripes oriented perpendicular to the close-packed direction form, and so a two-dimensional nanostructure emerges spontaneously (figure 3.2(c)–(d)). In figure 3.2(d) the coverage of the stripes is $\sim 0.6\text{ML}$, and the individual stripes consist on average of 7-8 protrusions and are separated by 4-5 lattice spacings. The corresponding superperiodicity along the $[1\bar{1}0]$ direction is 10-12 nearest-neighbour distances.

The extension of the oxygen pattern is illustrated in figure 3.4. The regular alignment of the stripes persists over the terraces and even over

¹1 ML is defined as the atom density in the first layer of the Pt(110)–(1×2) surface.

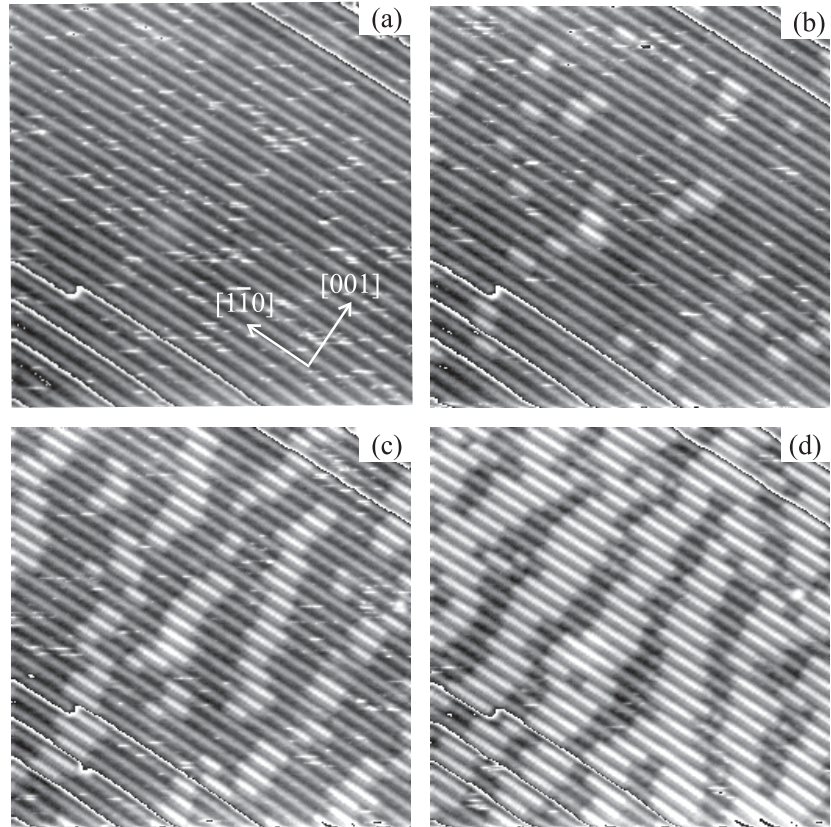


Figure 3.2: Four stills from an STM movie showing the stripe formation at a substrate temperature $T = 357$ K. The images show a broad terrace surrounded by more narrow and descending terraces. The full color scale is applied to each terrace, so the step edges appear as white/black lines running along the $[1\bar{1}0]$ direction. The oxygen dosage is (a) $10 L_f$, (b) $18 L_f$, (c) $39 L_f$ and (d) $205 L_f$ ($\theta_{stripe} \sim 0.6$ ML). Image size $208 \times 226 \text{ \AA}^2$. $I_t = 1.10$ nA and $V_t = -10.4$ mV.

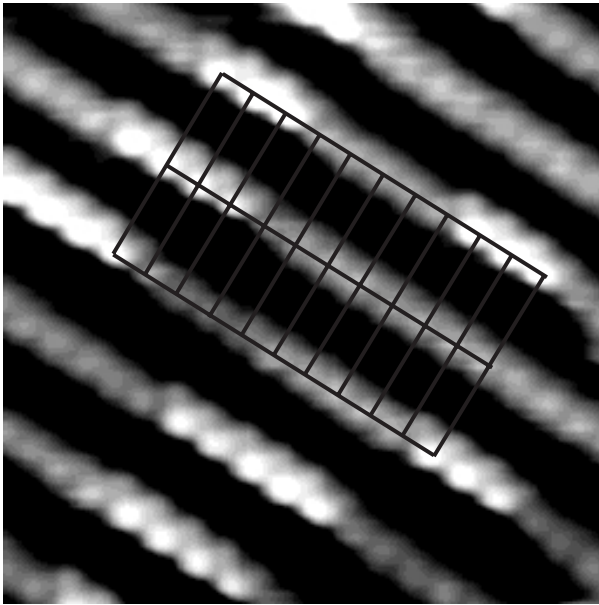


Figure 3.3: An atom-resolved STM image of the oxygen-induced stripes after an exposure of $21 L_f$ at $T = 336$ K. The grid superimposed in the image shows the registry of the protrusions in a stripe relative to the Pt atoms in the ridges. The image size is $43 \times 47 \text{ \AA}^2$. $I_t = 0.46$ nA and $V_t = -2.1$ mV.

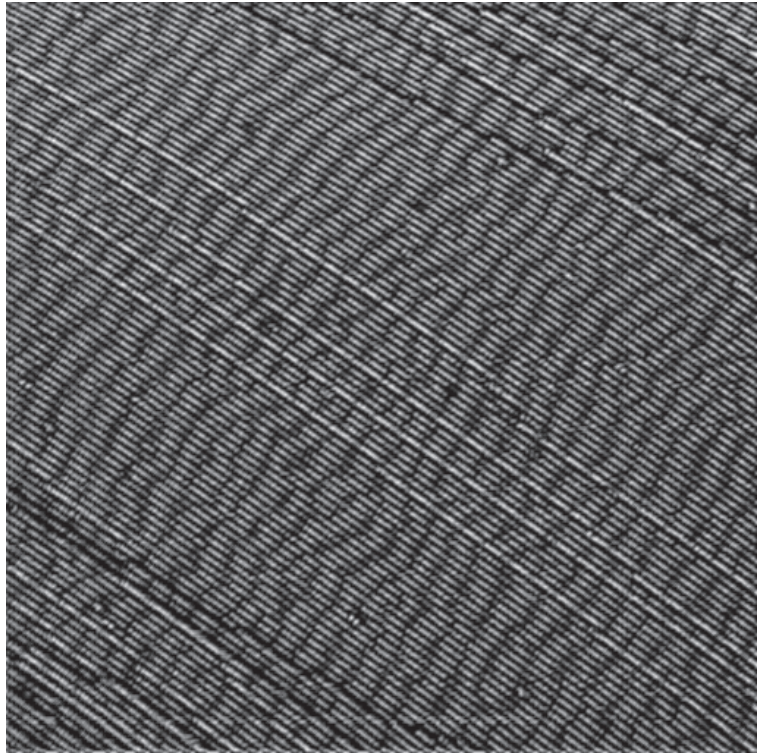


Figure 3.4: An STM image of the oxygen pattern showing the extension of the stripe alignment. Oxygen is exposed 281 L at 400 K. Image size $703 \text{ \AA} \times 840 \text{ \AA}$. The image is acquired at RT.

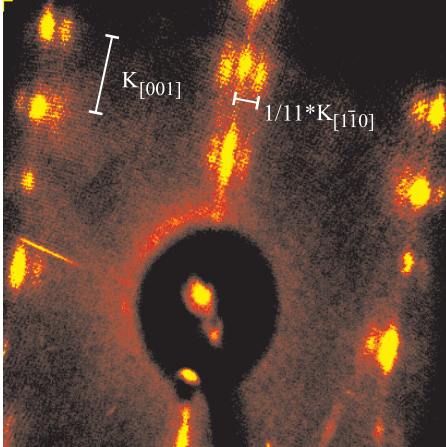


Figure 3.5: The LEED pattern corresponding to the oxygen pattern shown in figure 3.4 shows satellite spots of a (11×2) superstructure. The beam energy was 105 eV.

the step edges, so the bands of stripes extend over a mesoscopic scale. Occasionally, the alignment may be disrupted, e.g. at step edges. The characteristic superstructure introduced by the oxygen pattern is also observed in the corresponding LEED pattern (figure 3.5).

These observations address two main questions: (i) what are the microscopic details of the oxygen-induced structures and (ii) what is the origin of the pattern formation? The following section 3.3 will describe the atomic details of the oxygen-induced structures. The various structures appearing with the increasing oxygen coverage are characterized by STM. Theoretical results are presented, and a coherent picture of the O/Pt(110)-(1×2) system is obtained from an interplay with the experimental observations. The pattern formation will be described more thoroughly in section 3.4.

3.3 Atomic details of the oxygen structures

3.3.1 Experimental results

At low coverages oxygen atoms diffuse very fast even at temperatures just above 220 K. As a consequence, structural changes occur on a time

scale considerably shorter than the typical STM image acquisition time, resulting in a blurred appearance of the Pt ridges. In order to suppress the thermally activated diffusion of the oxygen atoms, experiments are performed in which the clean sample is exposed to oxygen at RT outside the STM and subsequently transferred to the microscope, where scanning is performed at temperatures ~ 220 K.

From theoretical calculations, described in section 3.3.2, the energy barrier for an oxygen atom to diffuse along the $[1\bar{1}0]$ ridge between fcc sites via hcp sites is calculated to be $E_d = 0.53$ eV. This diffusion barrier provides an estimate of the temperature range in which the changes in the oxygen-induced structures are suppressed relative to the typical imaging time. Neglecting the O–O interactions, this suppression happens when the O hopping-rate, $h = \nu \exp(-E_d/k_B T)$ (section 4), is smaller than the typical image acquisition frequency (0.1 – 0.2 s $^{-1}$). Assuming a prefactor $\nu = 10^{12}$ s $^{-1}$, the O hopping-rate is 0.1 s $^{-1}$ at a substrate temperature of 205 K, and the temperature window of interest is therefore below this value. This is in good agreement with the experimental observation that temperatures of ~ 200 K or below are sufficient for imaging oxygen-induced structures in the low coverage regime.

At low oxygen exposures of ~ 0.1 L, oxygen-induced depressions (termed A_1) appear on the $[1\bar{1}0]$ ridges with a coverage of ~ 0.08 ML (figure 3.6(a)). A linescan shows that these depressions are ~ 0.1 Å deep compared to the surrounding ridge, and the grid superimposed in the STM image reveals that the depressions are located on bridge sites on the Pt ridges. The STM image in figure 3.6(b) is the same as in (a). However, the color code is changed in order to accentuate that depressions are also observed on the fcc sites adjacent to a depression on the bridge site. According to Lang’s theory for imaging adsorbates in STM, chemisorbed oxygen atoms are expected to be imaged as depressions, since O normally depletes the LDOS at the Fermi level [21–24]. For this reason, the depressions are tentatively associated with O atoms chemisorbed in the fcc sites. The ridge next to a depression is imaged brighter in figure 3.6(a). This is attributed to changes in the electronic structure along the ridge caused by the adsorbed O atom. Furthermore, figure 3.6 shows that the oxygen-induced depressions are separated by at least $2 \times a_{[1\bar{1}0]}$, indicating a nearest-neighbour repulsive interaction between the O atoms along the ridge.

When the oxygen exposure is slightly increased to ~ 1 L, the ridges are found to be covered with such depressions separated by $2 \times a_{[1\bar{1}0]}$, as shown in figure 3.7. This structure, termed A_2 , develops into domains of either $c(2 \times 4)$ or $p(2 \times 2)$ symmetry, since the A_2 depressions on neighbouring

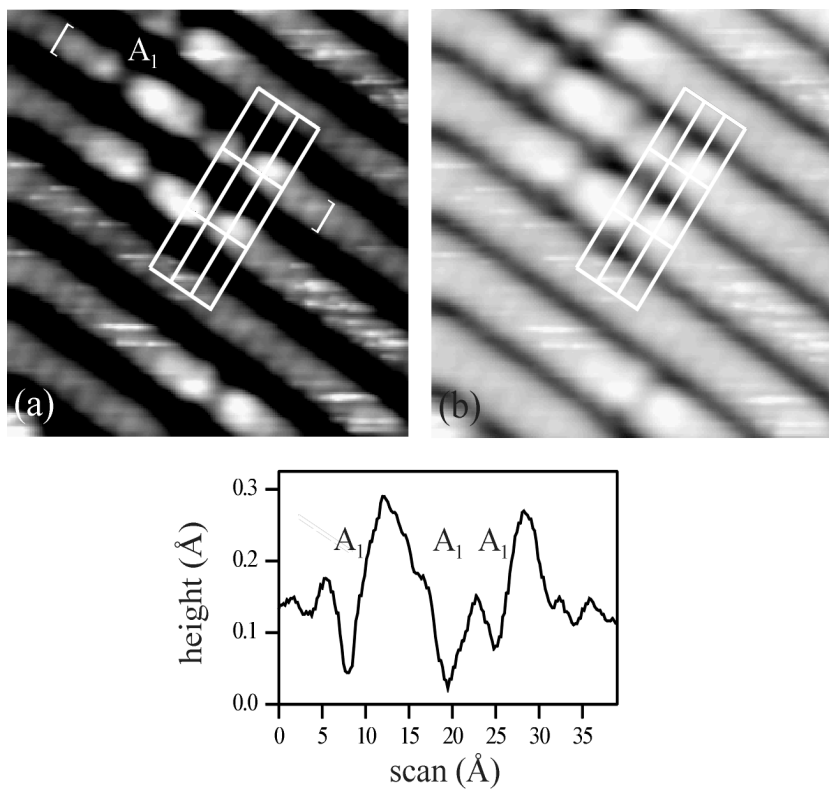


Figure 3.6: (a) An atom-resolved STM image of depressions (A_1) on the $[1\bar{1}0]$ Pt ridges induced by chemisorbed O atoms. The grid marks bridge sites on the ridges. The sample is exposed to 0.1 L of oxygen at 313 K before transfer to the STM. Substrate temperature 159 K. Size $33 \times 39 \text{ \AA}^2$. (b) The same image as in (a), but the color code has been modified to accentuate the corrugations on the sides of the ridges. The linescan originates from the ridge segment indicated by the brackets in (a).

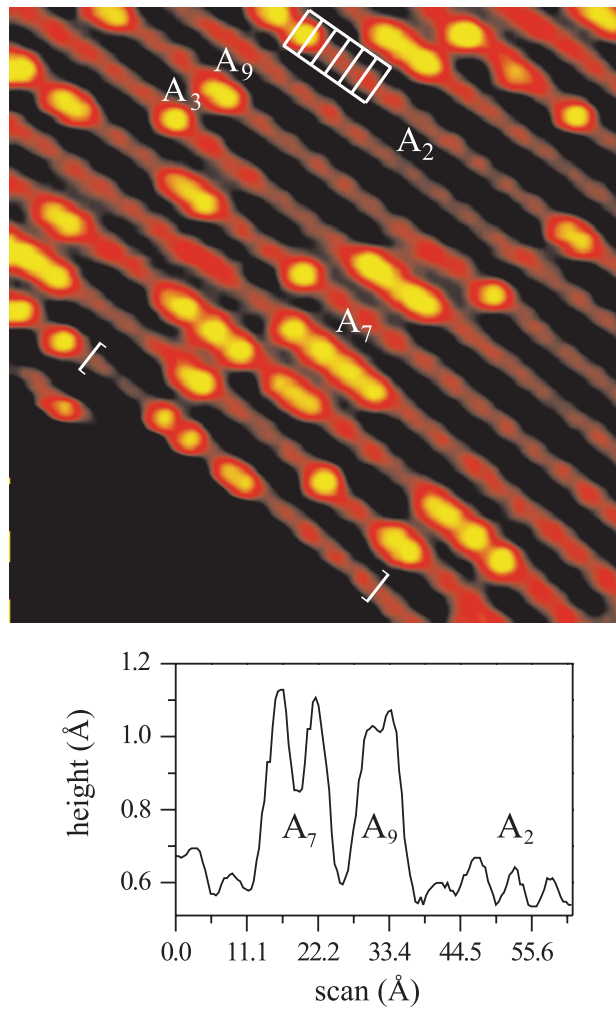


Figure 3.7: The STM image shows the structural elements A_2 , A_3 , A_7 and A_9 . The grid marks successively bridge sites along the ridge, as determined by the position of the depressions. In the linescan, which comes from the ridge segment marked by the brackets, the ticks on the scan axis denote lattice positions. Image acquisition time 5.8 s. Oxygen exposure 1.4 L at 309 K. Scanned at 203 K. Image size $100 \times 101 \text{ \AA}^2$.

ridges can either be in phase or be shifted by $a_{[1\bar{1}0]}$ (only the former is found in figure 3.7).

The A_2 domains are, however, observed to have a fairly limited extension due to the appearance of other characteristic oxygen-induced structures (figure 3.7). These new structural elements all show up as bright protrusions localized on Pt lattice sites. The registry is inferred from grids superimposed in STM images, as illustrated in figure 3.7. A linescan in figure 3.7 shows that the depressions represent a height modulation of $\sim 0.1 \text{ \AA}$, and that the bright elements protrude $\sim 0.45 \text{ \AA}$ further out from the ridge. The protrusions are found in different configurations. Isolated bright elements, termed A_3 , cover about 5% of the ridge sites. Protrusions also develop into chains separated by at least $2 \times a_{[1\bar{1}0]}$ (termed A_7), or stripes with a periodicity of only $1 \times a_{[1\bar{1}0]}$ (termed A_9).

As the oxygen exposure is increased further, more of the A_9 stripes nucleate and grow among the myriad of the coexisting structural elements, which were identified above. These stripes tend to align along the $[001]$ direction and thus merge into a two-dimensional nanostructure, as illustrated in figure 3.2.

When the Pt(110)-(1 \times 2) surface is exposed to oxygen and scanned at constant substrate temperatures above 220 K, only two types of structures appear stable in the STM images: (i) the stripe structure (A_9) and (ii) the double-periodic depression structure (A_2). The A_2 structure shows up occasionally on the ridges in between the stripes (figure 3.8). More frequently, the ridges have a blurred appearance. This shows that the local oxygen coverage varies on the different ridge segments separating the stripes.

Figure 3.9 shows how the coverage and the density of the oxygen-induced stripes evolve during the oxygen exposure. Above a critical exposure of typically 10-20 L_f , the oxygen-induced stripes begin to form. The density of the stripes has a steep increase at low stripe coverages and saturates at higher exposures. The coverage of the stripes on the other hand grows more smoothly. The formation of the stripes is thus associated with a transition from a regime, where stripes preferentially nucleate, to a state where the growth of the individual stripe is dominating. If the oxygen dosage at RT is continued further up to a stripe coverage of $\sim 0.8 \text{ ML}$, a new type of protrusions appears. These protrusions are $\sim 0.4 \text{ \AA}$ higher than the stripes and show up between coalescing stripes (figure 3.10).

To summarize, structures induced by chemisorbed oxygen atoms have been identified and characterized in this section. At substrate temperatures above $\sim 220 \text{ K}$, oxygen is very mobile at low coverages. As the oxy-

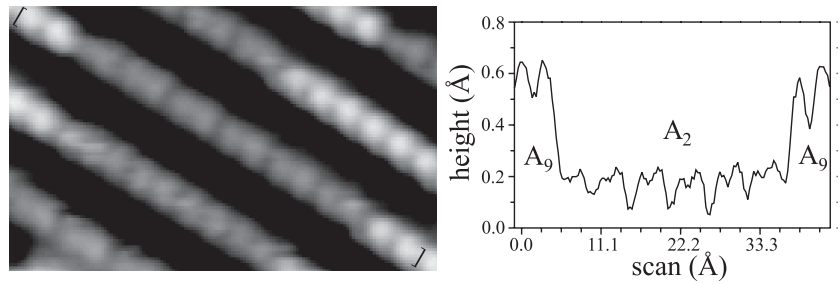


Figure 3.8: An STM image of the A_2 double-periodic depression structure observed between the A_9 stripes. The linescan originates from the ridge segment marked by the brackets. The neighbouring ridge appears blurred and without any stable oxygen-induced structures. Size $38 \times 26 \text{ \AA}^2$. The image is recorded at a substrate temperature of 304 K after an exposure of 72 L at this temperature.

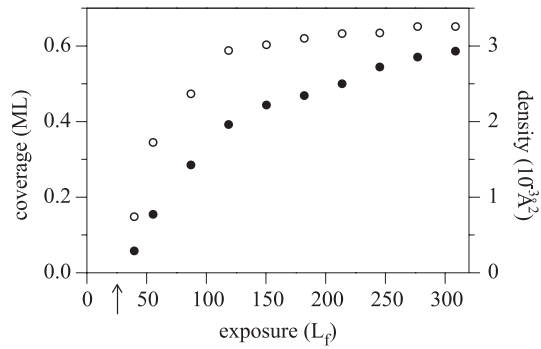


Figure 3.9: Stripe coverage (filled circles) and stripe density (open circles) as a function of the oxygen exposure in an STM movie, acquired with the sample at RT and with a background pressure of oxygen of 5×10^{-8} mbar. The arrow indicates the exposure at which stripes begin to emerge.

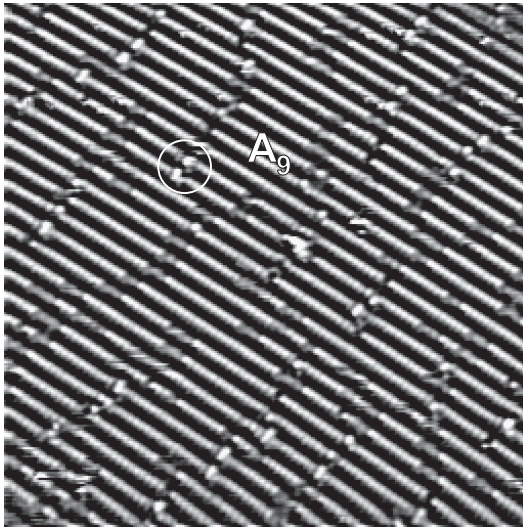


Figure 3.10: The oxygen pattern (A_9) close to saturation. Brighter protrusions appear in between coalescing stripes, as indicated by the circle. The sample was kept at RT during oxygen exposure and image acquisition. Image size $291 \times 317 \text{ \AA}^2$.

gen coverage is increased, oxygen-induced stripes emerge and self-organize spontaneously into $[001]$ oriented bands forming an oxygen nanostructure. From the quench-and-look experiments, the STM results reveal that five different structural elements, A_1 , A_2 , A_3 , A_7 , and A_9 are sufficient to build a myriad of coexisting structures. At low coverages, depressions localized on the bridge site on the ridges appear and condense into a structure with a double periodicity along the ridges. At higher coverages, bright protrusions positioned at lattice sites appear. In the following, the present experimental results will be discussed in the light of density functional theory (DFT) calculations. A number of examples have shown that DFT calculations can provide fairly accurate results on adsorption properties on metal surfaces, e.g. [25–28]. The interplay between STM experiments and DFT calculations establishes a coherent picture of $\text{O}/\text{Pt}(110)-(1 \times 2)$. The consistency of this picture is tested by comparison with previous experimental studies.

3.3.2 Theoretical results

A theoretical study of oxygen adsorption on Pt(110)-(1×2) has been performed by H. T. Lorensen at the Technical University of Denmark ([I] and [29]). Equilibrium structures, adsorption energies, diffusion barriers and vibrational energies have been obtained from calculations performed within the density functional theory. The results will be presented and discussed in this section.

Density functional theory is a very efficient way to obtain the ground state electron density and total energy in a many-electron system. In the present calculations, a super-cell approach is taken in which the surface is described by a slab containing five (110) oriented layers of platinum and nine layers of vacuum. Each layer is a (2×2) or (2×3) Pt(110) unit cell containing four or six atoms, respectively, except for the missing-row reconstructed top layer, where only two or three atoms are present. The super-cell is repeated in three dimensions. The electron-ion interaction is described with pseudo-potentials [30], and the non-local exchange and correlation term in the electron-electron interactions is treated within the generalized gradient approximation described by Perdew and Wang [31]. A more detailed description of the calculations can be found in reference [I] and [29].

In order to find the optimum adsorption site of O on Pt(110)-(1×2), the adsorption energy has been calculated for a number of high and low symmetry positions, including the fcc, the hcp, the bridge and the on-top sites as well as three sites in the trough (the threefold fcc site, the fourfold bridge site, the fivefold hollow site) and a subsurface site beneath the ridge-Pt atom. The various sites are illustrated in figure 3.1. The DFT calculations are performed for these adsorption sites using a (2×2) unit cell with an oxygen coverage of $\frac{1}{2}$ ML. The lowest energy adsorption site is found to be the fcc site with an adsorption energy of -3.91 eV relative to atomic oxygen in the gas phase. In the hcp site, the corresponding energy is 0.21 eV higher. At the bridge site, the potential energy surface has the character of a saddle-point, and O is more weakly bound by 0.04 eV compared to the fcc site. For the on-top position, corresponding to a local maximum on the potential energy surface, oxygen is less strongly bound by 0.90 eV. For all the sites in the trough and the subsurface site, oxygen is more weakly bound by more than 0.5 eV compared to the fcc site. Although sites in the trough [7] and subsurface sites [9] were considered important in previous experimental studies, they can be excluded on the basis of the DFT calculations.

The previous findings of subsurface oxygen are based on photo-emission electron microscopy (PEEM), deriving its imaging contrasts from work function variations induced by the adsorbates [32]. It should be added that subsurface oxygen is only observed when intermediate CO is present, causing a lifting of the (1×2) reconstruction to a (1×1) structure of the surface. On clean Pt(110)- (1×2) oxygen is not observed to form subsurface oxygen [9]. AES measurements confirming this observation have been performed. AES probes oxygen to a depth of $\sim 10 \text{ \AA}$ [33]. Increasing the substrate temperature from 400 K to 500 K during the oxygen exposure leads to a reduction of the oxygen AES signal, whereas an increase would have been expected if subsurface species were formed.

The oxygen diffusion barrier, for moving from an fcc site through a bridge site to an fcc site on the opposite side of the Pt ridge, is found to be the difference $E(\text{bridge})-E(\text{fcc})=0.04 \text{ eV}$. For an oxygen atom moving along the (111) micro-facet near the Pt ridge from an fcc site via an hcp site to the next fcc site, the diffusion barrier is 0.53 eV. This value matches the oxygen diffusion barrier on the Pt(111) surface. On the Pt(111) surface, oxygen diffuses in a similar way between fcc sites via hcp sites. Experimentally, the barrier on Pt(111) is determined to $E_d=0.43 \text{ eV}$ [34], whereas recent theoretical calculations find $E_d=0.55 \text{ eV}$ [35].

Furthermore, theoretical calculations show that oxygen binds $\sim 0.5 \text{ eV}$ stronger to the fcc site compared to the hcp site on Pt(111) [35–37]. Thus, as for O/Pt(110)- (1×2) , the fcc site is the preferred adsorption site, but the energy difference between the fcc and the hcp site is larger than the 0.21 eV on Pt(110)- (1×2) .

In the following, only the lowest energy fcc adsorption site will be considered. Nine different oxygen configurations have been investigated, corresponding to the models (1) to (9) in figure 3.11. From the DFT calculations the binding energy per O atom (E_O) as well as the vertical geometrical displacement for the ridge-Pt atoms ($z - z_0$), relative to the position in a clean surface (z_0), are obtained for each configuration. It should be noticed that the difference in E_O between the various models is fairly small $\approx 0.1\text{--}0.2 \text{ eV}$. These models are the lowest energy configurations. Even without taking into account the O–O repulsion, configurations involving other sites than the most stable fcc site will bind oxygen less strongly than the pure fcc configurations. In the calculations, the positions of the atoms have been relaxed to find the lowest energy for a given model. For the Pt lattice the only significant relaxation is the vertical displacement of the ridge-Pt atoms outwards from the surface.

Due to the periodic boundary conditions applied in the calculations,

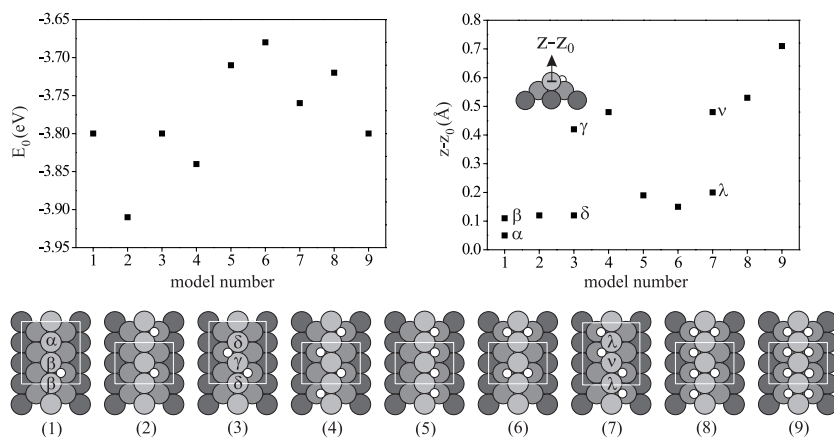


Figure 3.11: Ball models of O/Pt(110)-(1×2). A Pt ridge (light-grey circles) is sketched with adjacent (111) facets (darker grey circles). In models (1)–(9), white circles symbolize O atoms in fcc sites. The white squares indicate the surface unit cell used in the calculations. For configurations (1)–(9), E_O and $(z - z_0)$ are depicted. E_O is the binding energy per O atom relative to atomic oxygen in the gas phase. $(z - z_0)$ is the height of the ridge-Pt atom relative to the position on the clean surface (z_0). Model (1) corresponds to a local coverage θ_O^{loc} of 1/3 ML, (2) to 1/2 ML, (3) to 2/3 ML, (4)–(7) to 1 ML, (8) to 1½ ML, and (9) to 2 ML.

the ball models in figure 3.11 correspond to an oxygen coverage of 1/3 ML in (1), 1/2 ML in (2), 2/3 ML in (3), 1 ML in (4)–(7), 1½ ML in (8), and 2 ML in (9), respectively.

In configuration (1) at 1/3 ML coverage, the binding energy of an oxygen atom is -3.80 eV. It is seen that the ridge-Pt atoms (labelled β) with one oxygen neighbour relax outwards by 0.11 Å, whereas the ridge-Pt atom (labelled α) without any oxygen neighbours only relaxes by 0.05 Å. Concerning the binding energy, model (2) represents the lowest energy configuration with oxygen adsorbed in the fcc site at 1/2 ML coverage. This configuration describes a double periodicity along the $[1\bar{1}0]$ direction due to the periodic boundary conditions. For model (2), the oxygen atoms lead to a slight relaxation of the ridge-Pt atoms by 0.16 Å. When the oxygen coverage is increased to 2/3 ML in model (3), the binding energy is reduced by 0.09 eV compared to model (2). The ridge-Pt atom (labelled γ) with two neighbour oxygen atoms relaxes outwards by 0.42 Å. The two other

Model number	2	4	5	9
$E_{relaxed}(\text{eV})$	-3.91	-3.84	-3.71	-3.80
$E_{unrelaxed}(\text{eV})$	-3.69	-3.56	-3.42	-3.08

Table 3.1: The binding energy E_0 for models (2), (4), (5) and (9), respectively, on a relaxed (as in figure 3.11) and an unrelaxed substrate.

ridge-Pt atoms (labelled δ) in the unit cell have only one oxygen neighbour each, and these Pt atoms only relax outward by 0.12 Å. At 1 ML coverage, four possible structures are model (4), (5), (6) and (7). Configuration (4) corresponds to a zigzag configuration of the oxygen atoms. In this structure, all ridge-Pt atom are relaxed outwards by 0.48 Å. Models (5) and (6) are energetically less favourable compared to (4). Configuration (7) is basically a combination of models (4) and (5). The two oxygen neighbours of the ν -Pt give a large relaxation, as in model (4). The relaxation is smaller around the λ -Pt atom, where the oxygen neighbours are located on the same side of the ridge, as in model (5). The binding energy of model (7) is in between that for models (4) and (5). When increasing the coverage to 2 ML, the configuration (9) emerges. This is associated with the largest ridge-Pt atom displacement and a binding energy lower than in (8) at $1\frac{1}{2}$ ML. Thus, the five structures (1), (2), (3), (4) and (9) are ~ 0.1 eV lower in energy than any of the other structures, and these will be considered in the following section 3.3.3.

The effect of relaxation of the Pt lattice is illustrated in table 3.1. The binding energy of O in some of the oxygen configurations in figure 3.11 is compared with the O binding energy in the same structures on a rigid Pt(110)-(1 \times 2) substrate. It is evident that the relaxation of the Pt lattice has a large influence on the stability of especially the high-coverage structures.

On the inclined (111) micro-facets, two vibrational modes of oxygen adsorbed in the fcc site are dipole active, since the corresponding electrical dipole moments have components perpendicular to the surface plane [33]. The first mode is the vibration perpendicular to the (111) micro-facet. A calculation at $\frac{1}{2}$ ML oxygen coverage yields a frequency of 467 cm^{-1} . The second mode is parallel to (111) micro-facet and has a vibration frequency of 316 cm^{-1} .

In order to link the equilibrium structures obtained from the DFT cal-

culations to the experimental STM images, STM images have been calculated within the Tersoff-Hamann scheme (section 2.2), using the electronic structure obtained from the DFT calculations. The calculated STM images reflect iso-surfaces of LDOS at the Fermi level and are obtained at a constant LDOS = 0.001 electrons/eVÅ³. This value is chosen since the corrugation along the Pt ridge on the clean surface in the calculated STM image is the same as that measured experimentally (typically ≈ 0.1 Å). Calculated STM images are shown in figure 3.12. The calculated image for the clean surface is shown for comparison. The oxygen in model (1) produces a depression of ~ 0.2 Å on the bridge site. A similar depression is observed in the simulated STM image of model (2). In both model (4) and model (9) protrusions appear on the Pt lattice sites of almost the same height of 0.32 Å and 0.43 Å, respectively, compared to the ridge atoms on the clean surface.

3.3.3 A coherent picture of O/Pt(110)-(1×2)

In the following, a coherent picture will be presented for the oxygen adsorption on the Pt(110)-(1×2) surface. The picture is obtained from an interplay between the experimental STM results and the DFT calculations presented in the two previous sections.

At low exposures the oxygen-induced depressions A_1 are found at the bridge sites and are found to evolve into the prevalent double-periodic structure A_2 . These features are associated with models (1) and (2) in figure 3.11. For the structural model (1), the STM image calculated within the simple TH scheme (see figure 3.12) very much resembles the experimental STM images of A_1 . In both the experimental and the calculated images, a depression of ~ 0.1 Å appears on the bridge site, since the oxygen atom adsorbed in the adjacent fcc site depletes the LDOS at E_F . An asymmetry exists in the calculated image. However, since the calculated diffusion barrier is small (0.04 eV) for an O atom moving across the ridge, an O atom is expected to flip back and forth between the fcc sites on each side of a ridge in figure 3.6 with a frequency of ~ 100 GHz at 160 K. The calculated STM image for model (1) in figure 3.12 has been averaged accordingly, and it therefore appears symmetric as the experimental images. Thus, it is concluded that the individual depressions A_1 are associated with single oxygen atoms chemisorbed in the fcc sites.

In the calculated STM image for model (2), oxygen induces a depression on the bridge site similar to model (1). Due to the periodic boundary conditions invoked in the calculations, model (2) therefore represents a

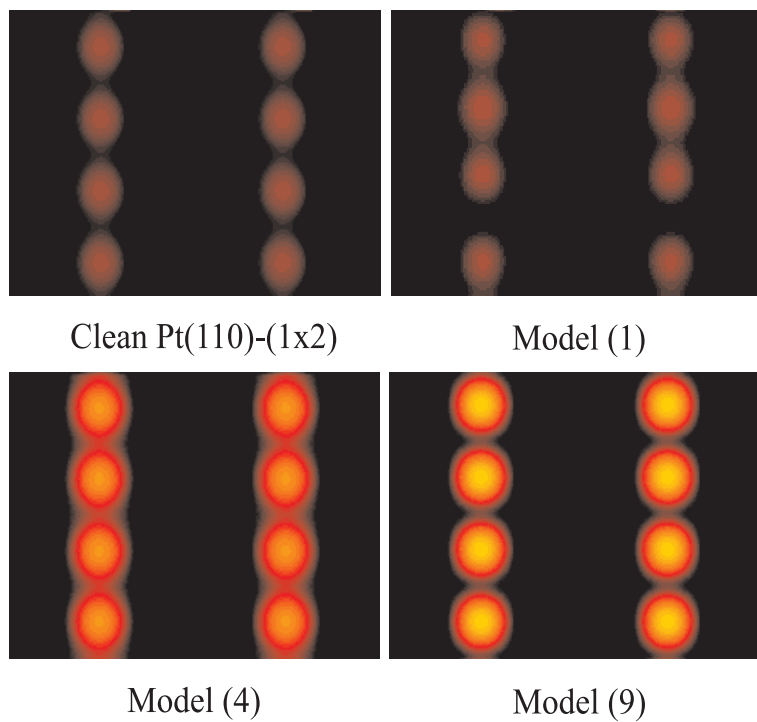


Figure 3.12: Simulated STM images for the clean Pt(110)-(1 \times 2) surface, model (1), (4) and (9) in figure 3.11. For the asymmetric models (1) and (4), the averages of the images with oxygen on either sides of the ridge are shown.

structure with double periodicity. This is the most stable configuration of all the configurations. Thus, it is energetically favorable for the oxygen atoms in model (1) to merge into the double-periodic structure (2) as the oxygen coverage is increased, in accordance with the experimental findings for A_1 and A_2 .

At higher oxygen coverages, the additional structures appearing on the surface are all characterized by bright protrusions localized at lattice positions. These protrusions are associated with Pt atoms relaxing outwards from the surface. As seen from figure 3.11, the vertical relaxation of a ridge-Pt atom is indeed significant, if the Pt is coordinated to at least two oxygen atoms sitting diagonally across the ridge-Pt atom.

The bright, isolated protrusion A_3 is associated with model (3) in figure 3.11. Both models (3) and (4) should in this connection be considered, since they are both among the five low-energy configurations. The local oxygen coverage, θ_O^{loc} , for models (3) and (4) is $\frac{2}{3}$ ML and 1 ML, respectively. From the calculations model (4) appears to be 40 meV more stable than model (3). One must be careful with so small energy differences, in particular since the long-range elastic interaction is different in the model (using small unit cells) and in the experimental situation. Model (3) gives, however, the best description of observed features in A_3 , since an asymmetry exists between the γ -Pt and δ -Pt atoms. The γ -Pt atom with two oxygen neighbours in the adjacent fcc sites relaxes outwards by 0.42 Å, whereas the δ -Pt atom with only one neighbouring oxygen atom is only displaced slightly by 0.12 Å. As a consequence, model (3) describes a bump located on a ridge lattice position.

The observed structure A_7 can be explained as a chain of successive λ -Pt and ν -Pt atoms in model (7). The ν -Pt atom protrudes farther out than the λ -Pt atom, thus resulting in a double periodicity of bright protrusions. However, A_7 is less stable than both A_2 and A_3 .

At the highest coverages, the A_9 stripes (figures 3.2 and 3.7) can be described by model (9) as well as model (4). Both models are among the low-energy structures, they differ by only 40 meV in energy, and vertical relaxations of the ridge-Pt atoms is associated with both models. In configuration (9), the geometrical relaxation is 0.2 Å larger than in model (4), but in the calculated STM images of models (4) and (9) in figure 3.12, the protruding ridge-Pt atoms have almost the same height increase of ~ 0.4 Å. This is consistent with the fact that only one type of stripe has been observed experimentally with an apparent height ≈ 0.45 Å. The two models differ, however, by a factor of two in the local oxygen coverage. In a recent study by Walker *et al.* [38], the saturation coverage was found to be close

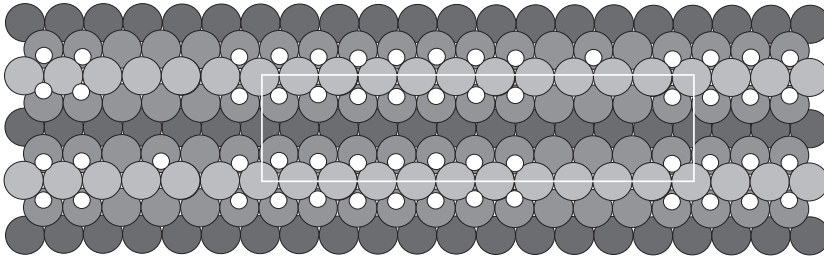


Figure 3.13: A ball model of an oxygen-induced (11×2) pattern. Oxygen atoms are shown as white balls and Pt as grey balls. The white rectangle indicates the unit cell of the superlattice.

to 2 ML. Therefore, the A_9 stripes are interpreted in terms of model (9). It cannot, however, be excluded that some of the stripes observed below saturation (as in figure 3.7) are associated with model (4).

Based on this picture, a model for the spatial distribution of oxygen atoms in the oxygen pattern is shown in figure 3.13. As in figure 3.2(d), the stripes are $6 \times a_{[1\bar{1}0]}$ long and separated by $5 \times a_{[1\bar{1}0]}$, which introduces a (11×2) superlattice. The oxygen coverage varies on different ridge segments between the stripes, as discussed in connection with figure 3.8.

In summary, the interplay between STM experiments and DFT calculations has provided a detailed picture of the complete range of oxygen-induced structures on Pt(110)-(1x2), from single oxygen atoms to a high-coverage surface oxide-like structure. At low oxygen coverages, the oxygen atoms are imaged as depressions at the bridge site, whereas oxygen induces vertical displacements of the ridge-Pt atoms at higher local coverages. These relaxations are directly observable in the STM and play a key-role in stabilizing the high-coverage structures.

3.3.4 Comparison with other studies

The structural complexity of the O/Pt(110)-(1x2) system clearly shows that STM is an ideal technique for studying this system, and the complexity also explains why previous studies based on integral techniques [5–11, 38] have not been successful in establishing a coherent structural picture. It has only been possible to obtain the novel picture presented in the previous section by combining STM and DFT. Applying these two techniques separately would not have provided a coherent description. Fur-

thermore, it appears that the new picture also explains the previous published results for oxygen on Pt(110)-(1×2). The following will discuss the more relevant studies.

Electron energy loss spectroscopy, EELS, has been applied by Schmidt *et al.* [7], to study the vibrational excitation of the oxygen atoms on Pt(110)-(1×2). The EELS spectra show energy losses corresponding to two vibrational frequencies of $\sim 480 \text{ cm}^{-1}$ and $\sim 330 \text{ cm}^{-1}$, respectively. In the original work, these frequencies were tentatively assigned to oxygen adsorbed in fivefold-coordinated trough sites and threefold-coordinated sites on the (111) micro-facets, respectively. However, the observed vibration frequencies agree with those calculated for the fcc site, and thus, the fcc adsorption site alone accounts for the EELS measurements.

During our investigation of O/Pt(110)-(1×2), we became aware of a similar study carried out at the same time by Walker *et al.* [38]. In this study, the dissociative adsorption of oxygen on Pt(110)-(1×2) is investigated by molecular-beam studies, TPD and LEED. Using molecular beams, the sticking probability of oxygen is measured by the King and Wells method [39]. The measured sticking probability and the flux in the molecular beam allow a determination of the oxygen coverage. The oxygen coverages are also obtained from TPD, in which the integral area under the TPD curves is calibrated using CO titration experiments. Oxygen coverage determinations should be treated carefully due to the very rough surface morphology of the Pt(110)-(1×2) surface (section 3.1). The reactivity changes near defects, and so does the amount of adsorbed oxygen [26, 40]. Walker *et al.* show by TPD of oxygen that defects contribute significantly to a high-temperature shoulder of the TPD spectra and that this contribution can be minimized by applying a sample preparation procedure involving oxygen treatments. Throughout their study, Walker *et al.* take into account the surface roughness by using the preparation procedure that minimizes the defect contribution. The corresponding LEED pattern of the clean surface has sharp spots. Thus, their coverage determinations are expected to largely reflect the oxygen coverages on the terraces. The important part of this study is the correlation of the measured oxygen coverages with the corresponding LEED patterns. Below an oxygen coverage of 1 ML, the (1×2) LEED pattern is retained at RT. In the light of the picture presented above, this is due to extremely mobile oxygen atoms, which ensure that no adsorbate structures exit on the average. When the oxygen coverage exceeds 1 ML, Walker *et al.* find that oxygen induces less intense satellite spots in the LEED patterns, which correspond to a (10×2) or (14×2) pattern depending on the actual oxygen coverage. This

superstructure corresponds to the oxygen pattern in figures 3.4 and 3.5. The saturation coverage is determined to be close to 2 ML. Based on their results alone, Walker *et al.* are not able to establish a well-founded model for the O/Pt(110)-(1×2) system. However, the coverage determination is important, since it provides additional information to the interplay between STM experiments and DFT calculations as discussed in the previous section.

Recently, a combined STM and DFT study of O/Pt(110)-(1×2) has appeared by Janin *et al.* [41]. In the reported STM images, small protruding strings are observed on the Pt ridges after an oxygen exposure of 5 L at RT. These strings correspond most likely to the stripes shown in figure 3.2. To interpret their STM results, Janin *et al.* perform hybrid DFT calculations modelling the Pt surface with a cluster containing a certain number of Pt atoms. It is found that atomic oxygen preferentially adsorbs at the bridge site on the Pt ridges, and that O adsorbed in the fcc site is more weakly bound by 1.2 eV. This deviates significantly from the DFT results discussed previously. However, cluster calculations are generally known to be less accurate than slab calculations as those discussed in section 3.3.2. If the clusters employed in the cluster calculations are too small, it is difficult to obtain accurate chemisorption energies. This is likely the reason why the cluster calculations by Janin *et al.* differ from the slab calculations reported in section 3.3.2. Based on their calculations, Janin *et al.* attribute the bright strings to oxygen chemisorbed in bridge sites, even though their STM images do not provide the detailed atomic-scale structure of the bright strings. Furthermore, the model proposed by Janin *et al.* does not account for the saturation coverage reported by Walker *et al.* [38], and it cannot account for the variety of oxygen-induced structural elements observed in the comprehensive STM study presented here. Janin *et al.* have not reported such a thorough study, and it appears that they have not discovered the complexity of the O/Pt(110)-(1×2) system.

3.3.5 Stabilizing high-coverage structures

It is surprising that the stripe structure A_9 develops with $\theta_O^{loc} = 2$ ML, corresponding to a density of 9.2×10^{14} (O atoms)/cm⁻². Usually O–O interactions on metal surfaces are repulsive [42, 43], leading to low saturation coverages. For oxygen adsorption on the close-packed Pt(111) surface, for instance, $\theta_O = 0.25$ ML (corresponding to 3.7×10^{14} (O atoms)/cm⁻²) at saturation, leading to a p(2×2) structure [42].

In the following, the reason for the lifting of the ridge-Pt atoms and

for the coupling of the lattice distortion to the stabilization of the high-coverage structures will be discussed. The coupling between the vertical displacement of the ridge-Pt atoms and the oxygen adsorption energy can indeed give rise to an *effective* O–O attractive interaction. Let us split the change in the oxygen adsorption energy $\delta E_{ads}(z)$ with the Pt displacement z into the energy change $\delta E_{Pt}(z)$, due to the displacement of the Pt atoms from the relaxed position z_0 in the absence of the oxygen atoms, and the change in the O–Pt bond strength $\delta E_{O-Pt}(z)$:

$$\delta E_{ads}(z) = \delta E_{Pt}(z) + \delta E_{O-Pt}(z) \quad (3.1)$$

$$\simeq Nk(z - z_0)^2 + \frac{\partial E_O}{\partial \epsilon_d} \frac{d\epsilon_d}{dz}(z - z_0). \quad (3.2)$$

The first term $\delta E_{Pt}(z)$, which is positive, is elastic of origin and thus quadratic in the displacement around the equilibrium height z_0 . It is given by the vertical stiffness of the surface k and the number N of Pt atoms, which have to be moved per O atom, i.e. $N = 1/\theta_O^{loc}$.

The second term $\delta E_{O-Pt}(z)$, on the other hand, is negative (i.e. the larger z , the stronger the O–Pt bond). This is explained by the electronic interaction between the O $2p$ valence states and the Pt bands.

The bonding of an adsorbate to a transition metal surface can be viewed as a two-step process (figure 3.14) [28, 44]: In the first step, the adsorbate valence states (O $2p$) interact with the metal s electrons (Pt $6s$). The broad continuum of the s states broadens the valence state and shifts it down in energy, as described in the Newns-Anderson model [45, 46]. The O $2p$ derived resonance states are below the Fermi level and therefore completely filled [29]. This may explain the repulsive O–O interaction in terms of either Pauli repulsion resulting from orbital overlap [43] or electrostatic interaction [47]. In the second step, the coupling to the localized Pt $5d$ bands is turned on. Since the metal d bands are narrow, a splitting into bonding and anti-bonding hybrid states with respect to the adsorbate and metal d states occurs.

This interpretation of the changes in the electronic structure provides an understanding of how the chemisorption energy changes when local properties of the adsorption site are varied [28, 40, 44, 48–50]. The binding energy can be considered as consisting of two contributions: One from the coupling to the Pt s states and one due to the interaction with the Pt d states [28, 44]. The metal s states give the major contribution to the adsorption energy, but since the bands are broad and featureless, this contribution is approximately the same for the different transition metals. On the other hand, the d bands are narrow due to the small coupling ma-

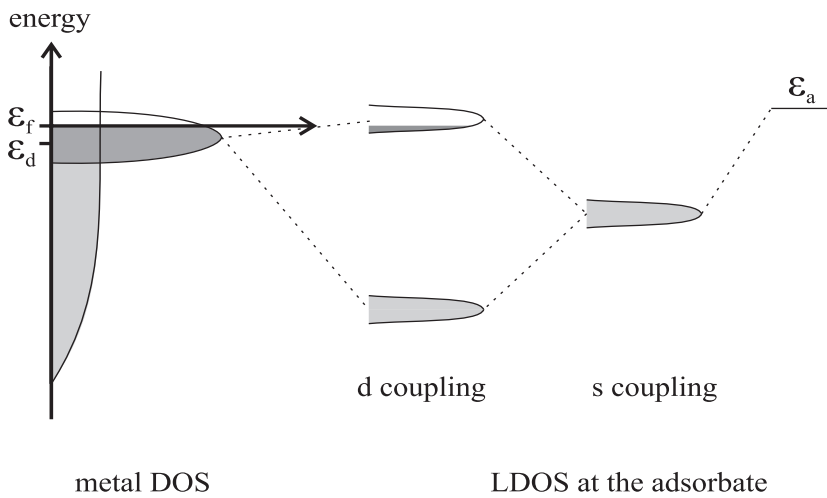


Figure 3.14: Schematic illustration of the local density of states (LDOS) at an adsorbate on a transition metal surface. The atomic valence state ϵ_a (e.g. one of the O $2p$ levels) is first broadened and shifted down in energy due to interaction with the metal s band (light grey area in the metal density of states (DOS)). Then the interaction with the metal d bands (dark grey area in the metal DOS) is turned on, and bonding and antibonding states are formed. ϵ_f is the Fermi level. The main trends in the chemisorption energies are given largely by the variations in the position of the d band center, ϵ_d .

trix element between the localized metal d orbitals on neighbouring metal atoms. Small changes in the metallic environment will therefore introduce significant modifications in the d states and hence their interaction with the adsorbate [50]. Thus, in this description, the main trends in the chemisorption energies are given largely by the coupling to the metal d states and follow closely the variations in the position of the d band center (ϵ_d). An upshift in ϵ_d forces more anti-bonding states to pass the Fermi level and become empty, resulting in a stronger bond to the surface.

In this picture, variations in the strength of the O-Pt bond result largely from shifts of the Pt d -bands. This is the explanation for the second term in (3.2). An outward relaxation of the ridge-Pt atoms results in a smaller overlap of the d states on neighbouring Pt atoms, so the width of the d bands decreases. To keep the d electron occupancy fixed, the d states have to shift up in energy, and this makes the O-Pt bond stronger [50]. Thus, the

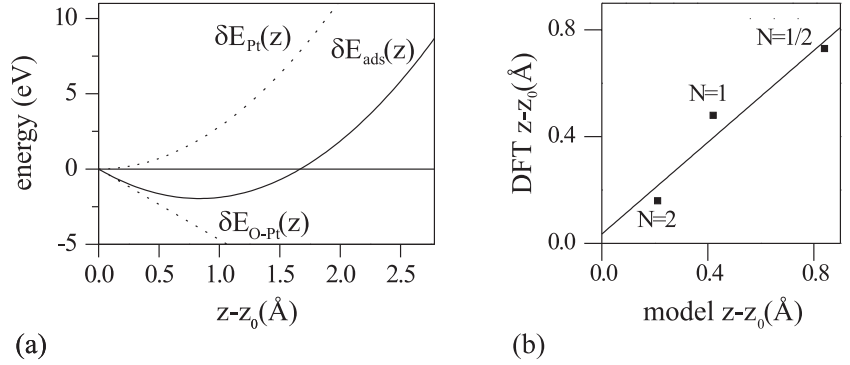


Figure 3.15: (a) Model calculations of the variation of the adsorption energy $\delta E_{ads}(z)$ with displacement ($z - z_0$) of the Pt overlayer for $N = 1/2$. (N is the number of Pt atoms that must be displaced per oxygen atom, $N = 1/\theta_o^{loc}$). The two contributions $\delta E_{Pt}(z)$ and $\delta E_{O-Pt}(z)$ in equation 3.2 are also shown (dashed curves). (b) A comparison between the equilibrium displacements from the DFT calculations and the simple model as a function of N . Only the most stable cases, in which oxygen atoms are placed diagonally across a ridge-Pt atom, are included.

coupling between lattice distortion and adsorption energy is established.

From the DFT calculations of the oxygen adsorption energy in different threefold sites on the surface, the calculations give $\partial E_O/\partial \epsilon_d = -4.27$, and calculations for the clean surface give $d\epsilon_d/dz = 1.10 \text{ eV}/\text{Å}$ and $k = 5.62 \text{ eV}/\text{Å}^2$. With these parameters all terms in equation (3.2) are defined and the result are illustrated in figure 3.15.

The model explains the origin of the outward relaxations of the Pt atoms as a competition between an elastic and an electronic term. This relaxation results in an effective attractive contribution to the O–O interaction given by the minimum of $\delta E_{ads}(z)$. From (3.2), it is seen that an increasing θ_o^{loc} increases the relaxation, as also shown in figure 3.15. This attractive interaction compensates the repulsive O–O interaction and thereby stabilizes the high-coverage structures (see tabel 3.1). The open structure of the (110) surface is what makes high oxygen coverages possible: With only seven nearest-neighbours for the ridge atoms, the stiffness k is small. At the same time, it is geometrically possible for N to become very small ($1/2$ for structure (9)). The simple model does not explain why there are different relaxations for models (4), (5) and (6) — configurations

where the ridge-Pt atoms have the same oxygen coordination. It can be due to local changes in the electronic structure [51], but further studies are required to elucidate that.

The coupling between lattice relaxations and adsorbate-adsorbate interactions and the coupling between the adsorbate-surface interaction strength and the d -band center have general implications for other metal-adsorbate systems. The effect may lead to a weakening of the repulsive adsorbate-adsorbate interactions, and it may even lead to an attraction on open surfaces. It also explains the oxygen-induced restructuring of Cu, Ni, Ag, Pd and Rh surfaces where the surface metal-metal bonds are broken giving rise to a lower metal coordination number, higher lying d -band, and an effective increase in the oxygen adsorption bond strength [52].

3.4 The self-assembled oxygen nanostructure

Currently, the spontaneous formation of periodic patterns on surfaces with nanoscale dimensions is shown a lot of interest, since it offers the possibility of tailoring surfaces with new physical and chemical properties, and since it opens up new possibilities for material processing technologies in which the patterns are used as templates for subsequent epitaxial growth [53–58]. The following section will describe the self-organized oxygen nanostructure in more detail, and the implications of the oxygen pattern will be discussed in the concluding part of this chapter.

3.4.1 Experimental results

As the Pt(110)-(1×2) surface is exposed to oxygen, oxygen-induced stripes form and tend to align into bands oriented along the [001] direction. Due to this alignment, a two-dimensional nanostructure emerges as shown in figures 3.2 and 3.4. Dynamical changes in the ridge-structures during the pattern formation are visualized in figure 3.16. A linescan along a $[\bar{1}\bar{1}0]$ ridge is collected from each image in an STM movie (sample temperature 357 K) and plotted versus the oxygen exposure. The resulting image shows when the individual stripes nucleate and how the length and/or the position of the stripes subsequently fluctuate. In a microscopic view, a change in the length or the position of a stripe happens when the exchange of oxygen between the stripe phase and the surroundings forces Pt atoms in the ridges to relax outwards or inwards, depending on whether oxygen moves to or away from a stripe.

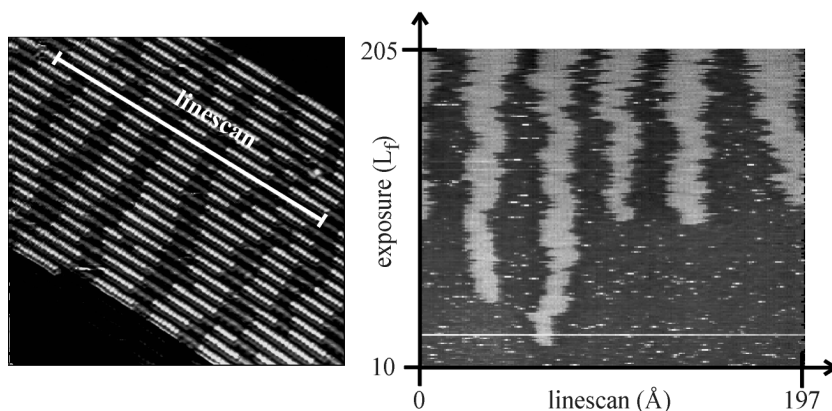


Figure 3.16: Illustration of the dynamic fluctuations along a $[1\bar{1}0]$ ridge at a substrate temperature of 357 K. Linescans from a ridge segment (illustrated in the STM image to the left) are collected from successive images in an STM movie and shown versus exposure (image to the right). Each of the bright bands in the resulting image represents the time evolution of a stripe. The image acquisition time is 8.3 s. The linescans are compensated for drift.

A quantitative analysis of the fluctuations in the stripe lattice provides further insight into the interactions between the stripes. The center of mass (CM) of a stripe at time t relative to the mean position along $[1\bar{1}0]$ is defined by $u(t) = r_{CM}(t) - \langle r_{CM} \rangle$. A record of $u(t)$ can be obtained for each individual stripe by tracking its end points during a movie (section 2.3.3). Such a data set is obtained for an oxygen pattern, which is filmed at 357 K after the oxygen exposure is terminated. Figure 3.17 shows correlations between the CM displacements of nearest-neighbour stripes along and perpendicular to the Pt ridges. In both cases, the positive skewness of the distributions reflects a positive correlation in the displacement of nearest-neighbour stripes, indicating a repulsive interaction along the $[1\bar{1}0]$ ridges and an attractive interaction across the troughs.

Furthermore, the analysis shows that the fluctuations in the stripe lattice occur frequently. For instance, about 70% of the stripes are displaced from image to image with an image acquisition time of 8.3 s. This suggests that oxygen patterns formed at substrate temperatures above 357 K are

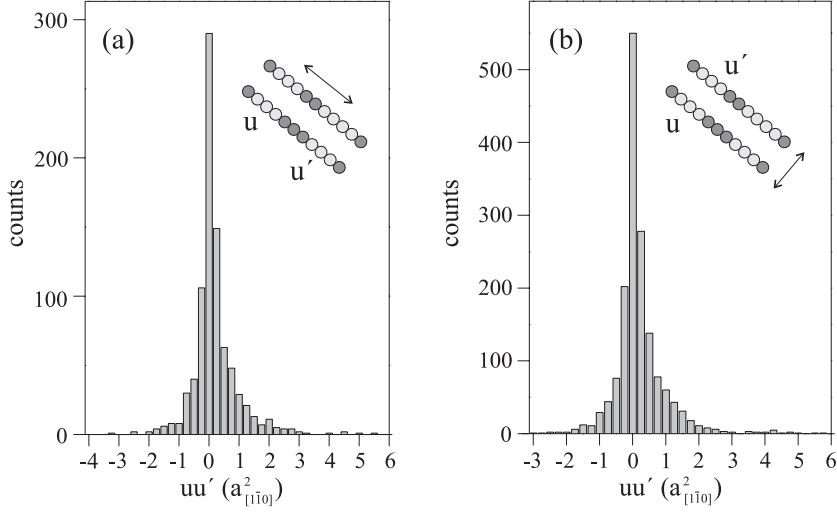


Figure 3.17: Distributions of the product uu' for nearest-neighbour stripes along (a) the $[1\bar{1}0]$ direction and (b) the $[001]$ direction. The correlations are illustrated by the inserted ball models of two adjacent ridges, where the light balls indicate the lifted Pt atoms in stripes. The analysis includes 42 stripes. The movie is acquired under UHV conditions at 357 K. The image acquisition time is 8.3 s. In (a), the mean value is $\langle uu' \rangle = 0.2a_{[1\bar{1}0]}^2$ and the skewness is $\kappa = 3.2$. In (b), the mean value is $\langle uu' \rangle = 0.2a_{[1\bar{1}0]}^2$ and the skewness is $\kappa = 2.7$.

close to equilibrium. At RT, it is observed directly in the STM movies that such dynamic stripe fluctuations are almost quenched.

In order to study the oxygen pattern in greater detail, a series of experiments have been performed in which the oxygen exposure, and hence the stripe coverage, has been varied. After sputtering and annealing to 980 K, the cooling is stopped at a given substrate temperature, and the sample is exposed to oxygen at a constant background pressure. The sample is subsequently cooled under UHV conditions to RT at a rate of ~ 1 K/s, and finally, the sample is transferred to the STM, where scanning is done at RT.

In the experiments, a background pressure of oxygen has been used in the range $1.0 \times 10^{-8} - 1.0 \times 10^{-6}$ mbar. For this range, it is found that the pressure as such does not influence the length of the stripes and the periodicity along the $[1\bar{1}0]$ ridges.

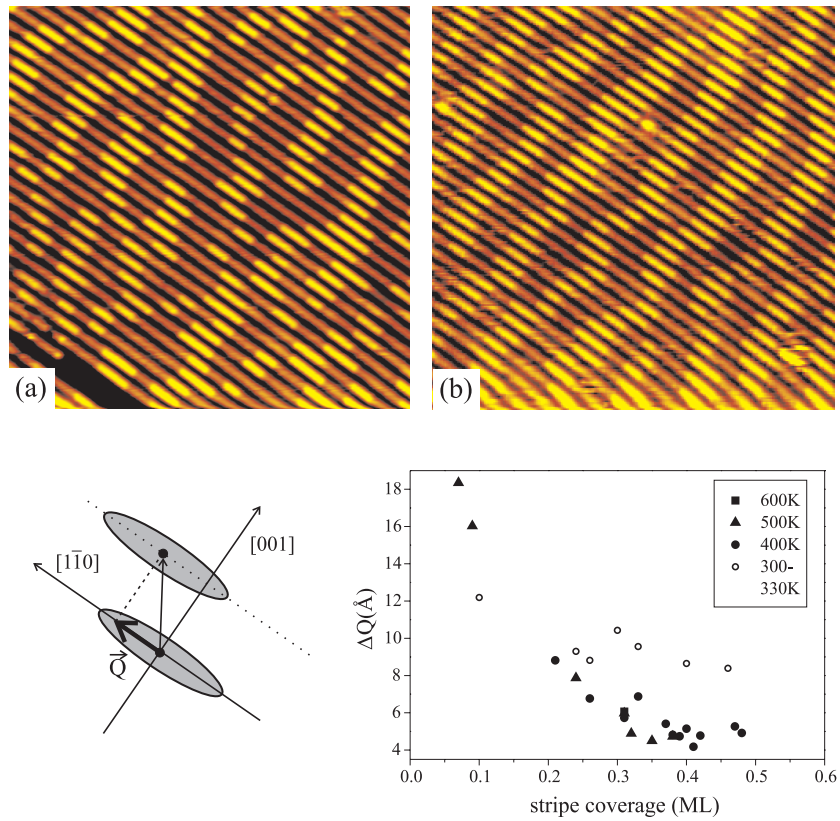


Figure 3.18: The effect of the substrate temperature on the alignment of the stripes. The oxygen patterns shown in the STM images are formed at 309 K (a) and at 400 K (b). The stripe coverage is 0.46 ML in (a) and 0.49 ML in (b). The size of the images is $211 \times 252 \text{ \AA}^2$. At the bottom, the sketch illustrates two stripes (grey ellipses) on adjacent ridges. The inter-stripe vector connecting the CM of the stripes projected onto the $[1\bar{1}0]$ direction is \vec{Q} . The standard deviation of the distribution of $|\vec{Q}|$, termed ΔQ , measures the extent to which the alignment is perfect. ΔQ is shown versus the stripe coverage for oxygen patterns formed at different substrate temperatures.

The influence of the temperature on the stripe alignment along [001] is illustrated by the STM images in figure 3.18. To quantify the alignment, we consider the distribution of [1 $\bar{1}$ 0] projections of inter-stripe vectors, \vec{Q} , connecting the center of mass of stripes nearest to each other on neighbouring ridges (see figure 3.18). The standard deviation of the distribution of $|\vec{Q}|$, termed ΔQ , is zero for stripes perfectly aligned in the [001] direction, and ΔQ increases as the alignment is deteriorated. ΔQ is therefore a measure of the ordering of the stripes. Figure 3.18 shows ΔQ as a function of the stripe coverage for patterns formed at different conditions. ΔQ is found to be independent of the oxygen pressure. For stripe coverages above ~ 0.25 ML, ΔQ is smallest for substrate temperatures at or above 400 K, and a nearly perfect alignment is achieved. Thus, in agreement with the dynamical data discussed above, this suggests that oxygen patterns formed at elevated substrate temperatures equilibrates into well-ordered, one-dimensional nanostructures.

Below stripe coverages of ~ 0.25 ML, ΔQ is found to increase with decreasing coverages. This is due to a reduced stripe density (figures 3.2(b) and (c)) - a low stripe density makes it less likely that stripes are located near each other on adjacent ridges, resulting in large $|\vec{Q}|$. It also implies that the stripe coverage must exceed a certain value before it is reasonable to say that an oxygen pattern has emerged at all. By visual inspection of the STM data, the critical stripe coverage, above which the oxygen pattern is formed, is found to be ~ 0.15 ML.

The following will focus on well-ordered, coherent oxygen patterns formed at substrate temperatures of 400 K, 500 K and 600 K. For such patterns, two characteristic lengths are of interest - the length of the stripes and the periodicity along the Pt ridges. These parameters are sketched in figure 3.19. The periodicity d is measured as the distance between ends of nearest-neighbour stripes along a [1 $\bar{1}$ 0] ridge. The average value and standard deviation of the d -distribution are obtained from 100-200 observations for a given stripe coverage and are shown in figure 3.20 as a function of the stripe coverage. At stripe coverages below ~ 0.15 ML, the large error bars indicate that no characteristic periodicity has evolved, whereas the much more narrow distributions of d for stripe coverages above ~ 0.15 ML reflect that a periodic pattern has emerged. The mean periodicity is large at low stripe coverages and decreases to a value of 10–12 nearest-neighbour distances with increasing stripe coverage (as in figures 3.4 and 3.5). The length of the stripes l is also measured. The mean value and the standard deviation of the l -distribution are obtained from 100-200 observations for a given stripe coverage and are shown in figure 3.20. The length of the

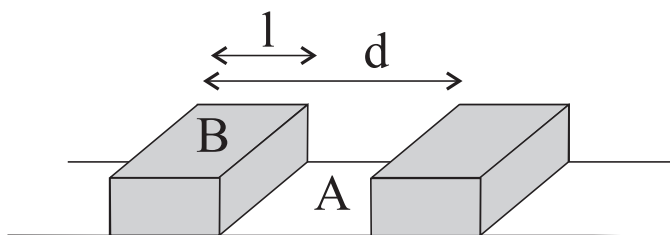


Figure 3.19: Sketch of a one-dimensional pattern of two alternating phases, A and B. The width of phase B (to be imagined as the $[001]$ oriented bands of oxygen-induced stripes) is l , and the periodicity introduced by the pattern is d .

stripes is found to increase with increasing stripe coverage. Independent of the substrate temperature, the periodicities and the lengths of the stripes are observed to be described by common curves for stripe coverages above 0.15 ML (figure 3.20). These curves will be discussed later on.

One remaining question is why no data exists for l and d above a stripe coverage of 0.5 ML in figure 3.20. For oxygen patterns formed at 400 K or above, it appears that the stripe coverages saturate at values at or below 0.5 ML. Exposure to oxygen at RT can, however, almost saturate the surface with oxygen-induced stripes. As discussed in relation to figure 3.10, the lattice distortions begin at a stripe coverage of ~ 0.8 ML. At present, the reason for this difference between oxygen dosage at higher temperatures and RT is unclear. It should be noticed that the hydrogen and carbon monoxide partial pressures increase, when high oxygen exposures are performed, and that the rise in the CO concentration is significant, when the filament used for heating the sample is turned on. More specifically, the CO partial pressure is two orders of magnitude lower than the O_2 pressure of 5.0×10^{-7} mbar. The hydrogen partial pressure is lower by three orders of magnitude. Although the CO pressure increases, CO titration of the adsorbed oxygen seems unlikely, since a simple estimate shows that the CO partial pressure should be six times higher than that measured in order to account for the low saturation coverages of the stripes. Oxygen does not go subsurface, according to the discussion in section 3.3.2. Another possible explanation is that the sticking coefficient of oxygen approaches zero. The recent study by Walker *et al.* [38] reports on the coverage dependence of the sticking coefficient. Initially, the temperature-dependent sticking probability is high (~ 0.3) and drops with increasing oxygen coverage to

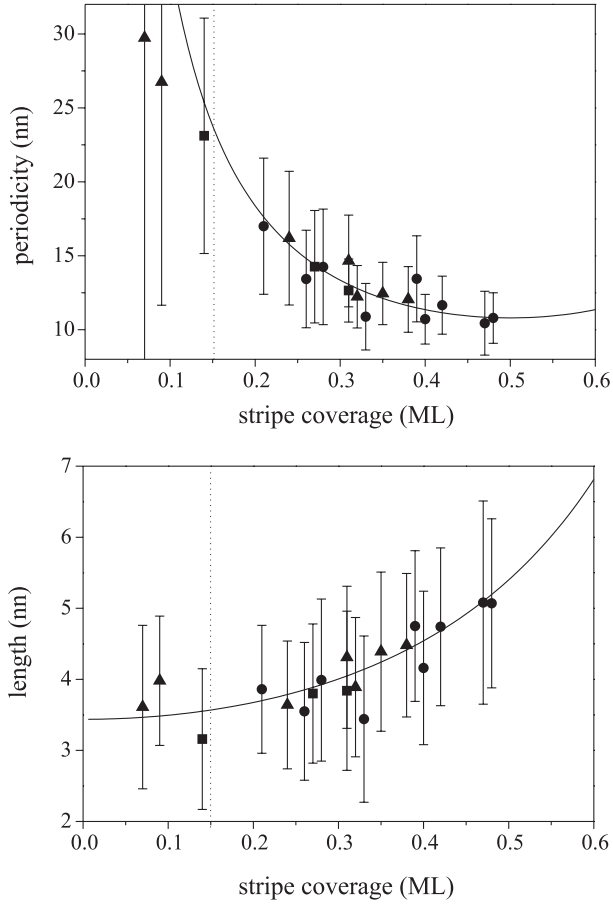


Figure 3.20: The stripe periodicity (d) and length (l) versus the stripe coverage. d and l are defined in figure 3.19. Each data point represents the average over 100-200 observations and the error bars show the standard deviation of the corresponding distributions. Each data point corresponds to a sample preparation using an oxygen pressure of 5.0×10^{-7} mbar and substrate temperatures of 400 K (circles), 500 K (triangles) or 600 K (squares). nm is the nearest-neighbour distance $a_{[1\bar{1}0]}$. The vertical, dotted lines indicate the stripe coverage above which an oxygen pattern has evolved.

a low and constant value of ~ 0.03 for oxygen coverages exceeding a level of 0.5 ML. For oxygen coverages above 1 ML, no information is reported concerning the sticking-coefficient of oxygen.

3.4.2 Discussion

A wide variety of two-dimensional systems spontaneously form periodic patterns in equilibrium [59]. Examples of such patterns include the characteristic herringbone reconstruction on Au(111) [60, 61] and the piano-board structure of [001] oriented O–Cu–O chains on Cu(110) [53]. In these examples, the pattern formation is accounted for by a generic model based on the work by Marchenko [62] and Vanderbilt [63, 64]. The self-organization is regarded as originating from elastic interactions in the surface region. In the following, the model will be described briefly and used to shed some light on the formation of the self-assembled oxygen pattern on Pt(110)-(1×2).

Consider the sketch in figure 3.19 of a one-dimensional pattern of alternating phases A and B, each associated with different surface stress tensors. The pattern forms if it is energetically favoured compared to the low-energy phase (assumed to be A). The change in the surface free energy per unit area associated with the introduction of the B phase with a width l_B is [65]

$$\Delta F = \theta \Delta F_0 + \frac{2C_1}{d} - \frac{2C_2}{d} \ln\left(\frac{d}{2\pi a} \sin(\pi\theta)\right). \quad (3.3)$$

θ is the coverage of the B phase, and $\Delta F_0 = F_B - F_A$ is the surface free energy difference per unit area between the B and the A phase. If ΔF_0 is large (positive or negative) compared to the two large terms, a single domain of either A or B will emerge. Hence, to describe the formation of a domain structure, the model presumes that ΔF_0 is small. The sum of the last two terms is the energy change associated with the formation of the domain walls between A and B. The creation of a domain boundary reflects an energy cost C_1 per unit length along [001]. In the present case, the energy cost is associated with the reduced coordination of the lifted ridge-Pt atoms at the stripe ends. The factor of two appears since two domain walls are formed per period. The difference in stress between the two phases gives rise to an elastic relaxation at the domain boundary, resulting in a lowering of the surface energy. According to elasticity theory, this is given by the last term. The prefactor C_2 is a function of the elastic constants of the surface and the difference in the surface stress between

the two phases. a is a microscopic cut-off which is introduced to prevent divergence in the calculations of the C_2 term. a is to be interpreted as the domain wall width.

Minimizing the energy in (3.3) for constant coverage yields the equilibrium periodicity and length of B [63]

$$d(\theta) = \frac{\kappa}{\sin(\pi\theta)} \quad l(\theta) = \frac{\kappa\theta}{\sin(\pi\theta)}, \quad (3.4)$$

where $\kappa = 2\pi a \exp(1 + C_1/C_2)$. $\theta = l/d$ for the periodic pattern in figure 3.19, providing the expression for $l(\theta)$. For the periodicity in (3.4), the competition between the two last terms in (3.3) results in a negative contribution to ΔF . The characteristic lengths of the domain structure are a trade-off between the energy cost (C_1) associated with the formation of the domain walls and the energy gained from elastic interaction across the boundaries (C_2). If C_1 is dominating, a large value of l results in order to reduce the density of boundaries. If, on the other hand, C_2 dominates, narrow domains form.

Before proceeding, it is noticed that the elastic interaction is related to the problem of elastic step-step interactions. Actually, it can be shown that the strain relaxation effectively introduces an $1/r^2$ repulsive interaction energy between the boundaries; r being the domain wall separation [66]. Besides elastic interactions, electrostatic interactions, resulting from a difference in the work functions between the two phases, are also capable of giving rise to the formation of periodic domain structures. The theory provides a result analogous to (3.3) with C_2 depending on the work function difference [63]. The similarity is due to the fact that the electrostatic interaction energy between surface dipoles and the interaction energy between surface stress elements scale as $1/r^3$. In general, C_2 is to be interpreted as the sum of both the elastic and the electrostatic contributions [63].

From a microscopic point of view, both elastic and electrostatic interactions are expected to be involved in the formation of the oxygen nanostructure on Pt(110)-(1×2) since the Pt lattice is highly strained in the oxygen-induced stripes and charge is transferred towards the oxygen in this phase.

From the static studies of the equilibrated oxygen patterns on Pt(110), the mean periodicity and stripe length are shown in figure 3.20. The curves in this figure represent the best fit of the expressions for $d(\theta)$ and $l(\theta)$ to the data for stripe coverages above 0.15 ML only, and there appears to be a good agreement. The generic stress model describes a periodic domain

pattern, and for this reason, a comparison with the experimental data is not physically reasonable for stripe coverages below ~ 0.15 ML, where an ordered oxygen pattern has not clearly emerged.

The value of κ providing the best fit in figure 3.20 for stripe coverages above 0.15 ML is determined to $\kappa = 10.7 \times a_{[110]}$. κ contains the ratio C_1/C_2 , but also the microscopic cut-off. Since a is not *a priori* fixed, a quantitative determination of the C_1/C_2 is inhibited. Assuming $a = 0.5a_{[110]}$, the ratio of the two competing energies is $C_1/C_2 = 0.23$, or stated differently, since $C_1/C_2 > 0$, the value for κ gives an upper limit of the domain wall width $a < 1.6\text{\AA}$. The present framework does not provide further possibilities for quantifying the characteristic energies. An interplay with a more detailed theoretical study of the pattern formation in the O/Pt(110)-(1×2) system would in this respect be useful.

The O/Pt(110) system resembles O/Cu(110). For that system, [001] oriented O–Cu–O rows are formed, when Cu(110) is exposed to oxygen. These rows spontaneously self-organize into [001] oriented oxide bands, which are separated by bands of the bare Cu(110) surface [53, 67, 68]. The oxide band structure extends over a mesoscopic length scale and even straight across step edges. The periodicity of the oxygen pattern has been measured by He diffraction [53] as a function of the oxide band coverage, ranging from 0.2 ML to 0.8 ML. These observations are also accounted for by the expression for $d(\theta)$ in (3.4) [63, 69]. At lower oxygen coverages O/Cu(110) faces a regime, similar to the O/Pt(110) system, where no pattern and thus superperiodicity have evolved. The oxide bands in the O/Cu(110) pattern are much more straight than those in the O/Pt(110) system, which is probably due to the chemical bonds linking the O–Cu–O units together.

Recently, Pohl *et al.* have actually succeeded in measuring the ordering forces responsible for the self-organization of a surface nanostructure [54, 70]. STM movies of a hexagonal lattice of vacancy islands in a Ag film on Ru(0001), formed by S exposure, are acquired. Correlation plots similar to those presented in figure 3.17 are obtained by analyzing the displacements of the vacancy islands around their equilibrium positions in the hexagonal lattice. The information in these plots is combined with an elastic description of the repulsive interaction between the vacancy islands, and this allows a quantitative determination of the C_2 parameter.

The application of a similar procedure to the O/Pt(110) pattern would be an obvious move. The oxygen pattern is more complicated due to the anisotropic interactions between the individual stripes, as opposed to the pure repulsive interaction between the hexagonally arranged vacancy

islands in the Ag film. Again, a theoretical description of the anisotropic interactions between the oxygen-induced stripes is needed for establishing the link between the dynamical data and the interaction energies.

In conclusion, STM experiments show that the oxygen-induced stripes have a strong tendency to align along the [001] direction, and so a periodic pattern forms. For stripe coverages less than ~ 0.15 ML, the pattern is not clearly developed. For intermediate stripe coverages up to 0.50 ML, the best ordering is obtained, when oxygen patterns are formed at substrate temperatures above 400 K. For such patterns, the generic model for stress domain formation accounts for the observed variation in the period and length of the stripes. A more quantitative description of the long-range interactions governing the self-organization requires further interplay with theory.

3.5 Summary and outlook

In summary, an interplay between STM experiments and DFT calculations has provided a detailed picture of oxygen-induced structures on Pt(110)-(1 \times 2). A small number of structural elements is shown to describe all the surface structures from the very first adsorbed oxygen atoms to the formation of a new high-coverage oxide-like structure. It is shown that lattice distortions, directly observable in the STM, couple to the oxygen adsorption energy, which greatly stabilizes the high-coverage structures. Long-range interactions cause a spatial self-organization of the high-coverage oxide-like structure, so a periodic nanostructure emerges.

The detailed picture of O adsorption is important for understanding surface reactions on Pt(110)-(1 \times 2). The CO oxidation reaction on this surface has attracted much interest. Under certain reaction conditions, PEEM shows that patterns form on a mesoscopic length scale and exhibit a cyclic or even chaotic behaviour in space and time [32]. Currently, STM studies are pursued to reveal the atomic-scale details in this reaction and also in the water formation process. Four snapshots from an STM movie obtained during hydrogen titration of oxygen are shown in figure 3.21. Hydrogen adsorbs and reacts with oxygen to form water [71], which eventually desorbs from the surface [72]. These preliminary results show that the removal of oxygen from the oxygen-induced stripes proceeds from the stripe ends, i.e. a one-dimensional reaction. In modelling macroscopic reaction rates, a mean-field approximation is usually adapted, yielding reaction rates that scale with the product of the reactant coverages. However, the

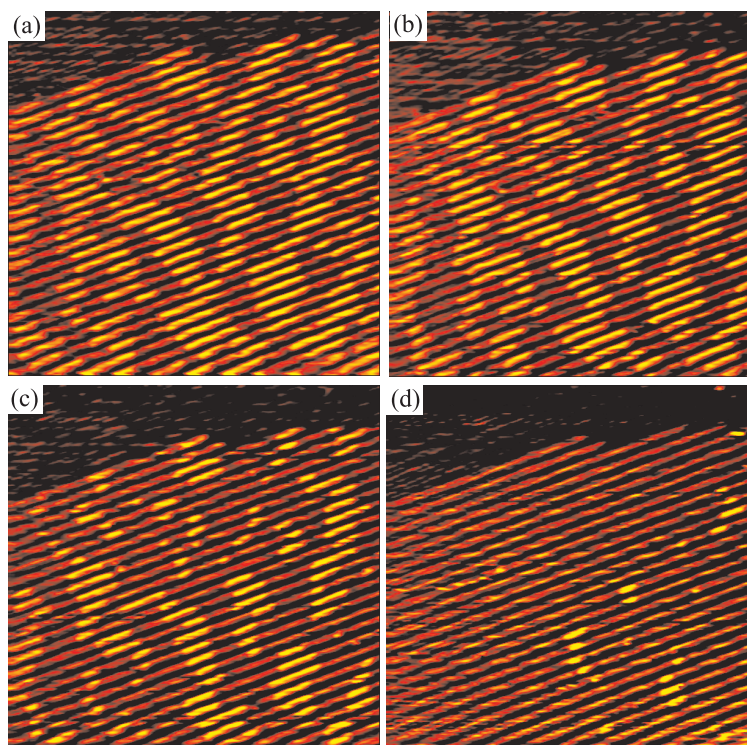


Figure 3.21: Snapshots from an STM movie showing the hydrogen titration of oxygen. (a) An oxygen pattern formed by oxygen adsorption at RT. Hydrogen exposure is (b) $0.24 L_f$, (c) $0.38 L_f$ and (d) $0.83 L_f$. Hydrogen inlet to a chamber pressure of 2.2×10^{-9} mbar. Sample temperature 304 K.

oxygen pattern clearly demonstrate that the reactants are not randomly distributed on the surface. A detailed analysis of the STM movies reveals that the stripe coverage reduces by a rate scaling with the number of stripe ends. Thus, the mean-field rate-equation formalism seems to break down at the atomic level. Currently, there is an increasing interest in exploring such microscopic aspects of surface reactions [71, 73–77].

Adsorbate patterns can also be used as templates in epitaxial growth [56, 78]. The STM images in figure 3.22 show a submonolayer of platinum deposited onto (a) a clean Pt(110)-(1×2) surface and (b) an oxygen nanostructure. On the oxygen nanostructure, platinum is confined to grow

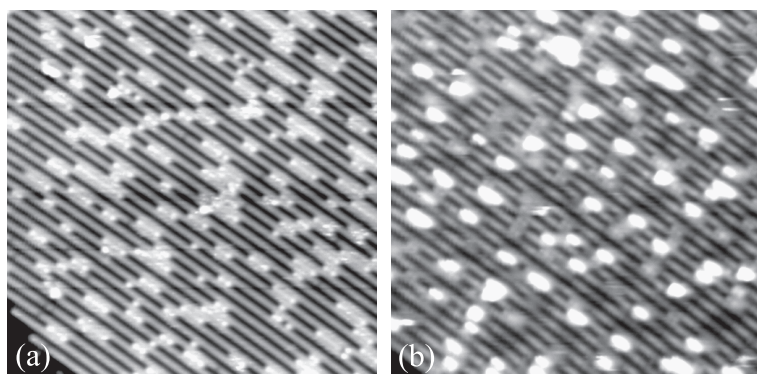


Figure 3.22: Platinum (~ 0.2 ML) deposited onto (a) a clean Pt(110)-(1 \times 2) surface and (b) an oxygen pattern grown at 400 K. Deposition is done at a substrate temperature of 327 K. Image size $242 \times 245 \text{ \AA}^2$.

in the regions in between the oxygen-induced stripes in one or two layer high islands. This confinement results in a very narrow length distribution of the Pt islands with an average length of $\sim 8 \text{ \AA}$. Thus, the oxygen pattern offers in principle a way to control the formation of novel metal nanostructures, such as one-dimensional nanogratings. There is currently a large emphasis on exploring such templated epitaxial growth, since it offers new and exciting possibilities for a controlled fabrication of nanostructures with well-defined sizes, shapes and positions at surfaces in a parallel process [55–57]. This will complement existing techniques based on scanning probes method [79, 80], cluster deposition [81–83], and lithography [84–86]. Chapter 5 will demonstrate how a model catalyst system consisting of a homogeneous ensemble of MoS₂ nanocrystals can be constructed using the periodic dislocation network on the reconstructed Au(111) surface as a template.

References

- [1] G. A. Somorjai, *Introduction to surface chemistry and catalysis* (John Wiley & Sons, Inc., New York, 1994).
- [2] G. Hoogers and D. Thompsett, *CATTECH* **3**, 106 (1999).
- [3] T. Zambelli, J. V. Barth, J. Wintterlin, and G. Ertl, *Nature* **390**, 495 (1997).
- [4] T. Engel and G. Ertl, in *The chemical physics of solid surfaces and heterogeneous catalysis, vol. 4*, edited by D. A. King and D. P. Woodruff (Elsevier scientific publishing company, Amsterdam, 1982).
- [5] N. Freyer, M. Kiskinova, G. Pirug, and H. P. Bonzel, *Surf. Sci.* **166**, 206 (1986).
- [6] Y. Ohno and T. Matsushima, *Surf. Sci.* **241**, 47 (1991).
- [7] J. Schmidt, C. Stuhlmann, and H. Ibach, *Surf. Sci.* **284**, 121 (1993).
- [8] J. Fusy and R. Ducros, *Surf. Sci.* **214**, 337 (1989).
- [9] A. von Oertzen, A. Mikhailov, H. H. Rotermund, and G. Ertl, *Surf. Sci.* **350**, 259 (1996).
- [10] M. Wilf and P. T. Dawson, *Surf. Sci.* **65**, 399 (1977).
- [11] R. Ducros and R. P. Merrill, *Surf. Sci.* **55**, 227 (1976).
- [12] R. J. Needs, M. J. Godfrey, and M. Mansfield, *Surf. Sci.* **242**, 215 (1991).
- [13] V. Fiorentini, M. Methfessel, and M. Scheffler, *Phys. Rev. Lett.* **71**, 1051 (1993).
- [14] J. Jacobsen, K. W. Jacobsen, and J. K. Nørskov, *Surf. Sci.* **317**, 8 (1994).
- [15] E. Vlieg, I. K. Robinson, and K. Kern, *Surf. Sci.* **233**, 248 (1990).
- [16] T. Gritsch, D. Coulman, R. J. Behm, and G. Ertl, *Surf. Sci.* **257**, 297 (1991).
- [17] K.-M. Ho and K. P. Bohnen, *Phys. Rev. Lett.* **59**, 1833 (1987).
- [18] P. Hanesch and E. Bertel, *Phys. Rev. Lett.* **79**, 1523 (1997).

- [19] K. Swamy, E. Bertel, and I. Vilfan, *Surf. Sci.* **425**, L369 (1999).
- [20] G. Binnig, H. Fuchs, and E. Stoll, *Surf. Sci.* **169**, L295 (1986).
- [21] N. D. Lang, *Phys. Rev. Lett.* **55**, 230 (1985).
- [22] N. D. Lang, *Phys. Rev. Lett.* **56**, 1164 (1986).
- [23] P. Sautet, *Chemical Reviews* **97**, 1097 (1997).
- [24] M.-L. Bocquet, J. Cerdà, and P. Sautet, **59**, 15437 (1999).
- [25] M. Bonn, S. Funk, C. Hess, D. N. Denzler, C. Stampfl, M. Scheffler, M. Wolf, and G. Ertl, *Science* **285**, 1042 (1999).
- [26] S. Dahl, A. Logadottir, R. C. Egeberg, J. H. Larsen, I. Chorkendorff, E. Törnqvist, and J. K. Nørskov, *Phys. Rev. Lett.* **83**, 1814 (1999).
- [27] P. J. Feibelman, *Phys. Rev. B* **56**, 2175 (1997).
- [28] B. Hammer and J. K. Nørskov, in *Theory of adsorption and surface reactions in Chemisorption and Reactivity on Supported Clusters and Thin Films, NATO ASI series E 333*, edited by R. M. Lambert and G. Pacchioni (Kluwer Academic Publishers, Dordrecht, Netherlands, 1997).
- [29] H. T. Lorensen, PhD thesis, Technical University of Denmark, Denmark, 1999.
- [30] D. Vanderbilt, *Phys. Rev. B* **41**, R7892 (1990).
- [31] J. P. Perdew and Y. Wang, *Phys. Rev. B* **33**, 8800 (1986).
- [32] H. H. Rotermund, *Surf. Sci. Rep.* **29**, 265 (1997).
- [33] A. Zangwill, *Physics at surfaces* (Cambridge University Press, Cambridge, Great Britain, 1996).
- [34] J. Wintterlin, R. Schuster, and G. Ertl, *Phys. Rev. Lett.* **77**, 123 (1996).
- [35] A. Bogicevic, J. Stromquist, and B. I. Lundquist, *Phys. Rev. B* **57**, R4289 (1998).
- [36] P. J. Feibelman, *Phys. Rev. B* **56**, 10532 (1997).

- [37] P. J. Feibelman, S. Esch, and T. Michely, *Phys. Rev. Lett.* **77**, 2257 (1996).
- [38] A. V. Walker, B. Klötzer, and D. A. King, *J. Chem. Phys.* **109**, (1998).
- [39] D. A. King and M. G. Wells, *Surf. Sci.* **29**, 454 (1972).
- [40] B. Hammer, O. H. Nielsen, and J. K. Nørskov, *Catal. Lett.* **46**, 31 (1997).
- [41] E. Janin, H. von Schenk, M. Göthelid, U. O. Karlsson, and M. Svensson, *Phys. Rev. B* **61**, 13144 (2000).
- [42] W. A. Brown, R. Kose, and D. A. King, *Chem. Rev.* **98**, 797 (1998).
- [43] Q. Ge, P. Hu, D. A. King, M. Lee, J. A. White, and M. C. Payne, *J. Chem. Phys.* **106**, 1210 (1997).
- [44] B. Hammer and J. K. Nørskov, *Adv. Catal.* to appear (2000).
- [45] D. M. Newns, *Phys. Rev.* **178**, 1123 (1969).
- [46] P. W. Anderson, *Phys. Rev.* **124**, 41 (1961).
- [47] W. Kohn and K.-H. Lau, *Solid State Commun.* **18**, 553 (1976).
- [48] B. Hammer and J. K. Nørskov, *Nature* **376**, 238 (1995).
- [49] B. Hammer, Y. Morikawa, and J. K. Nørskov, *Phys. Rev. Lett.* **76**, 2141 (1996).
- [50] M. Mavrikakis, B. Hammer, and J. K. Nørskov, *Phys. Rev. Lett.* **81**, 2819 (1998).
- [51] K. Stokbro and S. Baroni, *Surf. Sci.* **370**, 166 (1997).
- [52] F. Besenbacher and J. K. Nørskov, *Prog. in Surf. Sci.* **44**, 5 (1993).
- [53] K. Kern, H. Niehus, A. Schatz, P. Zeppenfeld, J. Goerge, and G. Comsa, *Phys. Rev. Lett.* **67**, 855 (1991).
- [54] K. Pohl, M. C. Bartelt, J. de la Figuera, N. C. Bartelt, J. Hrbek, and R. Q. Hwang, *Nature* **397**, 238 (1999).
- [55] H. Brune, M. Giovannini, K. Bromann, and K. Kern, *Nature* **394**, 451 (1998).

- [56] T. M. Parker, L. K. Wilson, N. G. Condon, and F. M. Leibsle, *Phys. Rev. B* **56**, 6458 (1997).
- [57] D. D. Chambliss, R. J. Wilson, and S. Chiang, *Phys. Rev. Lett.* **66**, 1721 (1991).
- [58] P. W. Murray, I. M. Brookes, S. A. Haycock, and G. Thornton, *Phys. Rev. Lett.* **80**, 988 (1998).
- [59] M. Seul and D. Andelman, *Science* **267**, 476 (1995).
- [60] J. V. Barth, H. Brune, G. Ertl, and R. J. Behm, *Phys. Rev. B* **42**, 9307 (1990).
- [61] S. Narasimhan and D. Vanderbilt, *Phys. Rev. Lett.* **69**, 1564 (1992).
- [62] V. I. Marchenko, *JEPT lett.* **33**, 381 (1981).
- [63] D. Vanderbilt, *Surf. Sci.* **268**, L300 (1992).
- [64] O. L. Alerhand, D. Vanderbilt, R. D. Meade, and J. D. Joannopoulos, *Phys. Rev. Lett.* **61**, 1973 (1988).
- [65] D. Vanderbilt, in *Computations for the Nano-Scale*, edited by P. E. Blöchl, A. J. Fisher, and C. Joachim (Kluwer Academic Publishers, Netherlands, 1993).
- [66] P. Zeppenfeld, M. Krzyzowski, C. Romainczyk, G. Comsa, and M. G. Lagally, *Phys. Rev. Lett.* **72**, 2737 (1991).
- [67] F. Jensen, F. Besenbacher, E. Lægsgaard, and I. Stensgaard, *Phys. Rev. B* **41**, 10233 (1990).
- [68] D. J. Coulman, J. Wintterlin, R. J. Behm, and G. Ertl, *Phys. Rev. Lett.* **64**, 1761 (1990).
- [69] V. I. Marchenko, *JEPT lett.* **55**, 73 (1992).
- [70] K. Pohl, J. de la Figuera, M. C. Bartelt, N. C. Bartelt, J. Hrbek, and R. Q. Hwang, *Surf. Sci.* **433**, 506 (1999).
- [71] S. Völkening, K. Bedürftig, K. Jacobi, J. Wintterlin, and G. Ertl, *Phys. Rev. Lett.* **83**, 2672 (1999).
- [72] J. Fusy and R. Ducros, *Surf. Sci.* **237**, 53 (1990).

- [73] J. Wintterlin, S. Völkening, T. W. Janssens, T. Zambelli, and G. Ertl, *Science* **278**, 1931 (1997).
- [74] W. W. Crew and R. J. Madix, *Surf. Sci.* **319**, L34 (1994).
- [75] R. A. Bennett, S. Poulston, and M. Bowker, *J. Chem. Phys.* **108**, 6916 (1998).
- [76] P. T. Sprunger, Y. Okawa, F. Besenbacher, I. Stensgaard, and K. Tanaka, *Surf. Sci.* **344**, 98 (1995).
- [77] I. Stensgaard, E. Lægsgaard, and F. Besenbacher, *J. Chem. Phys.* **103**, 9825 (1995).
- [78] Y. Matsumoto and K. Tanaka, *Jpn. J. Appl. Phys.* **37**, L154 (1998).
- [79] D. Eigler and E. K. Schweizer, *Nature* **344**, 524 (1990).
- [80] L. Bartelts, G. Meyer, and K.-H. Rieder, *Phys. Rev. Lett.* **79**, 697 (1997).
- [81] K. Bromann, C. Félix, H. Brune, W. Harbich, R. Monot, J. Buttet, and K. Kern, *Science* **274**, 956 (1996).
- [82] J. W. Niemantsverdriet, A. F. P. Engelen, A. M. de Jong, W. Wieldraaijer, and G. J. Kramer, *Appl. Surf. Sci.* **144**, 366 (1999).
- [83] J. P. Wilcoxon, P. P. Newcomer, and G. A. Samara, *J. Appl. Phys.* **81**, 7934 (1997).
- [84] K. Wong, S. Johansson, and B. Kasemo, *Faraday Discuss.* **105**, 237 (1996).
- [85] J. C. Hultten and R. P. V. Duyne, *J. Vac. Sci. Technol. A* **13**, 1553 (1995).
- [86] P. W. Jacobs, F. H. Ribeiro, G. A. Somorjai, and S. J. Wind, *Catalysis Letters* **37**, 131 (1996).

Chapter 4

Adsorbate-enhanced self-diffusion on Pt(110)–(1×2)

Surface diffusion is a key elementary process in heterogenous catalysis, thin film growth, and other material processes. In catalysts surface diffusion is of importance for the activity, since adsorbed atoms or molecules first have to reach a reaction partner before a chemical reaction can take place. Recently, scanning tunneling microscopy (STM) has clearly demonstrated its power to reveal dynamic phenomena such as diffusion and reaction of adsorbates on flat metal surfaces, e.g. [1–7]. In particular, quantitative microscopic information on diffusion processes can be obtained by directly tracking the positions of the individual adsorbates during their migration on the surface.

Surface diffusion is also important for the thermal stability of typical solid catalyst materials. Under reaction conditions, high operation temperatures or long term use can result in sintering or reshaping of the highly dispersed catalyst particles. Hereby active surface area is lost with serious consequences for the catalyst activity as well as the selectivity. In general, sintering processes exhibit a strong dependency on the gas environment [8]. Although numerous studies have been performed, the fundamental understanding of this phenomenon is still fairly limited, e.g. [9–12].

In order to shed some light on the microscopic understanding of the gas-assisted sintering, the present chapter will address the question of how

adsorbates modify surface diffusion of metal atoms. Mechanistic insight into this effect is derived from dynamical observations, using the STM, of hydrogen-promoted self-diffusion on the Pt(110)-(1×2) surface. The results are presented in [IV] and [V]. The influence of coadsorbed oxygen will also be described.

4.1 Self-diffusion on Pt(110)-(1×2)

The diffusion of individual Pt adatoms on the Pt(110)-(1×2) surface has been thoroughly investigated by T. R. Linderoth and S. Hørch from the group [13] and serves therefore as an ideal reference system for studying the influence of coadsorbed hydrogen. In this previous study, detailed insight into the diffusion process was obtained by acquiring and analyzing STM movies of migrating Pt adatoms (section 2.3.3). Platinum adatoms, deposited onto the surface, are situated in the missing-row troughs (figure 4.1), and STM movies¹ directly reveal that the diffusion of these adatoms proceeds one-dimensionally back and forth along the troughs.

In general, a single migrating adatom experiences a corrugated potential energy surface representing the adatom-surface interaction. The energy surface can have the same translational symmetry as the physical substrate, and an adatom will reside at a position of minimal potential energy. The adsorption sites are separated by energy barriers, and since such barriers are typically much smaller than the adsorption energy, thermally activated migration becomes possible. Occasionally, thermal fluctuations of the lattice excite the Pt adatom into a transition state. Once promoted into this state, the adatom can jump to the neighbouring adsorption site, where energy dissipation to the phonon-sea de-excites the adatom again. The adatom is then retrapped into an adjacent adsorption well. When the diffusion energy barrier is large compared to the thermal energy, the time spent making such a transition is much smaller than the period in which the adatom resides in the adsorption site interacting with the lattice. The adatom therefore loses all memory of where it came from and will, subsequently, be displaced back or forth with the same probability [14].

The rate, h , for a thermally activated jump process can usually be described by an Arrhenius expression

$$h = \nu \exp(-E_d/k_bT), \quad (4.1)$$

¹Examples can be found at <http://www.ifa.au.dk/camp/stmoldpub.htm>

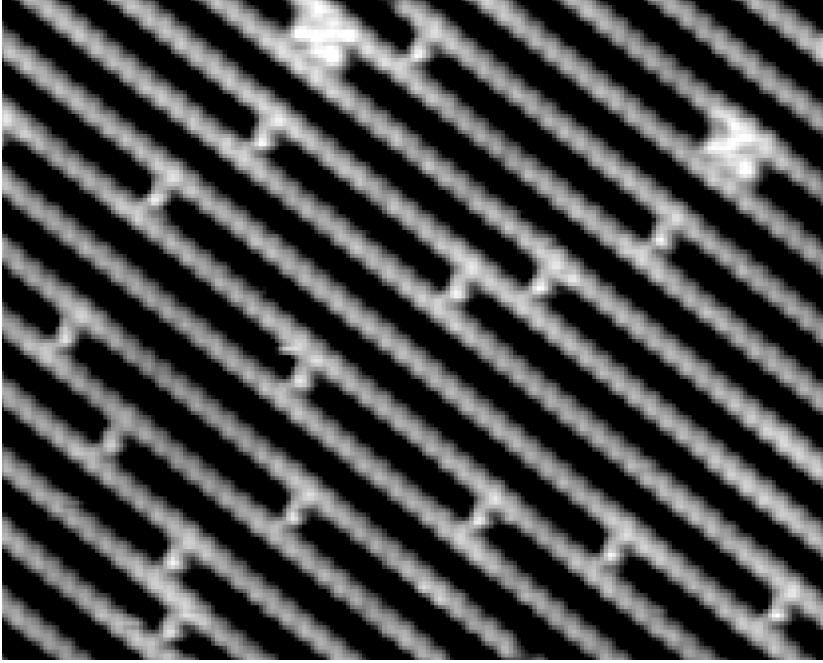


Figure 4.1: An atom-resolved STM image of the Pt(110)-(1×2) surface showing a submonolayer of Pt adatoms adsorbed in five-fold hollow sites in the troughs.

in which the activation barrier E_d is the highest energy point on the potential energy surface, relative to the initial state, along the minimum energy path connecting the initial and final state. k_b is Boltzmanns constant, and T is the substrate temperature. The transition state theory states that the prefactor ν is independent of temperature and related to curvatures on the potential energy surface in the adsorption well and at the transition state within a harmonic approximation to the potential energy surface at these positions [15]. Typically, $\nu \sim 10^{12}\text{s}^{-1}$ [16]. During a one-dimensional random migration, the uncorrelated jumps between nearest-neighbour sites will lead to a zero mean displacement of the adatom ($\langle l \rangle = 0$). The second moment of the displacement distribution will, however, reflect the excursion of the adatom. $\langle l^2 \rangle$ is related to h by $\langle l^2 \rangle = hta^2$, where $l = 0$ at time $t = 0$ and a is the distance between nearest-neighbour sites [15].

To extract quantitative information from the STM movies concerning

the diffusion of the Pt adatoms, it is important to realize that the observed displacements of the adatoms between consecutive images are not simply equated with the actual number of adatom jumps. An adatom can jump several times between successive images, which will be observed as either a displacement over several lattice spacings or, if the adatoms has jumped back and forth, as no displacement at all. In the diffusion process an adatom can perform single jumps to the nearest-neighbour (nn) site, but it may also execute long jumps, characterized as jumps taking the adatom to sites beyond the nn site before retrapping (in contrast to a series of sequential single jumps) [16].

The appropriate statistical analysis taking these considerations into account is worked out by Ehrlich and co-workers [17, 18]. The central element in this analysis is the displacement distribution, $P_l(t)$, of an adatom, i.e. the probability of an adatom being displaced by the distance l in the time interval t . By tracking the position of each Pt adatom in successive images in STM movies, the displacement distribution is readily obtained and quantitative information concerning the diffusion processes can be extracted. In this way, Linderoth *et al.* [13] determined the jump rate for single jumps taking the adatom from a fivefold hollow site to the neighbouring one. By acquiring and analyzing STM movies at substrate temperatures ranging from 300 K to 380 K, an Arrhenius dependence of the hopping-rate on the substrate temperature was revealed and characterized by a prefactor $\nu = 10^{10.7 \pm 0.2} \text{s}^{-1}$ and an activation barrier $E_d = 0.81 \pm 0.01 \text{ eV}$. The detailed displacement distribution analysis also revealed the occurrence of double jumps with an Arrhenius behaviour. The ratio of double to single jumps has a low value of only $h_2/h_1 \sim 5 - 10 \%$.

How one should envision the jump processes? The Pt adatoms are only depicted in the fivefold hollow sites in the troughs, whereas the actual trajectory followed by an adatom is not resolved in the STM movies. Quite surprisingly, results from atom-resolved STM movies reported in [X] reveal that longer Pt clusters situated in the troughs on Pt(110)-(1×2) can migrate by spontaneously promoting an end atom to the cluster top, where the Pt atom migrates to the opposite end of the cluster and drops back into the trough. From the STM movies, the activation energy barriers for an atom to ascend and descend the cluster edges are estimated to be 0.91 eV and 0.70 eV, respectively. These observations strongly suggest that the path followed by a Pt adatom on Pt(110)-(1×2) involves the (111) micro facets of the missing-row troughs.

These findings have already stimulated a number of theoretical studies. Two different diffusion channels are actually considered as the most

probable for an adatom: (1) A direct path along the trough from the fivefold hollow site through a bridge site to the neighbouring fivefold hollow site, and (2) an indirect path involving the close-packed (111) facets of the troughs. Both paths are illustrated in figure 4.2.

Using molecular dynamics simulations, Montalenti and Ferrando [19] have shown that the facet path contributes considerably to the diffusivity of Au adatoms on the reconstructed Au(110)-(1×2) surface, a system similar to the present Pt/Pt(110)-(1×2). Inspired by their results, Lorensen *et al.* have recently studied the self-diffusion on the Pt(110)-(1×2) surface and have mapped out the potential energy surface for trajectories along the trough and the facet using density functional theory (DFT) calculations [20]. The results are depicted in figure 4.2. The energy barrier for both the direct and indirect path is 0.94 eV, indicating that both paths are equally probable. In a similar study, using a slightly different calculational setup, Feibelman obtains the same barrier height for the indirect path but finds a larger barrier of 1.03 eV for the direct path, suggesting that the facet path is dominating [21]. With the present state of *ab initio* DFT calculations, the absolute accuracy of these barriers is ~ 0.1 eV, whereas the relative accuracy is expected to be much better. The discrepancy between the experimental and theoretical barriers seems therefore reasonable, indicating that both the trough and facet path are important for the diffusion of Pt adatoms. On the theoretical side, there is still some controversy left regarding the dominance of the facet path.

The facet path provides a likely explanation of the small fraction of double jumps found in the previous STM study [20]. Once an adatom is promoted to the facet, the subsequent displacements along the facet are to be viewed as instantaneous due to the small barriers. A single jump is executed if the adatom jumps back into the trough at the first hcp site it encounters, and a double jump only occurs only if the adatom reaches the second hcp site from where it returns to the trough.

4.2 H-enhanced self-diffusion on Pt(110)

Up to now there has only been few investigations of how surface diffusion is modified by the presence of foreign adsorbates. Hydrogen coadsorption has attained more attention due to hydrogen's potential of being an easily (thermally) removable surfactant in thin film growth. The current literature is rather conflicting in the sense that, experimentally, hydrogen coadsorption has been reported to promote and also inhibit the diffusion

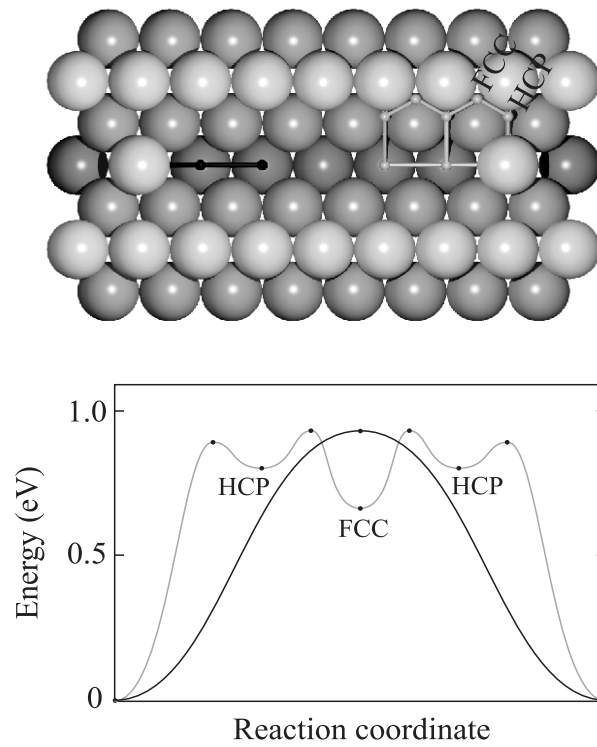


Figure 4.2: The ball model illustrates the trough path (black line) and the facet path (grey line) followed by a Pt adatom. The potential energy diagram along the two paths is obtained from DFT calculations by H.T. Lorensen [20]. The black (grey) curve corresponds to the direct (indirect) path.

of metal adatoms on surfaces [22, 23]. Theoretical *ab initio* calculations for H on Be(0001) have shown that the diffusivity of a Be adatom is increased by the formation of a Be-H addimer [24]. From a mechanistic point of view the enhanced diffusivity is in this case described as a simple 'skyhook' effect, where the hydrated Be adatom has a weaker bond to the surface, resulting in an outwards relaxation from the surface to a position where the addimer experiences a less corrugated potential energy surface.

Despite these efforts, the general atomistic understanding of gas-assisted surface diffusion is still quite sparse. In the following, the mechanistic insight is derived from experimental observations of hydrogen-promoted self-diffusion on the Pt(110)-(1×2) surface.

4.2.1 Experimental details

The experiments are performed in a standard ultrahigh vacuum system as described in section 3.1. A submonolayer of Pt is deposited onto an initially clean Pt(110)-(1×2) surface. This is done by resistively heating a thoroughly degassed 0.4 mm diameter 99.995% clean Pt wire in front of the sample. Following the Pt deposition, the sample is transferred to the STM for image acquisition.

A detailed insight into the migration of the Pt adatoms is obtained by acquiring STM movies (as described in section 2.3.3). The acquisition time for the individual STM images is adjusted to the mobility of the diffusing Pt adatoms and ranges from 1 s to 20 s. Typically, an STM movie consists of up to several thousand images, each containing 10 to 30 Pt adatoms. All STM images in a film are obtained in the constant current mode with tunnel resistances higher than 100 MΩ. Above this limit, the influence of the tip is found to be negligible on the self-diffusion on the clean surface [13]. To avoid any interaction between the Pt adatoms, very low coverages (~ 0.01 ML) of Pt adatoms are used in the experiments. The influence of coadsorbed gasses on the Pt self-diffusion is revealed by admitting gas (hydrogen) to the UHV chamber during acquisition of an STM movie.

In the data analysis, the positions of the individual Pt adatoms in a movie are tracked in time (section 2.3.3). Recent studies show that there is a weak attractive interaction between next-nearest-neighbour Pt adatoms situated in the same trough ([XI] and [21]). Since the adatom pair-interaction strength generally decreases with increasing adatom-adatom separation, Pt adatoms are expected not to interact if they are separated by more than three lattice spacings. The interaction between Pt adatoms

located in adjacent troughs is considered to be negligible [25]. Thus, in order to exclude any interaction between the diffusing adatoms, only those adatoms spaced by $4 \times a_{[1\bar{1}0]}$ or more in the same trough are included in the analysis.

As will be demonstrated, hydrogen increases the mean-square displacement of the Pt adatoms by orders of magnitude. Consequently, the displacement distribution approaches a gaussian form, in which the detailed information about the jump processes is smeared out and it becomes difficult to unravel the contribution from the different jump processes [17, 18]. However, the single jumps are much more frequent than the double jumps, and we will therefore neglect the double jump events in the following. When only single jumps participate in the diffusion process, the mean-square displacement is related to the hopping-rate, according to the discussion in section 4.1. The mean-square displacement ($\langle l^2 \rangle$) from image to image during a movie is calculated from the tables of the tracked adatom positions. The diffusivity of a Pt adatom is quantified in terms of $\langle x^2 \rangle = \langle l^2 \rangle / (a_{[1\bar{1}0]}^2 t_{ac})$, where t_{ac} is the image acquisition time and $a_{[1\bar{1}0]} = 2.78 \text{ \AA}$ is the nearest-neighbour distance in the $[1\bar{1}0]$ direction. $\langle x^2 \rangle$ is plotted versus time in the STM movie and provides quantitative information about the influence of the gas adsorbates on the Pt diffusivity in the period after the gas admission.

4.2.2 Experimental results

When hydrogen is admitted to the UHV chamber an enhanced self-diffusion is directly observed in the STM movies. The main new finding is the formation of intermediate Pt-H complexes, which have a significantly larger diffusivity than the other Pt adatoms. These Pt-H complexes show up in the STM movies as brighter Pt adatoms. After some images, a bright adatom turns normal again. Such events are presented in the STM images in figure 4.3, which are taken from an STM movie recorded at 303 K and at a hydrogen pressure of 7×10^{-7} mbar. In the first image all Pt adatoms look normal. In the following four images, one single adatom suddenly appears much brighter and moves several lattice spacings from image to image. In the same period, only one of the other Pt adatoms performs a hop to a neighbouring lattice site. The apparent height of a bright Pt adatom is increased by $\approx 0.4 \text{ \AA}$ compared to a normal adatom, as shown in figure 4.4.

Temperature-programmed desorption (TPD) studies have shown that hydrogen adsorbs dissociatively on the Pt(110)-(1 \times 2) surface and desorbs

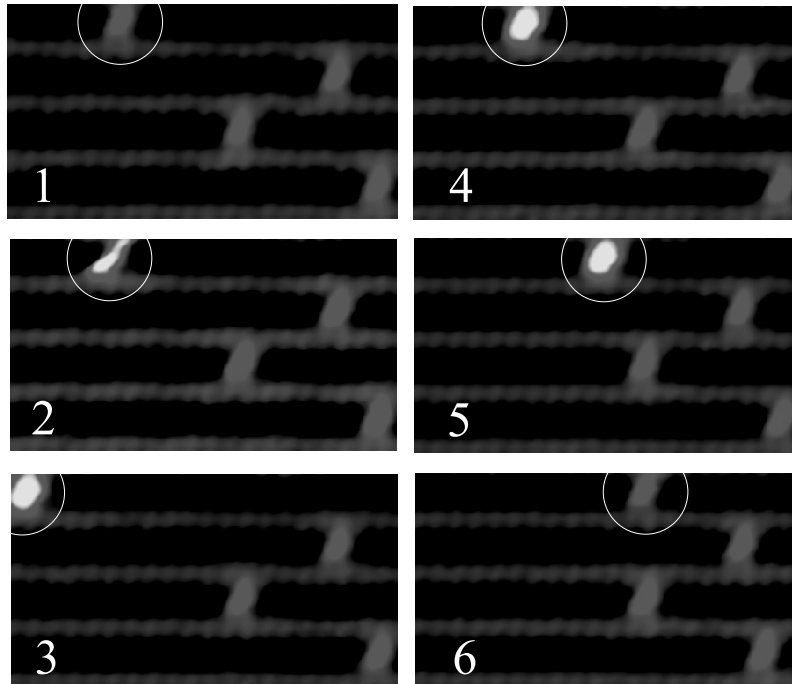


Figure 4.3: Six consecutive STM images ($56 \text{ \AA} \times 31 \text{ \AA}$) extracted from a typical STM movie showing the development of a normal Pt adatom to a bright Pt-H intermediate complex and back to a normal Pt adatom again. The Pt adatom of interest is marked by a white circle.

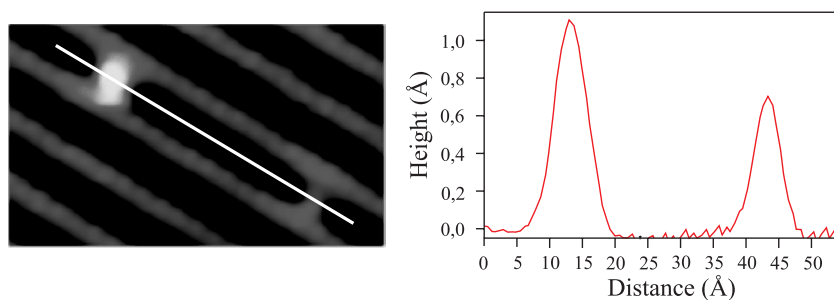


Figure 4.4: A linescan along a $[1\bar{1}0]$ trough containing a bright Pt-H complex and a normal Pt adatom.

around room temperature [26, 27]. In the experiments the hydrogen coverage is thus determined by an equilibrium between adsorption and desorption. Using the sticking coefficient and the desorption parameters in [26], the hydrogen coverage at a sample temperature of 303 K and at a hydrogen background pressure of 7×10^{-7} mbar is estimated to ≈ 0.5 H atoms per (1×2) unit cell. The hydrogen atoms chemisorbed on the surface are not observed in the STM images due to their high diffusivity. For a given hydrogen coverage, the diffusivity of the Pt adatoms is found to be constant in time.

As shown in Fig. 4.5, the Pt adatoms on the clean (1×2) surface at 303 K have a mean-square displacement of about 0.002 (nearest-neighbour spacings) 2 per second. This is consistent with the previous findings of a Pt self-diffusion activation barrier of 0.81 eV. For this and the following comparison, $\langle x^2 \rangle$ is assumed to exhibit an Arrhenius dependence on the temperature, and the prefactor for single jumps, $10^{10.7} \text{s}^{-1}$, is used. At these low pressures (background pressure of $\sim 7 \times 10^{-11}$ mbar) no bright Pt adatoms are observed. Increasing the hydrogen pressure to 4×10^{-8} mbar and further to 7×10^{-7} mbar, all Pt adatoms are found to diffuse faster, and bright adatoms appear. In the highest hydrogen pressure interval, the observed $\langle x^2 \rangle$ for the bright adatoms is in average ≈ 500 times larger than without hydrogen, corresponding to a reduction of the diffusion barrier by 0.16 ± 0.02 eV. This decrease depends only slightly on pressure as observed by comparison of the two pressure intervals.

The lifetime of the Pt-H complexes can be fairly long, as indicated by figure 4.3. To quantify the mean lifetime, the number of complexes observed to survive a time t , $N(t)$, is shown in figure 4.6. The discrete

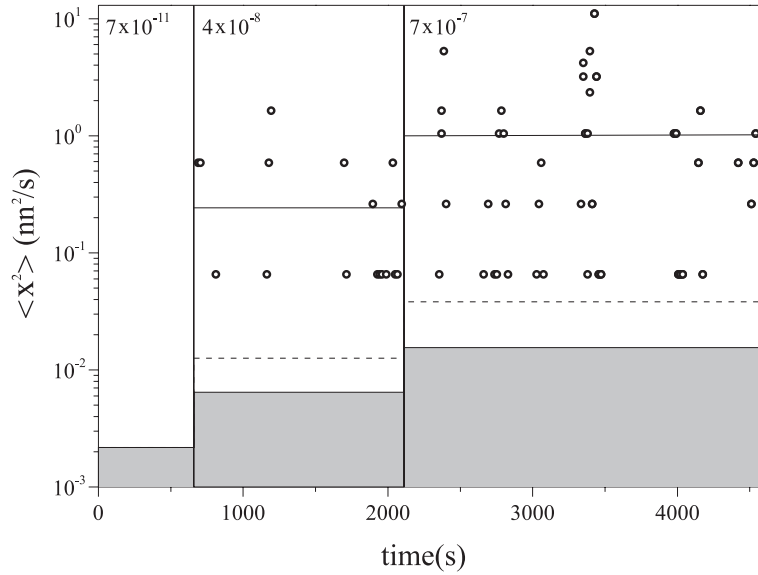


Figure 4.5: Mean-square displacements per second, $\langle x^2 \rangle$, during an STM movie for different hydrogen background pressures. At the times indicated by the vertical lines, the H_2 background pressure is increased in the film to 4×10^{-8} mbar and 7×10^{-7} mbar, respectively. The open circles in the top part show the $\langle x^2 \rangle$ for image to image displacements of individual Pt-H complexes. The full lines show the average of $\langle x^2 \rangle$ for the bright Pt-H complexes. The grey bars show the average $\langle x^2 \rangle$ of the other Pt adatoms. The dashed lines show the average $\langle x^2 \rangle$ of all Pt adatoms. The film is taken at 303 K and with 15 s per image. $\langle x^2 \rangle$ is given in units of nm^2/s , where nm is the nearest-neighbour distance in the $[1\bar{1}0]$ direction.

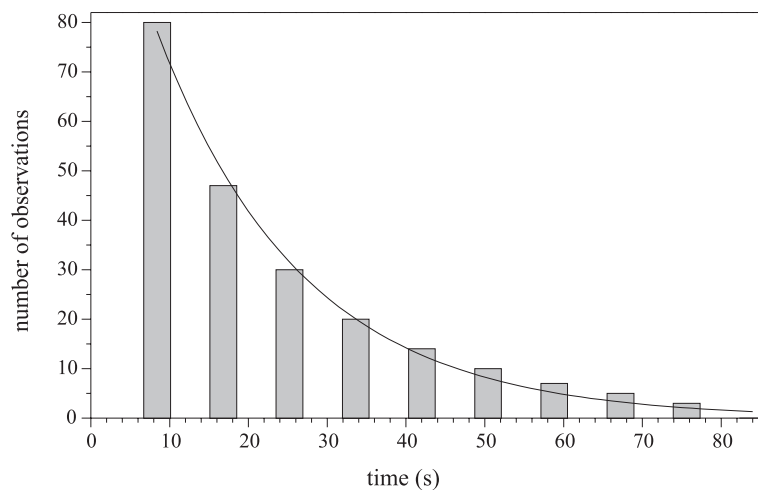


Figure 4.6: The lifetime distribution for Pt-H complexes observed in an STM movie showing the number of complexes which have survived a time t . The curve represents an exponential fit of $N = N_{ac} \exp(-(t - t_{ac})/\tau)$ to the distribution. τ is the mean lifetime. In the movie, the image acquisition time is $t_{ac} = 8.4$ s, $N_{ac} = 78$, the substrate temperature is $T = 304$ K, and $P_{H_2} = 2 \times 10^{-7}$ mbar. The lifetime is found to be independent of the hydrogen pressure.

distribution is due to the finite image acquisition time (t_{ac}). The lifetime of a complex observed in one image is t_{ac} , in two images $2t_{ac}$, and so forth. The lifetime distribution $N(t)$ is found to decay exponentially, and by fitting $N(t) = N_{ac} \exp(-(t - t_{ac})/\tau)$ to the distribution, the mean lifetime is determined to $\tau \approx 18$ s. The long mean lifetime reveals a large barrier for the decay of the Pt-H complex. An energy barrier for this process can be estimated to ≈ 0.8 eV by assuming an Arrhenius dependence for the decay rate $1/\tau = \nu \exp(-E_{diss}/k_B T)$. The temperature is $T = 304$ K and the prefactor $\nu = 10^{10.7} \text{ s}^{-1}$ is used.

The exponentially distributed lifetime of the Pt-H complexes also implies that complexes living shorter than the image acquisition time may have been formed. That is, bright adatoms may have been formed, displaced and turned normal again in the period between two encounters with the tip and are thus not registered as bright adatoms. Such short-living complexes are likely responsible for the slightly increased diffusivity of the “apparent” normal adatoms (the grey bars in figure 4.5).

4.2.3 Discussion

The giant mobility and the striking difference in height strongly suggest, as already discussed, that the bright adatoms are temporarily formed Pt-H complexes. In this section, the experimental findings will be discussed in the light of *ab initio* density functional theory calculations performed by H. T. Lorensen [28].

Molecular hydrogen adsorbs dissociatively on the Pt(110)-(1×2) surface [26]. In order to find the optimum adsorption site for a hydrogen atom, the adsorption energy has been calculated for a number of different high symmetry adsorption sites on the Pt(110)-(1×2) surface. The results are shown in figure 4.7. The preferred adsorption site for a H atom appears to be on-top of the adatom (model 10), whereas the bridge site on the ridge (model 4) has almost the same stability. Thus, these calculations show that a hydrogen atom can be trapped on-top a Pt adatom residing in the trough.

The modified appearance in STM of a Pt adatom having a H atom adsorbed on-top can be estimated by calculating the local density of states (LDOS) at the Fermi level, according to Tersoff and Hamann [29]. The electronic structure is available from the DFT calculations. It appears that the formation of a Pt-H complex with H sitting in the on-top site induces an increase in the LDOS as compared to the LDOS for a clean Pt adatom of $\approx 0.3 \text{ \AA}$, which is very similar to the “brightness” of the Pt-H complexes

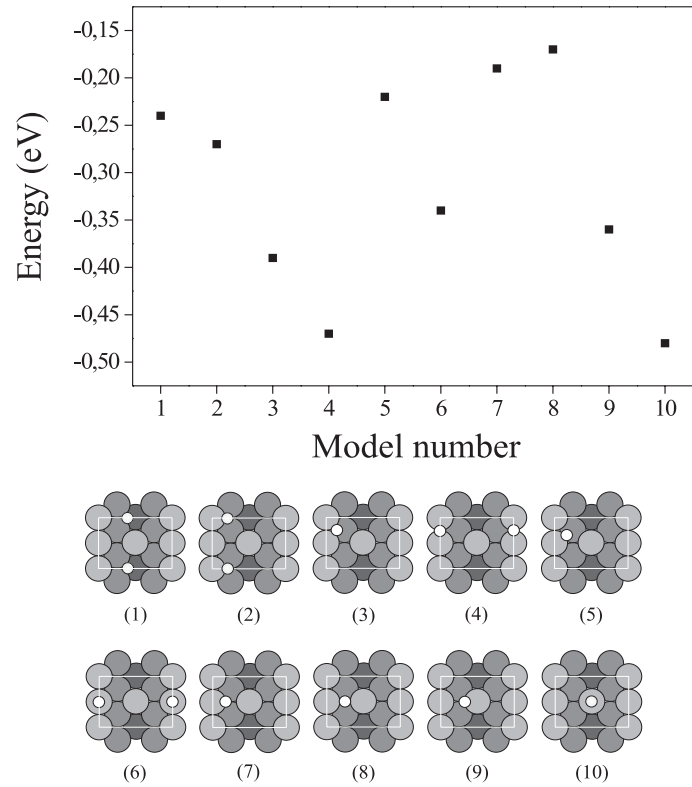


Figure 4.7: Energy diagram showing the adsorption energy of a hydrogen atom (relative to half the binding energy in H_2 in the gas phase) in various adsorption sites as illustrated by the ball models. Hydrogen atoms are indicated by the white balls, whereas grey-colored balls indicate platinum. A Pt adatom is coadsorbed in the trough. In the calculations a (2×2) unit cell is employed (depicted by the white square), and the H coverage is $1/2$ ML. Further calculational details are given in [28].

observed experimentally. Based on these theoretical results, the bright Pt adatoms are interpreted as Pt-H addimers consisting of Pt adatoms with top-bound H atoms.

Having established a structural model for the bright Pt adatoms, it is interesting to see how the potential energy surface for a Pt-H complex is changed compared to a Pt adatom along the two diffusion paths on the Pt(110)-(1×2) surface. Results from the DFT calculations are shown in figure 4.8. It appears that the two paths are affected differently: The indirect path along the facet has an *increased* barrier, while the barrier along the direct path is *lowered* by 0.09 eV, in reasonable agreement with the value found experimentally. The reduction in the diffusion barrier only occurs if the on-top H atom is allowed to relax, i.e. to slide down the side of the Pt adatom during the diffusion event. The resulting diffusion can thus be described as a “wagging” motion and is not associated a “skyhook” effect.

In conclusion, hydrogen coadsorption promotes the diffusivity of Pt adatoms on Pt(110)-(1×2) by the formation of Pt-H addimers whereby the barrier for the direct diffusion path is reduced significantly. The reason why hydrogen changes the diffusion barrier along the two diffusion paths differently is not revealed. Perhaps a detailed study of the electronic structure near the complex in the transition states for the two paths will provide an answer.

A remaining question is why only approximately 1% of the Pt adatoms are observed to be in the bright state. The adsorption site on-top of the adatom is by 0.01 eV marginally more stable than the bridge site on the ridge. Also, the energy barrier of 0.8 eV associated with the decay of the bright adatoms has not yet been discussed. It is not simply the barrier for hydrogen to move off the adatom which has a significantly smaller value of 0.31 eV, according to DFT calculations. It is suggested that both these findings are related to trace amounts of CO competing with the H atoms for the Pt adatom sites.

Carbon monoxide adsorbs molecularly on Pt(110)-(1×2) around room temperature and desorbs above ~ 450 K [30]. When the CO coverage exceeds a critical value of ~ 0.4 ML, a surface reconstruction initiates in which 4-6 atom wide (1×1) patches are formed by displacing ridge-Pt atoms into the troughs [31, 32]. Carbon monoxide binds to on-top sites on the ridges of the clean surface, as revealed by reflection absorption infrared spectroscopy [33], and is indeed expected to adsorb preferentially on Pt adatoms, since such sites have low coordination, thus high lying *d*-bands which give rise to stronger bonds, according to the *d*-band model

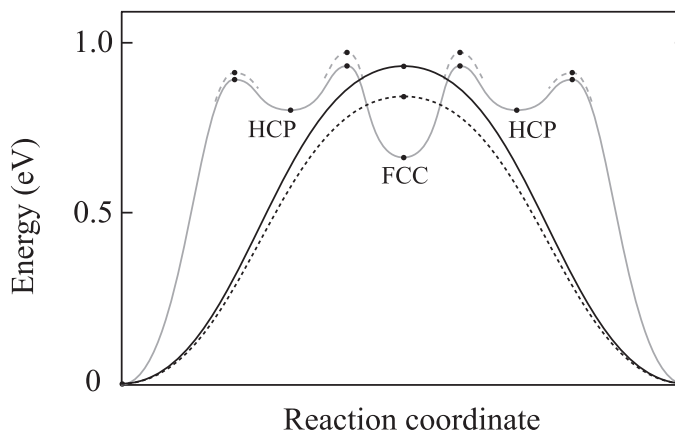


Figure 4.8: The calculated potential energy surface along the two different diffusion paths shown in figure 4.2. The black (grey) curves indicate the direct (indirect) path. The diffusion paths on the clean Pt surface are shown by the full-drawn curves. The dashed curves show the effect of forming a Pt-H complex.

by Hammer and Nørskov [34, 35].

The finite lifetime of the bright Pt-H complexes is tentatively attributed to the process where a CO molecule moves from the Pt ridge, through a site on the (111) micro-facet, to the low-coordinated Pt adatom site and replaces the H atom. DFT calculations show that (i) CO strongly prefers these adatom sites and that (ii) the larger barrier for the replacement process is due to the motion of a CO molecule from its on-top site on a ridge-Pt atom to the adatom in the trough, while the energy barrier for the H motion is much smaller. The barrier for CO to diffuse from the ridge to the adatom is estimated from the DFT calculations to ~ 0.7 eV, in reasonable agreement with the experimental value.

The low probability of observing a Pt-H complex is in this picture ascribed the larger preference of CO to occupy low-coordinated Pt adatoms compared with H. The equilibrium



is therefore heavily shifted towards the right. Defining the energy difference

$$\Delta E = E(CO_{adatom}) + E(H_{ridge}) - E(CO_{ridge}) - E(H_{adatom}) \quad (4.3)$$

the H coverage on the adatom is given roughly by

$$\frac{\theta_{H_{adatom}}}{\theta_{CO_{adatom}}} = \frac{\theta_{H_{ridge}}}{\theta_{CO_{ridge}}} e^{\Delta E/kT} \quad (4.4)$$

From the DFT calculations it is found that the CO gains $E(CO_{adatom}) - E(CO_{ridge}) = -0.36$ eV by the moving to the adatom site, whereas H is only marginally stabilized by $E(H_{adatom}) - E(H_{ridge}) = -0.01$ eV. The energy difference becomes $\Delta E = -0.35$ eV. Thus, around room temperature the concentration of Pt-H complexes ($\theta_{H_{adatom}}$) will only dominate if $\theta_{H_{ridge}}/\theta_{CO_{ridge}} \gg 10^6$.

Experimentally, a such low concentration of additional impurities is extremely hard to obtain. In the experiments hydrogen is coadsorbed from a constant background atmosphere at pressures of $10^{-7} - 10^{-6}$ mbar. Due to exchange and reaction with the chamber walls, the background concentration of water and carbon monoxide increases when hydrogen is admitted to the vacuum chamber. Water is not considered as a problem, since desorption from the Pt(110)-(1×2) surface is complete at substrate temperatures above 200 K under UHV conditions [36]. The carbon monoxide partial pressure in the hydrogen background atmosphere is typically three orders of magnitude lower than the hydrogen pressure and lies in the range $10^{-10} - 10^{-9}$ mbar. It can therefore not be excluded that CO constitutes a problem in the experiments.

In order to test experimentally whether co-adsorbed CO has any influence at all on the formation of bright adatoms and the hydrogen promotion, the diffusion of Pt adatoms is monitored in a background of hydrogen with small amounts of CO added deliberately. Figure 4.9 shows the Pt adatom diffusivity as a function of time in a such gas mixture. At the time noted A, CO is admitted to a total chamber pressure of 5×10^{-10} mbar, and at time B, after an CO exposure of 0.16 L, hydrogen is introduced to a total pressure of 2×10^{-7} mbar. Immediately after the gas admission (B), a promotion of the diffusivity is observed. However, the presence of CO results in a diminished effect of the hydrogen: only very few bright adatoms are observed and the diffusivity averaged over *all* Pt adatoms is only increased by a factor of ~ 3 . This should be compared to the 500-fold increase when only hydrogen is present, figure 4.5 (notice that the scale is logarithmic in fig. 4.5 and linear in fig. 4.9). As the CO exposure increases, the enhanced diffusivity of the Pt adatoms is gradually reduced and reaches a value below that of the clean surface. No bright adatoms are observed at this stage. At point C, the lifting of the (1 × 2) reconstruction starts.

For a comparison, experiments with coadsorption of only CO show,

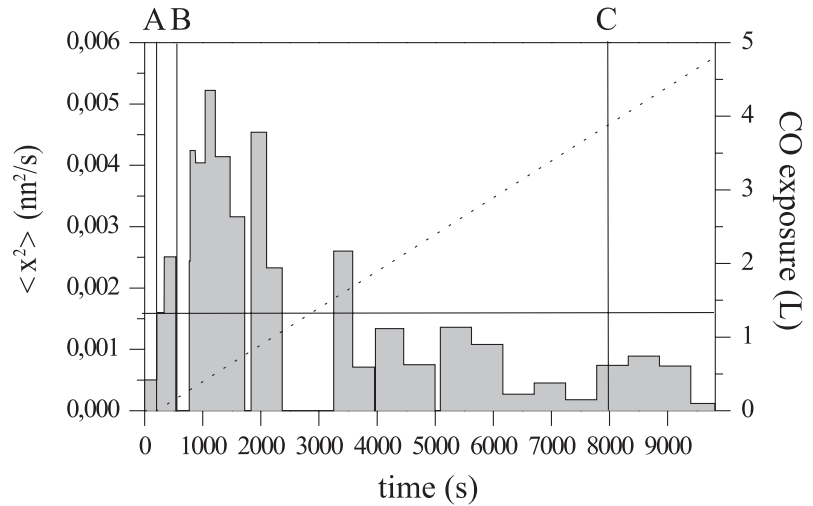


Figure 4.9: Mean-square displacement per second versus time for a Pt adatom with a background consisting of CO and H₂. The solid vertical line indicates the hopping-rate of a Pt adatom on the clean surface as a reference. The grey bars show the average of $\langle x^2 \rangle$ over *all* Pt adatoms in the corresponding time interval. At time A, CO is admitted to the vacuum chamber to a pressure of 5×10^{-10} mbar. At time B, hydrogen is admitted up to a total pressure of 2×10^{-7} mbar. The CO preexposure at time B is 0.16 L. The additional CO exposure during the movie is indicated with the dotted line. Notice that there might be a shadow effect due to the tip. At time C, the lifting of the (1×2) reconstruction begins. In the time intervals where the mean-square displacement is zero, the resolution is temporarily lost. The substrate temperature is 303 K and the image acquisition time is 5.5 s. $\langle x^2 \rangle$ is given in units of nm²/s, where nm is the nearest-neighbour distance in the $[1\bar{1}0]$ direction.

similarly to the late stage of the period BC in figure 4.9, a slight decrease in the diffusivity. The corresponding increase in the diffusion barrier is ~ 8 meV, which is within the uncertainty on the barrier determination. No bright adatoms are observed in the case of CO adsorption. The adsorbed CO molecules are invisible in the STM. The reason for this is the low diffusion barrier on the ridges (~ 0.15 eV [37]), and for CO trapped to the adatom, the CO molecule is probably quite flexible, so it relaxes away when the adatom encounters the tip.

Thus, these results show that coadsorption of CO during hydrogen exposure indeed suppresses the formation of bright adatoms and thereby indicates that CO impurities are likely to be the cause for the low fraction and finite lifetime of the bright Pt-H complexes. The facts that CO binds more strongly to the low-coordinated Pt adatoms and that low concentrations of Pt adatoms are considered in the experiments imply that the experiments are sensitive to even small amounts of CO impurities [38].

4.3 O-enhanced self-diffusion on Pt(110)

Oxygen has been shown to influence the size and the shape of Pt particles dispersed on oxidic supports under certain circumstances [9, 10, 39]. It has been speculated that oxygen induces these structural transformations by weakening the Pt-Pt bonds and by increasing the mobility of Pt, probably due to the formation of PtO_x complexes.

In the summary of chapter 3, it was shown that the oxygen-induced nanostructure on Pt(110)-(1 \times 2) can be used to control the growth of Pt islands, indicating that oxygen modifies the surface self-diffusion. In order to elucidate this influence directly, experiments with oxygen coadsorption are carried out, similarly to those for hydrogen described in the previous section. The mean-square diffusivity, $\langle x^2 \rangle$, is obtained as a function of time during an STM movie by tracking the positions of individual Pt adatoms. The results from a movie are shown in figure 4.10.

In the first period, the diffusivity of the Pt adatoms is monitored on the clean surface (background pressure of 5.0×10^{-11} mbar). The average $\langle x^2 \rangle = 0.0025 \pm 0.0003 \text{ s}^{-1}$, in agreement with the previous results in [13]. Oxygen is then admitted to the vacuum chamber up to a pressure of 2.5×10^{-8} mbar. Oxygen adsorbs dissociatively on the surface at room temperature, and an oxygen coverage is built up as the exposure is continued [40]. The diffusion of the Pt adatoms still proceeds as a one-dimensional hopping along the missing-row troughs. The chemisorbed

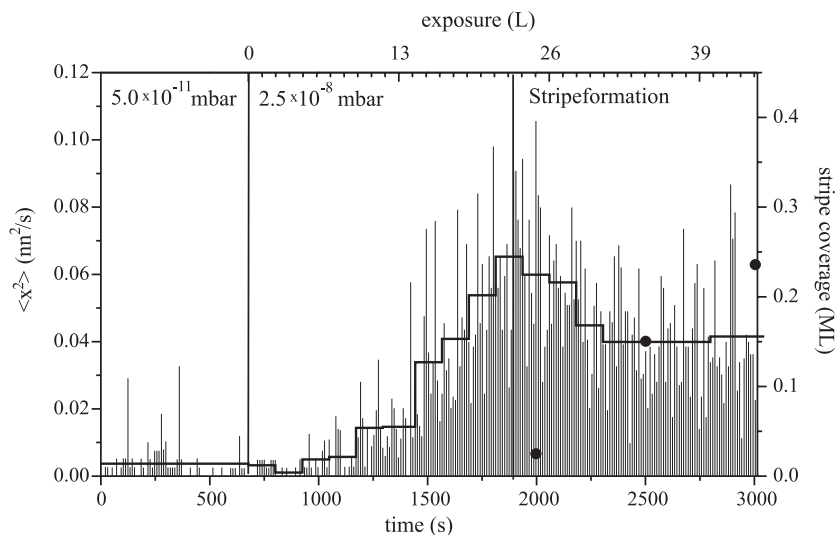


Figure 4.10: $\langle x^2 \rangle$ is shown versus time by the grey, vertical bars. Each bar corresponds to an average over ~ 30 events between two consecutive images in the STM movie. The black, horizontal line segments represent an average over $\langle x^2 \rangle$ in the corresponding time interval. After 678 s, indicated by the vertical line, an oxygen background pressure of 2.5×10^{-8} mbar is introduced to the UHV chamber. The oxygen exposure in the STM is shown on the upper vertical scale. After 22 L, the oxygen-induced stripes begin to evolve. The stripe coverage is indicated by the black circles. The movie is stopped after an exposure of 44 L. The film is acquired at 304 K and with 10.2 s per image. $I_t = 0.50$ nA and $V_t = -104.7$ mV. $\langle x^2 \rangle$ is given in units of nm^2/s , where nm is the nearest-neighbour distance in the $[1\bar{1}0]$ direction.

oxygen promotes the diffusivity of the Pt adatoms, and $\langle x^2 \rangle$ increases with increasing coverage up to an exposure of 22 L (figure 4.10).

The average $\langle x^2 \rangle$ is enhanced by a factor of ≈ 25 at maximum. The promotion effect of oxygen is thus less pronounced compared to the influence of hydrogen. No distinct change is observed in the appearance of the Pt adatoms. This does not, however, exclude the formation of Pt-O complexes with increased diffusivity. One could imagine that such complexes form without changing the LDOS at the Fermi level, so the complexes and clean adatoms actually become indistinguishable in STM. Further experimental studies combined with theory will hopefully establish a detailed picture.

After an exposure of 22 L, the oxygen-induced stripes begin to evolve, which has rather complicated consequences for the Pt adatom diffusivity. The Pt adatoms move back and forth along the troughs. The oxygen-induced stripes act repulsively against the diffusing Pt adatoms and confine them to move only in the parts of the troughs separating the stripe regions. The excursions of the individual adatoms are therefore limited, and this explains why the increase in $\langle x^2 \rangle$ is reduced at higher stripe coverages. A repulsive interaction between the Pt adatoms and the oxygen-induced stripes explains also why the oxygen pattern is able to confine the nucleation and growth of Pt as observed in figure 3.22 [41].

To summarize, oxygen coadsorption promotes the self-diffusion on the Pt(110)-(1 \times 2) surface. The effect is coverage dependent. As the oxygen pattern evolves, the diffusing Pt adatoms experience an inhomogeneous potential energy surface and are confined to move only in limited parts of the missing-row troughs.

4.4 Summary and outlook

In this chapter, mechanistic insight into hydrogen promotion of the self-diffusion on Pt(110)-(1 \times 2) is obtained. By STM, Pt-H complexes with an increased diffusivity of two orders of magnitude are directly observed. DFT calculations indicate that a Pt-H complex consists of a H adsorbed on-top a Pt atom and that the bound H atom decreases the diffusion barrier. A promotion of chemisorbed oxygen is also reported.

A such metal-adsorbate complex formation with an increased diffusivity may be a quite general phenomenon in gas-assisted sintering processes. Sintering (of e.g. supported catalyst particles) is in general comprised of a number of other elementary processes, including the formation of diffusing

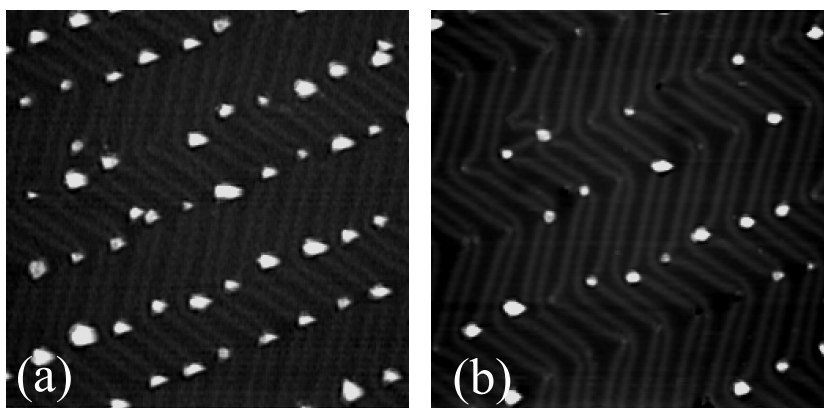


Figure 4.11: Co clusters on Au(111) exposed to H_2S (4×10^{-8} mbar) at room temperature. Two images from an STM movie acquired after exposures of (a) 4 L and (b) 177 L, respectively. The image size is $678 \text{ \AA} \times 740 \text{ \AA}$.

species, their migration across the support and subsequent recapturing to form larger clusters. In principle, adsorbates may influence any of these steps with crucial consequences for the overall agglomeration.

Recently, the group has initiated studies to gain further insight into gas-assisted sintering. Preliminary results of the ripening of Co clusters on Au(111) in an H_2S atmosphere are illustrated in figure 4.11. Cobalt is deposited onto the Au(111) surface under UHV and grows in highly dispersed clusters situated at the elbows of the herringbone reconstruction [42]. During exposure to H_2S , the coverage of the Co clusters on the terrace decreases exponentially in time due to a ripening of the individual metal clusters. The material is transported to step edges on the gold surface, where Co-S islands are formed (chapter 5). Thus, adsorption of H_2S greatly enhances the mass-transport of Co on Au(111). The action of the adsorbate is probably related to an enhanced formation of diffusing ad-species, as e.g. Co-S complexes, with a high surface diffusivity [43].

The present findings have an impact on many research areas where gas-surface interactions are of importance - besides sintering and catalysis also in areas such as chemical vapour deposition and crystal growth. Adsorbate-modified diffusion explains (at least in part) why sintering in heterogeneous catalysts depends crucially on the gas composition and why adsorbates can act as surfactants in metal-on-metal growth. With a bet-

ter systematic understanding of the phenomenon, gas adsorbates could be used to control diffusion of adatoms in surface processes.

References

- [1] M. Ø. Pedersen, L. Österlund, J. J. Mortensen, M. Mavrikakis, L. B. Hansen, I. Stensgaard, E. Lægsgaard, J. K. Nørskov, and F. Besenbacher, *Phys. Rev. Lett.* **84**, 4898 (2000).
- [2] S. Renisch, R. Schuster, J. Wintterlin, and G. Ertl, *Phys. Rev. Lett.* **82**, 3839 (1999).
- [3] J. Wintterlin, R. Schuster, and G. Ertl, *Phys. Rev. Lett.* **77**, 123 (1996).
- [4] J. V. Barth, T. Zambelli, J. Wintterlin, R. Schuster, and G. Ertl, *Phys. Rev. B* **55**, 12902 (1997).
- [5] S. Völkening, K. Bedürftig, K. Jacobi, J. Wintterlin, and G. Ertl, *Phys. Rev. Lett.* **83**, 2672 (1999).
- [6] J. Wintterlin, S. Völkening, T. W. Janssens, T. Zambelli, and G. Ertl, *Science* **278**, 1931 (1997).
- [7] B. G. Briner, M. Doering, H.-P. Rust, and A. M. Bradshaw, *Science* **278**, 257 (1997).
- [8] *Handbook of Heterogeneous Catalysis*, edited by G. Ertl, H. Knözinger, and J. Weitkamp (VHC Verlagsgesellschaft mbH, Weinheim, Germany, 1997), Vol. 3.
- [9] R. M. J. Fiedorow and S. E. Wanke, *J. Catal.* **43**, 34 (1976).
- [10] K. Wong, S. Johansson, and B. Kasemo, *Faraday Discuss.* **105**, 237 (1996).
- [11] P. J. F. Harris, *Nature* **323**, 792 (1986).
- [12] H. Graoui, S. Giorgio, C. R. Henry, and P. J. F. Harris, *Surf. Sci.* **417**, 350 (1998).
- [13] T. R. Linderoth, S. Horch, E. Lægsgaard, I. Stensgaard, and F. Besenbacher, *Phys. Rev. Lett.* **78**, 4978 (1997).
- [14] R. Gomer, *Rep. Prog. Phys.* **53**, 917 (1990).
- [15] G. Wahnström, in *Interaction of atoms and molecules with solid surfaces*, edited by V. Bortolini, N. H. March, and M. P. Tosi (Plenum Press, New York, 1990).

- [16] G. L. Kellogg, *Surf. Sci. Rep.* **21**, 1 (1994).
- [17] S. C. Wang, J. D. Wrigley, and G. Erhlich, *J. Chem. Phys.* **91**, (1989).
- [18] J. D. Wrigley, M. E. Twigg, and G. Erhlich, *J. Chem. Phys.* **93**, 2885 (1990).
- [19] F. Montalenti and R. Ferrando, *Phys. Rev. B* **58**, 3617 (1998).
- [20] H. T. Lorensen, J. K. Nørskov, and K. W. Jacobsen, *Phys. Rev. B* **60**, R5149 (1999).
- [21] P. J. Feibelman, *Phys. Rev. B* **61**, R2452 (2000).
- [22] G. L. Kellogg, *Phys. Rev. B* **55**, 7206 (1997).
- [23] G. L. Kellogg, *Phys. Rev. Lett.* **79**, 4417 (1997).
- [24] R. Stumpf, *Phys. Rev. B* **53**, R4253 (1996).
- [25] T. R. Linderoth, PhD thesis, University of Aarhus, Denmark, 1997.
- [26] J. R. Engstrom, W. Tsai, and W. H. Weinberg, *J. Chem Phys.* **87**, 3104 (1987).
- [27] G. Anger, H. F. Berger, M. Lugerand, S. Feistritzer, A. Winkler, and K. D. Rendulic, *Surf. Sci.* **219**, L583 (1989).
- [28] H. T. Lorensen, PhD thesis, Technical University of Denmark, Denmark, 1999.
- [29] J. Tersoff and D. R. Hamann, *Phys. Rev. Lett.* **50**, 1998 (1983).
- [30] P. Hofmann, S. R. Bare, and D. A. King, *Surf. Sci.* **117**, 245 (1982).
- [31] T. Gritsch, D. Coulman, R. J. Behm, and G. Ertl, *Phys. Rev. Lett.* **63**, 1086 (1989).
- [32] T. Gritsch, D. Coulman, R. J. Behm, and G. Ertl, *Appl. Phys. A* **49**, 403 (1989).
- [33] R. K. Sharma, W. A. Brown, and D. A. King, *Surf. Sci.* **414**, 68 (1998).
- [34] B. Hammer, O. H. Nielsen, and J. K. Nørskov, *Catal. Lett.* **46**, 31 (1997).

- [35] B. Hammer, Y. Morikawa, and J. K. Nørskov, *Phys. Rev. Lett.* **76**, 2141 (1996).
- [36] J. Fusy and R. Ducros, *Surf. Sci.* **237**, 53 (1990).
- [37] Q. Ge and D. A. King, *J. Chem. Phys.* **111**, 9461 (1999).
- [38] M. Kalff, G. Comsa, and T. Michely, *Phys. Rev. Lett.* **81**, 1255 (1998).
- [39] S. Johansson, K. Wong, V. P. Zhdanov, and B. Kasemo, *J. Vac. Sci. Technol. A* **17**, 297 (1999).
- [40] Y. Ohno and T. Matsushima, *Surf. Sci.* **241**, 47 (1991).
- [41] H. Brune, M. Giovannini, K. Bromann, and K. Kern, *Nature* **394**, 451 (1998).
- [42] B. Voigtländer, G. Meyer, and N. M. Amber, *Phys. Rev. B* **44**, 10354 (1991).
- [43] P. J. Feibelman, *Phys. Rev. Lett.* **85**, 606 (2000).

Chapter 5

Hydrodesulfurization model catalysts

Hydrotreating comprises the wealth of catalytic processes used in the oil industry to upgrade and convert crude petroleum feedstocks into the variety of oil products. These processes are some of the most important catalytic processes, and the annual sale of hydrotreating catalysts represents close to 10% of the total world market for catalysts. The most important of the hydrotreating processes is the hydrodesulfurization (HDS) reaction in which the dominant impurity sulfur is extruded from the crude oil fractions. The sulfur removal has a twofold purpose: first of all to reduce the sulfur outlets to the environment (in the form of SO_x which contributes to acid rain), and secondly to prevent sulfur poisoning of other catalysts in the refineries and car exhaust catalysts [1].

The field of HDS catalysis has recently attracted increased attention due to new severe environmental legislation. In both Europe and the U.S., this legislation requires a reduction of the maximum sulfur content allowed in, e.g., diesel products from 500 ppm to 50 ppm by the year 2004. Or stated differently, catalysts, which are at least five times more reactive than those used today, must be introduced [2]. Clearly, the new requirements for a deep desulfurization have large consequences for the industrial refineries, and significant efforts must be devoted to improve the processing schemes as well as to introduce new and more active catalysts [2, 3].

In order to aid the catalyst development, there has been a strong emphasis in the past on establishing fundamental relations between the catalyst structure and the HDS activity. Despite extensive studies over the last

50 years, where HDS catalysis have been used to purify crude oil, there are still many open questions regarding the atomistic description of the commonly used catalysts. The aim of the present study is to shed further light upon some of these issues by using STM to explore the atomic-scale structure of suitable model systems. The results (described in the papers [VI], [VII] and [VIII]) have already received much international attention [4, 5].

The outline of the present chapter is as follows: First, a brief introduction will be given to HDS catalysis (section 5.1). A more thorough overview of hydrotreating catalysis can be found in references [1, 6–10]. Then results concerning the formation and the characterization of a model system for unpromoted HDS catalysts will be presented (section 5.2). Finally, the structure of active sites (section 5.3) and the addition of promoters to the model system (section 5.4) are considered as well as a short outlook on future experiments (section 5.5).

5.1 Hydrodesulfurization catalysis

5.1.1 Hydrodesulfurization process

The hydrodesulfurization process is used to remove sulfur from the sulfur-containing organic compounds in the petroleum fractions. The process proceeds by trickling a mixture of crude oil and gaseous hydrogen over a bed of catalyst material [1], as illustrated in figure 5.1. Various *in situ* measurements have revealed that the active parts of the commonly used catalyst material consist of alumina-supported MoS₂ crystallites with small amounts of Co added as promoters [1].

The initial step in the catalytic cycle is concerned with adsorption of an organosulfur compound on a surface site of the catalyst particle. The subsequent steps involve hydrogenation (i.e. breaking) of sulfur-carbon bonds, desorption of a desulfurized organic compound, and finally removal of adsorbed sulfur by hydrogen in the form of hydrogen sulfide, which regenerates the active surface site. Thus, hydrogen acts as a reactant in the desulfurization process and is needed for creating active sites. After passing the catalyst reactor, the desulfurized oil and gaseous H₂S are then separated.

Typically, the HDS reactions are carried out at high temperatures of 300–400 °C and high pressures of 50–100 bar. The high temperature is required, since sulfur is strongly bonded in many of the sulfur-containing molecules, and the high hydrogen pressure ensures that the catalyst surfaces are not saturated with sulfur. The upper limit on both the tem-

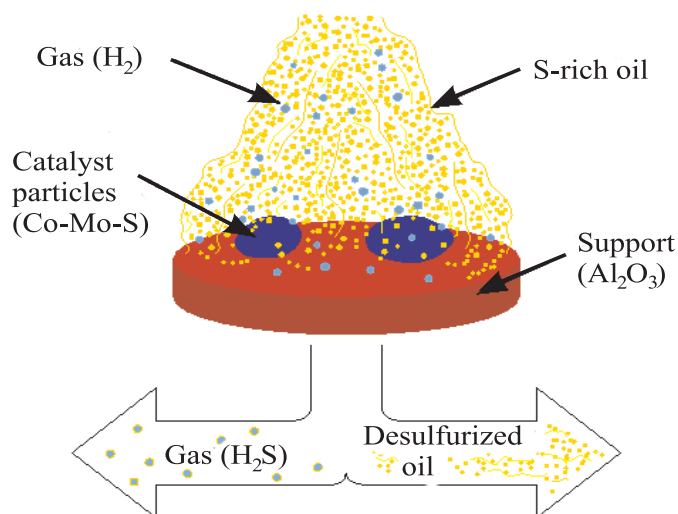


Figure 5.1: Schematic illustration of the HDS process. A mixture of sulfur-rich oil and gaseous hydrogen trickles over a bed of catalyst material. Sulfur is hereby removed from the organosulfur compounds in the petroleum fraction. Figure adapted from L. S. Byskov [6].

perature and the pressure is set by economy. Hydrogen is rather expensive. Furthermore, at elevated temperatures unwanted side reactions (reduced selectivity) may be initiated and also, a more rapid aging of the catalyst occurs, caused by sintering or coking [1].

The sulfur content in the crude petroleum varies from 0.1 wt% to 5 wt%, depending on geographic origin of the oil well [1]. The organosulfur molecules differ much in both size and structure which implies that large variations in their reactivity can be found. The oil contains thiols, sulfides and aromatic compounds as thiophenes. The main obstacle in achieving the demanded deep desulfurization, corresponding to a conversion of more than 95%, is the content of substituted thiophenes, like 4,6-dimethyldibenzothiophene ($C_{12}H_8S$), since such compounds are sterically hindered in the HDS process [2, 11].

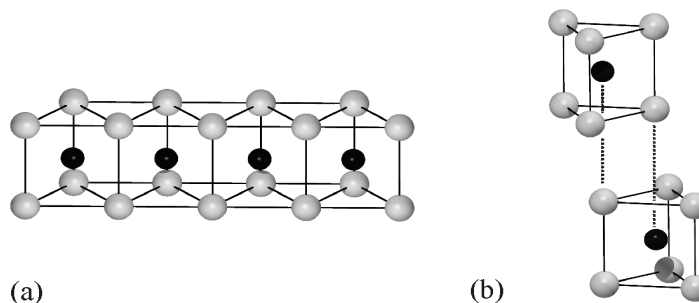


Figure 5.2: The crystal structure of MoS₂. (a) Sideview of a single-layer S–Mo–S slab. The S atoms (bright) and Mo atoms (dark) are hexagonally arranged. Within a MoS₂ slab, the S–S (and Mo–Mo) distance in the S (Mo) plane is 3.15 Å, whereas the S–Mo distance is 2.41 Å [15]. (b) Illustration of the 2H stacking sequence of two single-layer slabs. The distance between the metal layers in successive slabs is 6.15 Å [15].

5.1.2 Catalyst structure

In order to point out and to motivate the questions that the present model study will address, the current knowledge concerning the HDS catalyst structure is described in greater detail in this section.

Beginning with the structure of the *unpromoted* HDS catalyst, it has been established, largely by extended x-ray adsorption fine structure (EXAFS) measurements, that the commonly used catalysts consist of MoS₂ crystallites dispersed on a high-area porous γ -Al₂O₃ support. The MoS₂ nanocrystals are 10–20 Å wide after sulfidation at 300–400 °C [12, 13].

The crystal structure of MoS₂ is depicted in figure 5.2. MoS₂ is a layered compound consisting of stacks of S–Mo–S slabs held together by van der Waals interactions. Each slab is composed of two hexagonal planes of S atoms and an intermediate hexagonal plane of Mo atoms. The Mo atoms are trigonal-prismatically coordinated to the S atoms. In 2H-MoS₂, which is the common form found in nature [14], the unit cell contains two S–Mo–S slabs stacked as illustrated in figure 5.2.

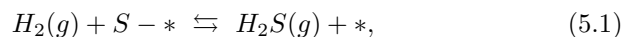
The MoS₂ nanocrystals can form two- as well as three-dimensional structures (in both the unpromoted and promoted catalysts): Type I catalysts consist of single-layer slabs and Type II catalysts consist of multiple slabs stacked on-top of each other. After sulfidation at ~ 673 K, mainly

single-layer slabs are present, whereas sulfidation at higher temperatures or extended use results in the formation of multi-layer slabs [16].

The morphology of the MoS₂ slabs is in principle determined by two types of low-indexed edge terminations, a ($\bar{1}010$) S-edge and a ($10\bar{1}0$) Mo-edge. In figure 5.3(a), the two edges are illustrated for a hypothetical hexagonal MoS₂ cluster, where the edges are simple terminations of the bulk MoS₂ structure.

The morphology of the MoS₂ nanocrystals has been studied by, e.g., transmission electron microscopy [17]. So far, insight from such investigations has been hampered by the amorphous and non-planar structure of the alumina support and by the small size of the crystallites, which are often too small to be resolved [1]. As a consequence, a number of questions related to the morphology of the catalyst particles is unsolved. For instance, are there any preferential shape of the MoS₂ clusters? To what extent does the relative stability of the edges depend on the preparation or the process conditions? What is the orientation of the crystallites relative to the substrate? And more interesting, what is actually the detailed atomic-scale structures of the edges? It is commonly assumed that the edges are obtained from a simple bulk truncation (figure 5.3) [1], but severe reconstructions may occur at the edges of the MoS₂ nanocrystals due to the reduced coordination of the edge atoms.

The interest in the edge structures is spurred by structure-activity studies. Such studies have found that the basal planes are inactive and that the HDS activity is uniquely related to the edges or corners of the MoS₂ crystallites in the unpromoted HDS catalysts [1, 18–21]. Moreover, it is commonly believed that fully sulfur-coordinated metal atoms in the sulfided catalysts are unable to adsorb sulfur-bearing molecules and that the active sites at the edges are therefore related to sulfur vacancies, i.e. coordinatively unsaturated metal sites (CUS). Such sites are provided by hydrogen stripping sulfur off the edges through reactions like



where * denotes an edge sulfur vacancy site. It is suggested that the number of sulfur vacancies is the key measure of catalytic activity. Experimentally [22] and theoretically [23, 24], it has been shown that the trend in the HDS activity follows the variation in the sulfur binding energy (describing the tendency to form S vacancies) for different transition metal sulfides, so that a weak sulfur bond correlates with a high HDS activity. Other features might be important as well (e.g. the sterical accessibility of the sulfur-containing molecules). At present, the nature of the active

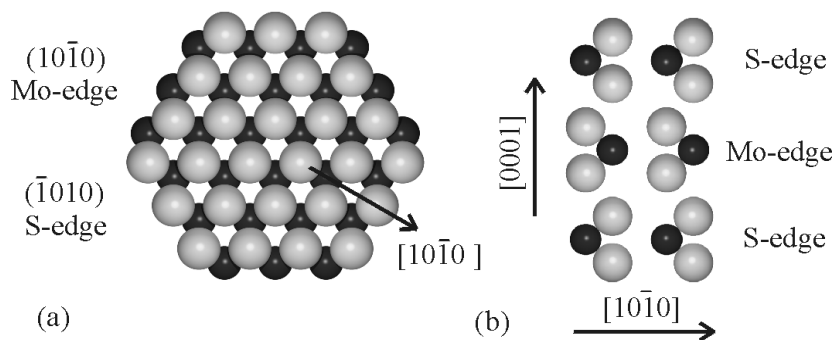


Figure 5.3: (a) A ball model (topview, along the $[0001]$ direction) of a MoS₂ hexagon, obtained from a simple bulk truncation. The Mo-edge and S-edge terminations are indicated. The Mo atoms (dark) at the S-edge and in the bulk are coordinated to six S atoms (light), whereas the Mo atoms at the Mo-edges are coordinated to only four S atoms. (b) A projected view of the 2H stacking sequence of three MoS₂ single-layer slabs. Successive single-layer slabs are terminated by alternately an S-edge and a Mo-edge.

site is still under intense debate. The discussion concerns the atomic-scale structure, the ability to form CUS on the different types of edges and also the adsorption properties of a CUS.

In order to increase the activity of the industrial catalysts, Co or Ni are added as *promoters* in the industrial HDS catalyst [1]. The well-accepted structural model for Co-promoted HDS catalyst is the so-called Co-Mo-S model, proposed by Topsøe and co-workers [1]. The structure of the Co-Mo/Al₂O₃ catalyst is quite complex, and structural insight has been obtained only by combining several *in situ* techniques including EXAFS, Mössbauer emission spectroscopy (MES), x-ray photoelectron spectroscopy (XPS) and infrared spectroscopy (FTIR). The multitude of techniques have revealed that the sulfided catalyst contains three different Co-phases (a schematic illustration is given in figure 5.4):

- Co dissolved in the alumina support
- Co in Co₉S₈ clusters
- Co in a mixed transition metal sulfide phase, the Co-Mo-S phase. This phase consists of Co incorporated in the edges of the MoS₂

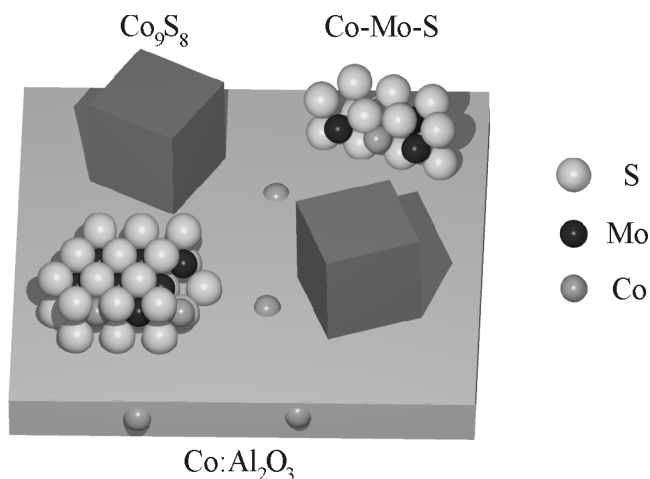


Figure 5.4: Schematic illustration of the Co-Mo-S model with the three different Co-containing phases. Adapted from [16].

crystallites and should be regarded as a family of clusters with a varying Co concentration.

The promoted HDS activity has been associated solely with the edge structures of the Co-Mo-S phase [1, 25]. Recent theoretical studies have suggested that the promotional effect of Co is to reduce the sulfur-binding energy and thereby increase the overall number of S vacancies at the edges of the MoS₂ crystallites [23, 24, 26]. A detailed description of the Co-Mo-S phase is still a matter of discussion, and the questions are related to both the morphology and the atomic-scale structure.

The picture of the working HDS catalyst presented above has emerged from an immense amount of studies, but it only provides an overall structural insight and is incomplete with respect to atomic details. The questions pointed out in this section are related to the structure and properties of the surfaces of the active catalyst particles. To address these issues, researchers have performed model studies in which a variety of surface-sensitive techniques are used to explore single-crystal surfaces under well-defined vacuum conditions, e.g. [27–30]. However, these studies have not provided any major breakthrough in the microscopic understanding. The main reason is that the single-crystal surfaces are simply inappropriate

model systems, since the HDS activity is related to defect sites on edges of MoS₂ nanoclusters [31]. Hence, more realistic model systems should be investigated.

One approach has recently been reported by Niemantsverdriet and co-workers (e.g. [31–33]): Model catalyst systems are prepared by impregnating flat oxidic model supports with precursor compounds of Mo (and Co) using spin coating. Subsequent sulfidation of these compounds results in the formation of MoS₂ or CoMoS clusters. These investigations focus on x-ray photoelectron spectroscopy studies of the sulfidation process and measure in addition the catalytic activities of the model system. The following will demonstrate another surface science approach in which MoS₂ nanoclusters are formed under UHV conditions on an inert gold substrate, and STM is used to characterize the structure of the clusters.

5.2 MoS₂ nanoclusters

The present chapter focuses on supported MoS₂ nanostructures as a model system for an unpromoted HDS catalyst. It will be demonstrated how MoS₂ nanocrystals, single-layer high and ~ 30 Å wide are synthesized on the Au(111) surface. By using STM, the morphology of the MoS₂ clusters is directly revealed and a detailed picture of the edge structures is obtained.

5.2.1 Experimental details

The experiments are performed in a standard UHV chamber with a base pressure better than 1×10^{-10} mbar. The chamber is equipped with the home-built, high-resolution STM described in chapter section 2.

The Au(111) surface is used as a model substrate. After an opening of the UHV chamber, the gold surface is cleaned by repeated cycles of sputtering by 1.5 keV Ar ion bombardment followed by annealing at 900 K, until it is judged clean by AES and STM. On a daily basis, the crystal is cleaned by a single cycle of sputtering and annealing.

Molybdenum disulfide (and Co-promoted MoS₂) nanoclusters are synthesized by depositing Mo (and Co) onto the clean Au(111) surface using an e-beam evaporator. The e-beam evaporator (Oxford Applied Research, model EGC04) is capable of depositing the metals simultaneously from separate pockets and offers the possibility to adjust the metal fluxes independently. The evaporator is loaded with rods of Mo (nominal purity of 99.9%) and Co (nominal purity of 99.99%). Furthermore, the evaporator is equipped with a high-voltage ion-retarding grid, which ensures that

only neutral atoms reach the gold surface. Prior to the experiments, the metals rods are thoroughly degassed and their cleanliness is checked by AES after deposition of several monolayers of Mo or Co on Au(111) under UHV conditions. Unless other conditions are explicitly specified, the coverage of Mo is $\approx 10\%$ (corresponding to a flux $\approx 1.7 \times 10^{-4}$ ML/s) and the coverage of Co is $\approx 4\%$ (flux $\approx 2.7 \times 10^{-4}$ ML/s), respectively. One monolayer equals the atom density in the unreconstructed surface layer of Au(111), $1 \text{ ML} = 1.39 \times 10^{19} \text{ m}^{-2}$. The coverage of Mo (Co) is determined by STM after UHV deposition of Mo (Co) onto the clean Au(111) surface kept at room temperature. During UHV deposition, the chamber pressure increases slightly, but it is always less than 5×10^{-10} mbar.

In order to sulfide the deposited Mo (Co), the gold sample is exposed to gaseous hydrogen sulfide (H_2S). The nominal purity of the H_2S gas is 99.8%, and no further purification is done in this work. In the beginning of the project, H_2S was introduced to the vacuum system as a background atmosphere at a constant pressure of 1.0×10^{-6} mbar (corresponding to an impinging flux of H_2S molecules on the surface of 0.2 ML/s). The gas composition was monitored by a quadrupole mass spectrometer and consisted of mainly hydrogen, water, carbon monoxide and hydrogen sulfide with relative intensities 1/2 (of mass 2), 1/20 (mass 18 and 28) and 1 (mass 34), respectively.

From the experiments, it turns out that a rather large exposure of $\sim 2700 \text{ L}$ and the high gas flux are required to form MoS_2 . As a consequence of reaction with the chamber walls, the base pressure increased to about 3×10^{-9} mbar in the period where the sulfidation experiments were performed. The background consisted mainly of hydrogen, water and hydrogen sulfide. In order to reduce the huge gas loadings and improve the subsequent vacuum conditions, a molecular beam doser, based on a design similar to that reported in [34], was installed and used later on. In the gas doser, the H_2S gas effuses from a reservoir through a $\sim 2 \mu\text{m}$ diameter pinhole aperture. A tube directs the gas onto the sample surface, so that a high local flux is obtained without a large increase in the background pressure. The pressure in the gas reservoir controls the effusion rate and thus the H_2S flux onto the sample. Using a gas reservoir pressure in the range 120-170 torr, the ensemble of nanoclusters synthesized on the gold substrate is identical with the ensemble obtained from the backfilling method. This serves as a calibration of the effusion source, and only gas reservoir pressures in this particular range are applied. Using the gas doser, the background pressure is reduced to roughly 4×10^{-8} mbar during the sulfidation procedure, and the base pressure in the UHV system is

improved by an order of magnitude to about 3×10^{-10} mbar.

5.2.2 Preparation of MoS₂ nanoclusters

The Au(111) surface is chosen as a model substrate, since gold is noble and chemically inert [35], and since the characteristic “herringbone” reconstruction, which exists for this surface [36], is ideal for providing nucleation sites for epitaxial growth of highly dispersed metal islands [37–41].

The reconstruction of Au(111) is driven by the reduced coordination of the surface atoms [42–44]. The reconstruction is characterised by a $(22 \times \sqrt{3})$ unit cell, in which the gold atoms in the topmost surface layer are compressed gradually by $\sim 5\%$ along the $[1\bar{1}0]$ direction [36]. Due to this contraction, the gold atoms form alternating broad fcc and narrow hcp stacking regions running parallel along the $[11\bar{2}]$ direction. Gold atoms located near bridge positions appear as brighter lines in the STM images and separate the fcc and hcp areas, as shown in figure 5.5(a). Long-range elastic interactions introduce domain boundaries, approximately every 140 Å [45]. At the boundaries, the domains bend by alternating $\pm 120^\circ$, and a zigzag pattern often referred to as the “herringbone” reconstruction forms (figure 5.5(b)). On a length scale even larger than the image size of figure 5.5(b), three rotational domains appear, and thus the stress relief effectively becomes isotropic. At the domain walls, two types of elbows are observed, a pinched and a bulged elbow. The latter, which is associated with a surface dislocation [38], acts as the preferential nucleation site in the epitaxial growth of a number of different metals [37–41].

Indeed, when a submonolayer of molybdenum is deposited on the gold (111) surface, a self-assembled regular array of one or two layer high Mo islands is formed, extending over a mesoscopic length scale (figure 5.6). Thus, the Au(111) surface acts as a template to disperse the Mo into islands of similar size. The narrow size distribution ensures a homogeneous degree of sulfidation of the metal clusters.

In order to sulfide the Mo, a number of different procedures with varying preparation parameters (the fluxes of Mo and H₂S, the substrate temperature and the total exposures) have been investigated. The scope of the present context is to characterize the atomic-scale structure of the sulfided Mo clusters, and the following discussion will therefore take the procedure, which results in the most homogeneous ensemble of clusters with respect to size and morphology, as a starting point.

In this “standard procedure”, the Mo deposition is done while the gold substrate is exposed to H₂S (figure 5.7 shows the surface temperature

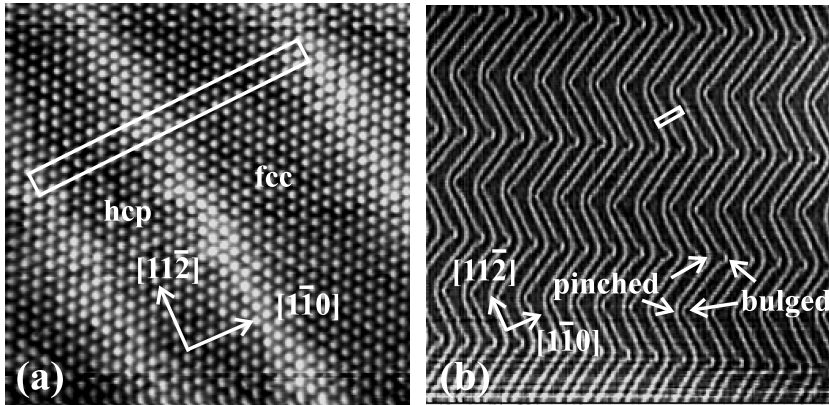


Figure 5.5: (a) Atom-resolved STM image of the reconstructed Au(111) surface. The square shows the $(22 \times \sqrt{3})$ unit cell. In between the brighter lines, the fcc (hcp) stacking region is identified as the broader (narrower) area, in accordance with reference [36]. Size $87 \times 90 \text{ \AA}^2$. (b) Large-scale STM image showing the herringbone superstructure. The $(22 \times \sqrt{3})$ unit cell, the bulged and the pinched elbow sites are indicated. Size $1211 \times 1227 \text{ \AA}^2$.

during the standard preparation). The high dispersion and preferential positioning at the elbow sites still prevail for the molybdenum clusters, but their shape appear more irregular than in figure 5.6. In order to crystallize these clusters, the sample is subsequently postannealed in the H_2S atmosphere at 673 K for 15 min. When the sample has cooled to 370 K, the H_2S exposure is terminated and the sample is transferred to the STM. This procedure transforms the majority of the clusters into crystalline MoS_2 nanoclusters (see figure 5.8).

Auger electron spectroscopy (AES) is used to characterize the chemical composition of the sample. AES spectra acquired of the clean Au(111) surface and the Au(111) surface exposed to H_2S , following the standard procedure but without Mo deposition, show no differences in neither peak positions nor intensities, confirming that H_2S does not adsorb. The AES measurements are combined with STM measurements, which also confirm the inertness of the Au surface toward H_2S adsorption. In addition, TPD experiments show that H_2S desorbs from Au(111) at substrate temperatures between 100 K and 160 K [46]. Furthermore, an AES spectrum is obtained after the standard sulfidation of Mo. This spectrum shows dis-

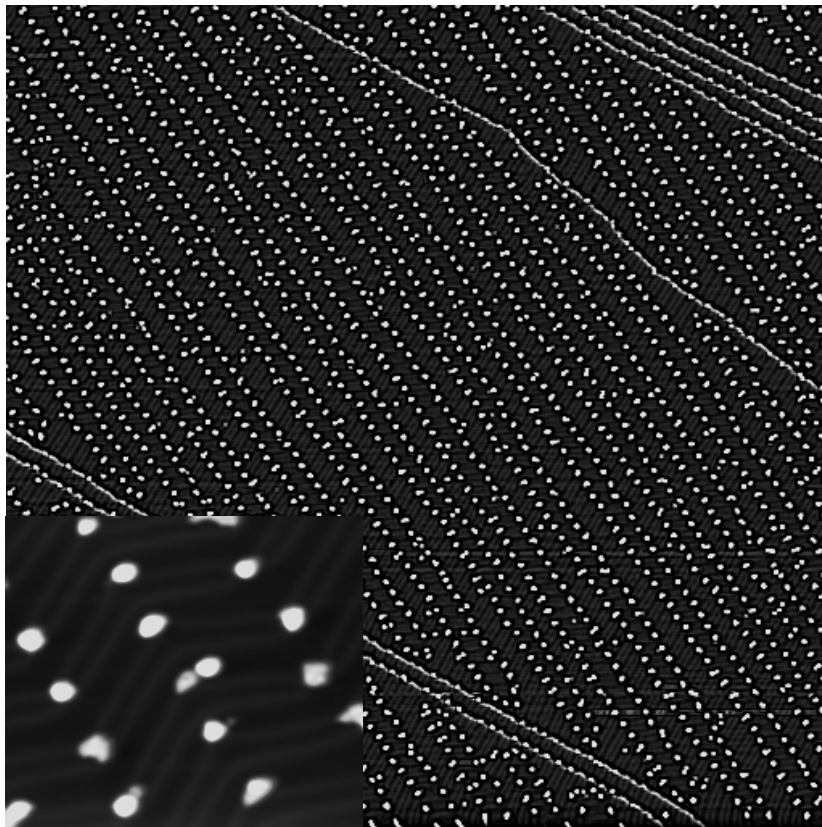


Figure 5.6: An STM image ($4035 \times 4090 \text{Å}^2$) of Mo deposited onto Au(111) at 307 K under UHV conditions. The insert is a close-up ($397 \times 354 \text{Å}^2$) showing the herringbone reconstruction of the Au(111). The regular array of bulged elbows acts as a template of nucleation sites for the epitaxial growth of Mo.

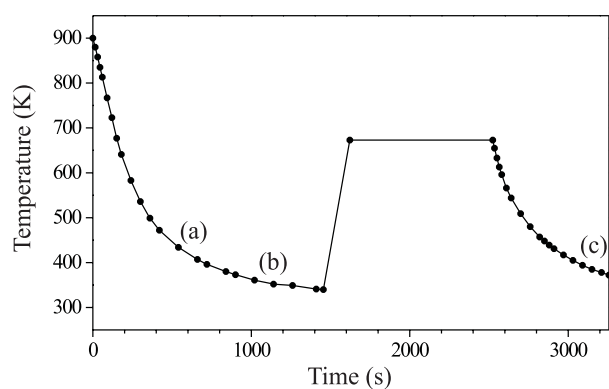


Figure 5.7: Illustration of the substrate temperature during the standard preparation. The gold crystal cools down from annealing to 900 K. At 450 K, the H_2S gas is introduced. The Mo deposition begins at 420 K (a) and ends at 357 K (b), when a Mo coverage of 10% is reached. To crystallize the sulfided metal clusters, the sample is postannealed at 673 K for 15 min. The chamber is evacuated for the H_2S gas when the sample temperature is 370 K (c). The time interval between (a) and (c) is 45 min. In experiments, where H_2S is adsorbed from a background atmosphere, the total H_2S exposure corresponds to 2700 L. When the gas doser is used as H_2S source with a reservoir pressure in the range 120-170 torr, the standard procedure results in a MoS_2 cluster ensemble identical to that obtained from the “backfilling” method.

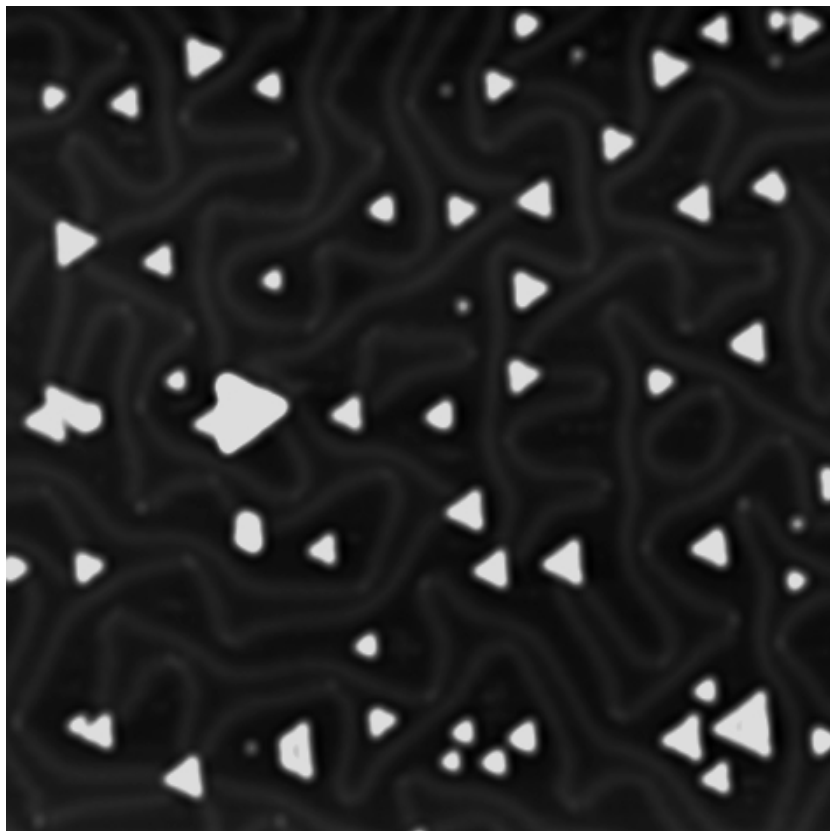


Figure 5.8: An STM image of the ensemble of MoS₂ clusters on the Au(111) surface, resulting from the standard preparation. Size $744 \times 721 \text{ \AA}^2$.

tinct peaks of both Mo and S, and it is concluded that H_2S binds to Mo. In principle, it is possible to determine the ratio of Mo/S from AES, but in order to obtain an appreciable intensity, the spectrum was acquired with a Mo coverage of 60%. In this case the collection of MoS_2 clusters is very inhomogeneous in size and shape, which makes it a considerable task to relate the integral AES signal to the cluster composition. Further experiments are planned for obtaining a quantitative analysis in the low-coverage regime.

The gold surface was shown to act as a template for dispersing the deposited Mo, but as illustrated in figure 5.8, the long-range elastic interactions in the substrate are distorted after the standard preparation. By comparing STM images obtained before and after the postannealing, it appears that the distortion of the herringbone pattern happens during the postannealing process and only when Mo is present on the surface. A possible explanation for this phenomenon is that the surface stress is changed by a fraction of the molybdenum diffusing into the substrate at the elevated temperatures [47]. In this exchange process, Au atoms are expelled onto the surface and probably diffuse around until they are captured by a step edge. A similar scenario has been observed when a submonolayer of Ni deposited on Au(111) is annealed under UHV conditions [48]. In the standard preparation, the island coverage does not change before and after the postannealing process. However, the sulfided Mo islands prior to the postannealing are not well-characterized, so the Mo concentration in these islands may differ from the amount of Mo in the MoS_2 nanocrystals. For instance, assuming that the sulfided Mo clusters consist of one Mo layer grown pseudomorphically on unstrained Au(111), these clusters contain $\sim 20\%$ more Mo than the MoS_2 clusters. Thus, it may be that small amounts of Mo dissolve in the Au(111) surface during the postannealing and distort the surface stress. Concerning the island density, it is reduced by roughly a factor of two to $1 \times 10^{-4} \text{ \AA}^{-2}$ (and the island sizes increase) after the postannealing. Thus, a minor agglomeration of the dispersed islands occurs during the postannealing process. However, the size distribution of the resulting collection of MoS_2 clusters is still very narrow. Section 5.2.4 elaborates on this point.

To summarize, the standard preparation results in an ensemble of nanoclusters with a narrow size distribution and a dominant triangular morphology. The ensemble therefore forms a well-characterized reference for further experiments. The following sections will focus on the structure of the clusters.

5.2.3 Characterisation

The triangular clusters resulting from the standard preparation procedure are characterized by atom-resolved STM images. In figure 5.9, the STM image illustrates that the clusters contain a plane of hexagonally arranged protrusions with an average interatomic spacing of $3.15 \text{ \AA} \pm 0.05 \text{ \AA}$. This is exactly the interatomic spacing of S atoms in the (0001) basal plane of MoS_2 .

As pointed out previously, low bias, constant current STM images reflect in general the electronic rather than the geometric structure of the surface. This has generated some controversy in the literature concerning the interpretation of atom-resolved STM images of the (0001) basal plane of single-crystalline MoS_2 . The debate stems from the fact that the hexagonal sulfur and molybdenum lattices are identical, and it is therefore not *a priori* clear whether hexagonally arranged protrusions reflect the S atoms in the surface layer or the Mo atoms in the second layer [49, 50]. STM calculations using the Tersoff-Hamann scheme [51] and the ESQC formalism [52] have, however, shown that on layered MoS_2 slabs only the S atoms in the topmost layer are imaged for typical tunnel distances.

Since the STM images do not change by variations in the tunnel current, the triangular-shaped islands are interpreted as MoS_2 nanocrystallites with their (0001) basal plane oriented parallel to the Au substrate surface and with the protrusions reflecting the hexagonally arranged S atoms in the topmost S layer. The MoS_2 nanocrystals have an apparent height of only $2.0 \pm 0.3 \text{ \AA}$, which is slightly smaller than the geometrical distance of 3.16 \AA between the S layers in a MoS_2 slab. This is probably due to the fact that STM probes the electronic structure of the surface. Hence, it is concluded that the MoS_2 nanoclusters are present as single-layer slabs on the Au surface, i.e. only one of the two building blocks in the unit cell of 2H- MoS_2 is present.

It is important to point out that molybdenum disulfide is a semiconductor with a bandgap of 1.23 eV [53]. The appearance of the gold-supported MoS_2 nanoclusters does not change in the STM images when the bias voltage is varied, even for bias voltages numerically less than half the size of the band gap in bulk MoS_2 . This suggests that the electronic structure of the MoS_2 nanoclusters is perturbed compared to the bulk crystal. In order to shed further light on this, density functional theory (DFT) calculations have recently been performed by M. Bollinger at the Technical University of Denmark [54]. In the calculations, a single-layer MoS_2 slab is adsorbed on a Au(111) substrate. It is found that there is a weak interaction be-

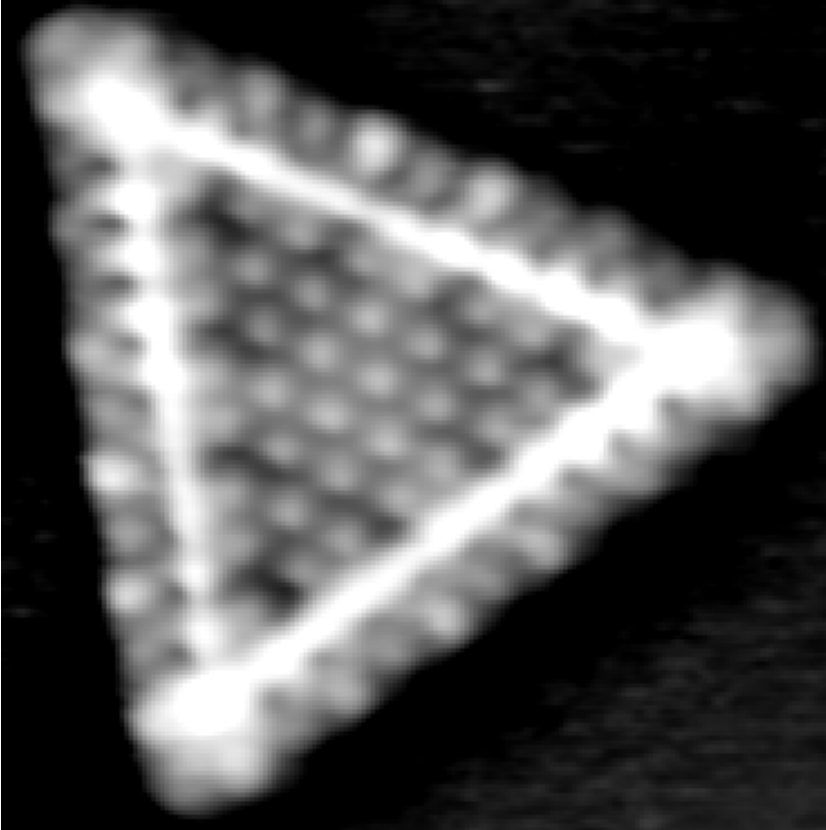


Figure 5.9: An atom-resolved STM image of a MoS_2 nanotriangle. Size $41 \times 42 \text{ \AA}^2$, $I_t=1.28 \text{ nA}$, $V_t=5.2 \text{ mV}$.

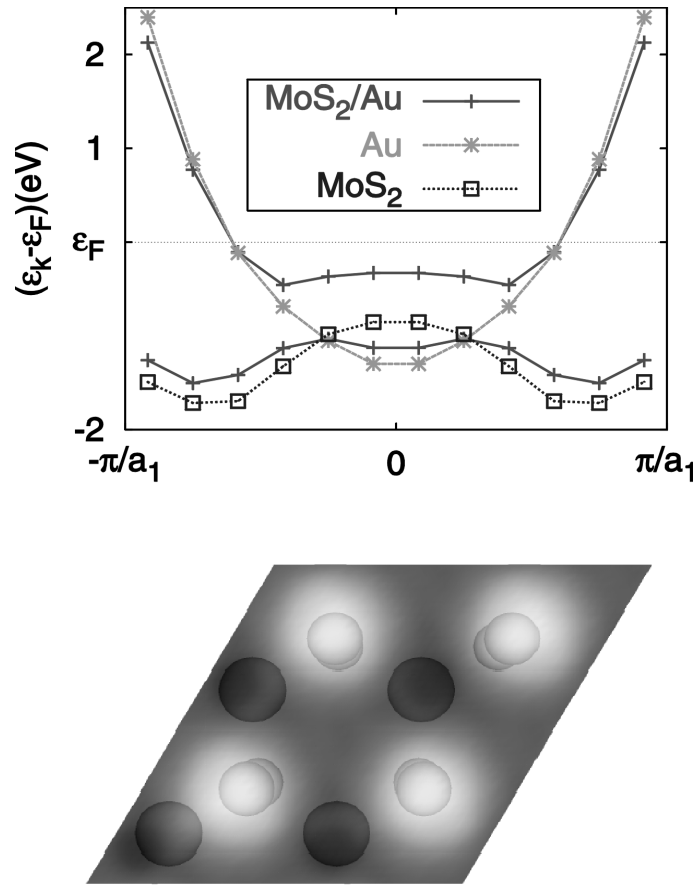


Figure 5.10: The band structure shows two bands for a single-layer MoS₂ slab on Au(111) (with a lattice constant of 3.2 Å). These bands are mainly a result of the interaction between a Au and a MoS₂ band, which are shown in addition. The close-packed directions, termed \vec{a}_1 , on Au(111) and MoS₂ are chosen to coincide, in accordance with experimental observations. The simulated STM image shows a (1×1) unit cell of the (0001) basal plane of MoS₂ on Au(111). The calculated STM image tracks a constant LDOS = 9.2×10^{-6} (electrons)/eVÅ³ at E_f . At this value, the corrugation along the close-packed direction on the S lattice is the same as that measured experimentally (~ 0.22 Å). The large and small circles superimposed in the image indicate the positions of Mo and S, respectively. Figure in courtesy of M. Bollinger.

tween the gold surface and the MoS_2 layer. The dispersion curves for two electronic bands for the combined MoS_2/Au system are shown in figure 5.10. These bands are derived mainly from the interaction of a Au *s*-band and the highest occupied MoS_2 band, which are also shown. Near the centre of the Brillouin zone, a large splitting of the electronic states for the MoS_2/Au system is found. Further out in the Brillouin zone, where there is a large separation in energy of the Au and MoS_2 band, the bands in the $\text{MoS}_2/\text{Au}(111)$ system follow closely either the Au band or the MoS_2 band, respectively. For the combined system, the states passing the Fermi level contain a small component of MoS_2 , i.e. the gold substrate lifts MoS_2 states up to the Fermi level. This explains why single-layer MoS_2 can be imaged on Au(111) for bias voltages less than half the size of the bulk band gap (numerically). The corresponding simulated STM image, i.e. the contours of constant LDOS at the Fermi level, of the (0001) basal plane of the MoS_2 on Au(111) is shown in figure 5.10. From the image, it appears that protrusions reflect the positions of sulfur atoms in the outermost plane of the MoS_2 surface. Thus, it is concluded that, as a result of an electronic interaction between MoS_2 and a gold substrate, STM images the S atoms in the (0001) basal plane of MoS_2 as protrusions, even for bias voltages in the bulk MoS_2 band gap.

5.2.4 Morphology

The shape of the MoS_2 clusters is determined by the relative stability of the Mo-edge and the S-edge. Since the HDS reactivity is related to the edges of the particles in the real catalyst and since the reactivity of the two types of edge terminations might differ, it becomes interesting to examine the morphology of the MoS_2 nanoclusters and to see how the morphology can be modified.

The MoS_2 clusters resulting from the standard preparation are surprisingly similar: The majority (84%) of the particles are directly associated with MoS_2 nanocrystals. Zooming in on any of these clusters, they appear to be oriented with the (0001) basal plane parallel to the gold substrate, as illustrated for the triangle in figure 5.9. The remaining clusters are either partly sulfided, non-crystalline Mo clusters or too small to be characterized. Among the MoS_2 crystallites the predominant shape is the triangular structure found for 91.3% of the nanocrystals. The remaining clusters are truncated triangles (4.4%), rhombs (1.3%), pentagons (0.7%) or hexagons (0.3%). The last 2% of the clusters have a shape, which is merged from the simpler geometrical forms. Thus, the morphology the nanocrystals

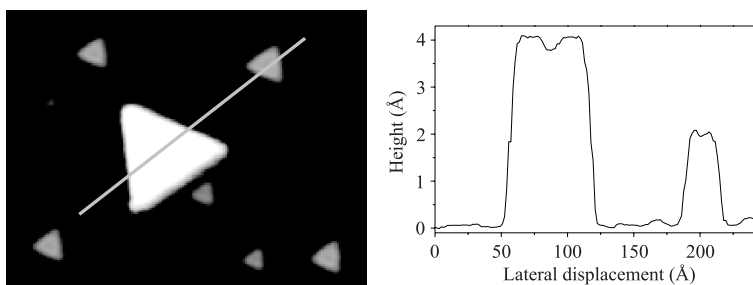


Figure 5.11: A two-layer high MoS₂ cluster appears brighter and larger compared to the single-layer slabs. The linescan indicates the height of a single-layer and a double-layer MoS₂ nanocrystal.

reflects the hexagonal-crystalline symmetry of MoS₂ and the majority of the MoS₂ nanoclusters has a triangular shape under the present sulfiding conditions.

From the height of the MoS₂ clusters (~ 2 Å), it is concluded that they are present as single-layer high particles. However, around 1% of the MoS₂ nanocrystals are actually found to be ~ 4 Å high triangles (see figure 5.11). These clusters have exactly the same hexagonal lattice as the single-layer clusters (figure 5.9) and are therefore interpreted as two-layer high MoS₂ clusters. The geometrical height of the two-layer slab from the lowest S-plane to the uppermost is 9.31 Å. The considerably smaller height observed for the two-layer slabs is attributed to a significantly altered electronic structure of the cluster compared with bulk MoS₂.

The single-layer MoS₂ slabs are also very similar with respect to size. The size distribution in figure 5.12 shows that the triangles have a side length of ~ 30 Å corresponding to the spatial extension of the clusters present in typical HDS catalysts. The size distribution of the MoS₂ triangles is furthermore very narrow. Thus, despite the agglomeration in the postannealing process, the gold substrate is still able to confine the material locally. A tentative explanation is that the brighter dislocation lines act repulsively towards the diffusing species.

According to the crystal structure of MoS₂, there is only one type of edge termination in a triangular-shaped cluster and, as will be evident from the discussion in the section 5.2.5, all the triangles have the same edge termination. Since the relative stability of the Mo-edge and the S-edge terminations determines the shape of the MoS₂ clusters, the observed

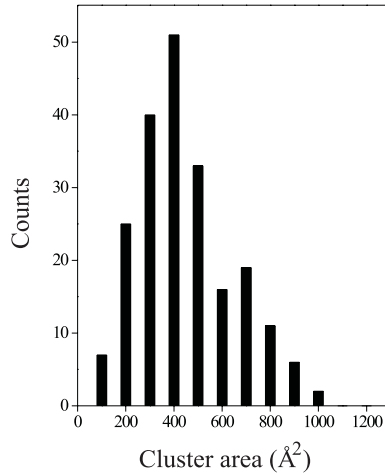


Figure 5.12: Size distribution for the single-layer MoS_2 triangles. The mean cluster area is 450 \AA^2 , corresponding to a mean side length of 32 \AA of equilateral triangles. The standard deviation is 207 \AA^2 and the bin size is 100 \AA^2 .

triangular morphology therefore implies that one of the edge types is far more stable than the other, and this implies further that the equilibrium shape is a triangle.

The equilibrium shape of a single-layer MoS_2 crystal is the form which minimizes the total free energy of the cluster edges, i.e. the sum over all edge free energy times the corresponding edge length ($\sum_i \gamma_i \times l_i$). This condition is fulfilled for the two-dimensional Wulff construction [55, 56]: The equilibrium shape of a single-layer MoS_2 cluster is inferred from a geometrical construction in which the $(10\bar{1}0)$ and $(\bar{1}010)$ vectors are plotted with a common origin and with a length proportional to the surface free energy of the Mo-edge and the S-edge, respectively. The inner envelope of the tangent planes, placed at the end of each radius vector, describes the equilibrium shape of the cluster in real space. The relative edge energies of the Mo-edge and S-edge determine whether the equilibrium shape is a triangle or a hexagon, as illustrated in figure 5.13. On the contrary, a multi-layer cluster (or a bulk crystal) is expected to grow in a hexagonal form only, since in the 2H bulk stacking sequence, successive MoS_2 layers will expose alternately a Mo-edge and a S-edge (see figure 5.3), and thus the difference in edge energies tends to cancel out.

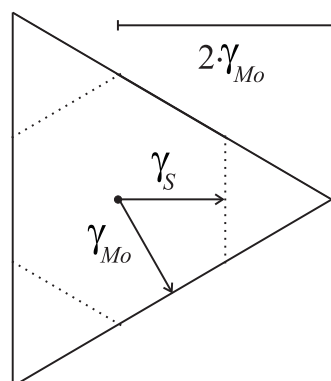


Figure 5.13: A 2D Wulff-type construction for the single-layer MoS_2 cluster. In a polar plot of the $(10\bar{1}0)$ and $(\bar{1}010)$ radius vectors with length proportional to the surface free energy of the Mo-edge (γ_{Mo}) and S-edge (γ_S), the real-space shape is obtained as the inner envelope of the tangent planes to these vectors. For example, the equilibrium shape is a triangle terminated by Mo-edges if $\gamma_S \geq 2 \times \gamma_{Mo}$ (as indicated by the full lines) and a hexagon if $\gamma_S = \gamma_{Mo}$ (as shown by the dotted lines).

Based on these considerations, the dominant triangular morphology of the single-layer MoS_2 clusters implies that the ratio of the specific surface free energy of the Mo-edge to the S-edge is at least a factor of two, or vice versa, depending on which edge is the more stable one. It should be added that the Wulff construction is a thermodynamic equilibrium description. The minor fraction of single-layer truncated triangles, rhombs etc. as well as the double-layer triangular clusters reveals that some kinetic limitations are present. Similarly, corner effects, which are of more importance as the crystallites become smaller, are not included in this description [57].

The phase space of different preparation parameters has been thoroughly investigated in order to find the parameters used in the standard preparation. The remaining part of this section will focus on the influence of increasing postannealing temperature, which plays an important role in the crystallization of the MoS_2 nanoclusters.

First of all, when the postannealing temperature is increased, the single-layer MoS_2 clusters change from having a dominantly triangular form to be shaped as trapeziums, rhombs, pentagons, hexagons, and other shapes obtained from a triangle as the basic unit (see figure 5.14 (a) and

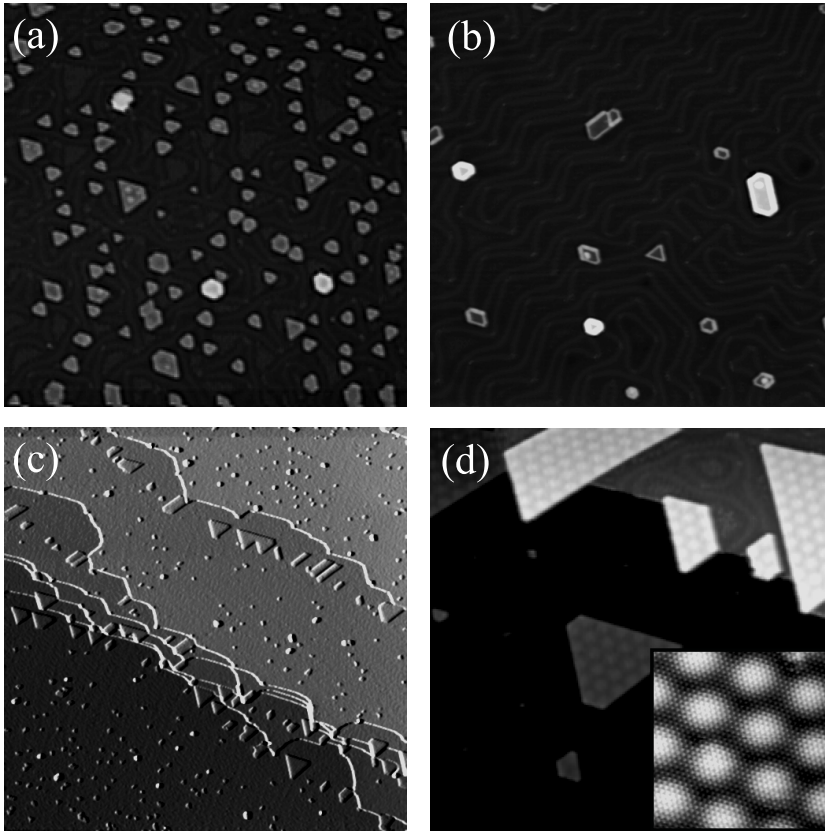


Figure 5.14: STM images showing the morphology of the MoS_2 clusters as the postannealing temperature is increased in (a) to 773 K and in (b) to 823 K. The size of both images is $1013 \text{ \AA} \times 1102 \text{ \AA}$. (c) A large-area STM image of the sample in (b). Size $5065 \text{ \AA} \times 5510 \text{ \AA}$. (d) A close-up on large single-layer islands near the Au(111) step edges in (c). Size $709 \text{ \AA} \times 771 \text{ \AA}$. The insert is an atom-resolved STM image of the basal plane on a large MoS_2 cluster. Size $101 \text{ \AA} \times 110 \text{ \AA}$.

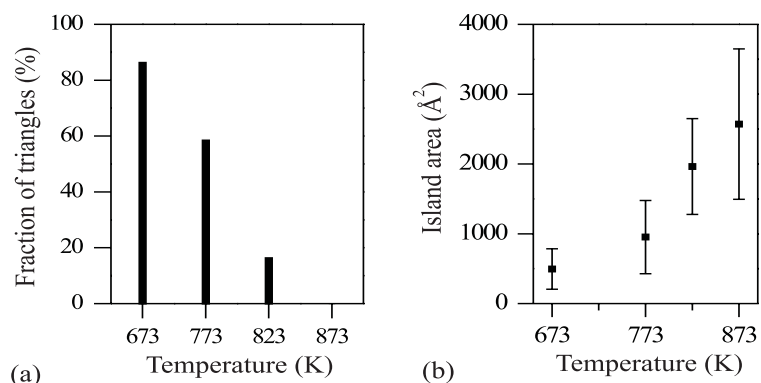


Figure 5.15: (a) The fraction of triangular single-layer clusters relative to the total number of single-layer MoS₂ clusters is plotted versus the postannealing temperature. (b) Mean size of the single-layer MoS₂ plotted versus postannealing temperature. The error bars shows the standard deviation of the size distribution.

(b)). Figure 5.15(a) shows how the number of triangles relative to the total number of MoS₂ nanocrystals (including clusters with three up to six edges) develops as a function of increasing postannealing temperature. According to the crystal structure, clusters with four, five and six edges must contain both Mo-edges and S-edges. Thus, a higher postannealing temperature introduces a larger multitude of cluster shapes, corresponding to a larger number of the less stable edge type.

The second consequence of increasing the postannealing temperature is that the mean size of the single-layer MoS₂ slabs increases and the size distribution broadens (figure 5.15(b)). Furthermore, the cluster coverage decreases on the terraces (figure 5.14 (a) and (b)), and larger single-layer MoS₂ platelets grow near step edges on the gold substrate. Thus, the cluster size distribution effectively becomes bimodal (figure 5.14(c)). It should be added that only the single-layer islands far from the step edges contribute in figure 5.15, and that the total coverage of single-layer slabs stays constant in the different preparations. Similar results are found for the double-layer slabs, i.e. the coverage is constant and the size increases with increasing temperature. Thus, as the postannealing temperature is raised, an agglomeration of the initially well-dispersed sulfided metal islands becomes more pronounced. Apparently, the gold substrate loses its

ability to confine the material locally. The agglomeration probably happens due to cluster diffusion or evaporation and subsequent diffusion of metal atoms or sulfur-metal complexes, followed by recapturing by other islands either on the terraces or near step edges.

At first glance, it seems contradictory that a higher postannealing temperature results in a lower fraction of triangles, which was suggested to be the low-energy form. However, this tendency is reversed if the postannealing period is increased. For instance, annealing at 823 K for 30 min. instead of 15 min., the fraction of single-layer MoS_2 triangles increases from 15% to 25%, without any significant increase in the mean island size. Thus, it can be concluded that the triangular shape is the equilibrium form of the single-layer high MoS_2 clusters. The larger cluster sizes at higher postannealing temperatures simply impede the equilibration of the cluster shape. Concerning the two-layer high MoS_2 particles, figure 5.14 (a) and (b) show that they approach a more hexagonal shape, as expected.

Atom-resolved STM images reveal that the close-packed directions on the gold substrate and on the MoS_2 basal plane coincide. This demonstrates an interaction between the MoS_2 cluster and the gold substrate, as also discussed in section 5.2.3. Furthermore, a hexagonal superstructure with a periodicity of $\sim 33 \text{ \AA}$ is observed on the larger MoS_2 islands in figure 5.14(d). This can be accounted for as a Moiré overlayer pattern. In a non-rotated hexagonal overlayer (with lattice constant a_o) on a hexagonal substrate (with lattice constant a_s), atoms in the overlayer will reside alternately in on-top sites and high-coordination sites on the substrate. Consequently, a buckling with a periodicity of $a_s \times a_o / (a_o - a_s)$ is introduced in the overlayer [58]. From the insert in figure 5.14(d), it is found that $a_o = 3.15 \text{ \AA}$, and, assuming that the gold underneath the MoS_2 is unreconstructed, i.e. $a_s = 2.88 \text{ \AA}$, the calculated moiré periodicity is 33.6 \AA , in agreement with the measured period. The moiré superstructure is most likely a structural effect resulting from the fact that the MoS_2 single-layer slabs are laterally stiff (the lattice constant is preserved) and vertically flexible. A such flexibility of MoS_2 structures has been observed in electron micrographs of nanometer-sized MoS_2 fullerene- and tube-like structures [59, 60].

To summarize, with respect to both morphology and size, a marked homogeneity characterizes the ensemble of MoS_2 nanoclusters resulting from the standard preparation. The triangular shape is found to be the low-energy form of the single-layer MoS_2 nanocrystals under the present sulfiding conditions. It is demonstrated that the ensemble of clusters resulting from the standard preparation represents a state of quasi-equilibrium,

i.e. by varying the crystallization parameters (postannealing temperature and period), a multitude of cluster shapes can be formed. The triangular equilibrium form may be a unique feature for the single-layer MoS₂ clusters, and the fact that it differs from the hexagonal equilibrium form of the double-layer clusters might be interesting, since previous studies have shown that type I and type II catalysts have different catalytical properties [1, 20].

5.2.5 Edge structures

A detailed description of the edge structures of single-layer MoS₂ nanoclusters is inferred from atom-resolved STM images. In figure 5.16, a grid is superimposed on an STM image of a MoS₂ triangle. It is found that the edge protrusions are out of registry with those on the basal plane. The reconstructed geometry is found to be general for the single-layer MoS₂ nanotriangles.

Assuming that the edge protrusions are also associated with S atoms, it is concluded that the S atoms at the edges are out of registry with the S atoms in the hexagonal lattice of the basal plane. In fact, the S atoms are observed to be shifted by half a lattice constant along the edges.

The question as to which type of edge termination is the more stable one is complicated by the fact that, under the present sulfiding conditions, the edges may not be simple terminations of the stoichiometric MoS₂, as depicted in figure 5.2.

At the S-edge, a Mo atom is coordinated to six sulfur atoms and is therefore saturated with S, as for a Mo atom in bulk MoS₂. At the Mo-edge, a Mo atom is only coordinated to four S atoms, and therefore either one or two S atoms per Mo atom can adsorb under sulfiding conditions, figure 5.17(b) and (c), respectively. In both cases, a Mo atom at the Mo-edge achieves a sulfur coordination of six. However, only the structure with one S atom per Mo edge atom results in S atoms which are shifted by half a lattice constant along the edge relative to the S atoms in the basal plane, as in the STM images. Thus, it is concluded that the model illustrated in figure 5.17(d) is the structure representing the observed edges of the MoS₂ triangles.

Density functional theory (DFT) calculations [24, 26, 61, 62] corroborate this picture. The calculations use an infinite one-dimensional chain-like model of MoS₂. Periodic boundary conditions are imposed, so the slab exposes one Mo-edge and one S-edge as well as the (0001) basal plane at the top and the bottom.

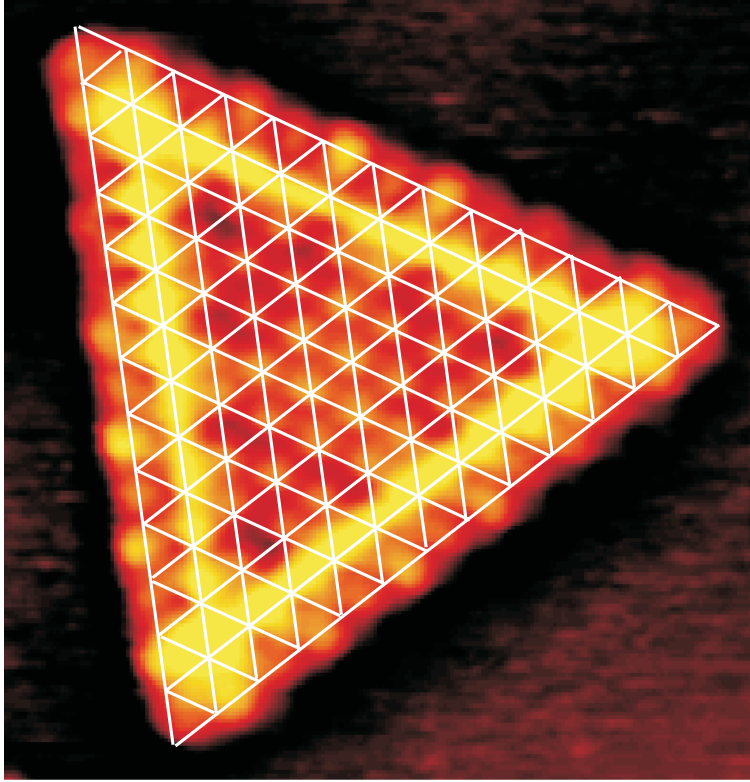


Figure 5.16: A grid indicating the lattice positions on the (0001) basal plane is superimposed on an atom-resolved STM image of a MoS_2 nanotriangle.

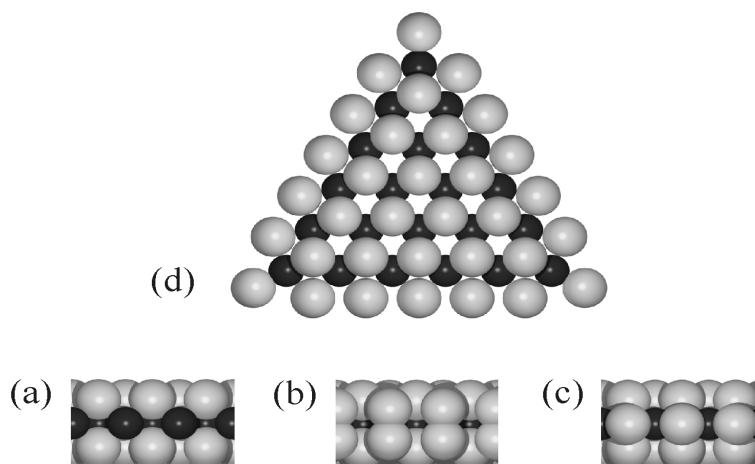


Figure 5.17: Ball models illustrating Mo-edges. (a)-(c) represent sideviews of Mo-edges. In (a), the naked Mo-edge in figure 5.2 is shown. A Mo atom (dark) is coordinated to only four S atoms (light). (b) The Mo-edge is terminated with two S atoms per Mo atom at the edge. According to the DFT calculations, a dimerization of the S atoms occurs [24, 26]. In (c), there is only one S atom per Mo atom at the edge. In this case, the S lattice at the Mo-edge is reconstructed with respect to the S lattice on the basal plane. The S atoms move vertically to the Mo plane and shift laterally with half a lattice constant. (d) A topview of (c). Model (c) and (d) depict the triangular structure observed in the STM images with the S atoms being out of registry with those on the basal plane of MoS_2 .

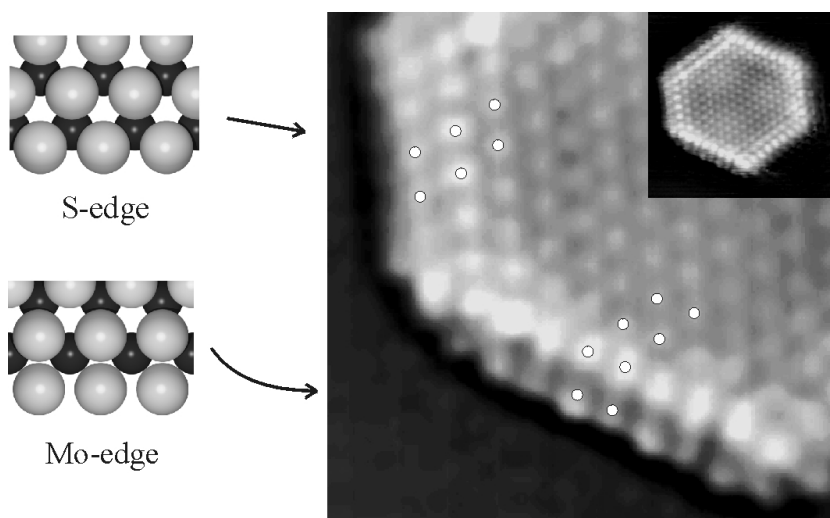


Figure 5.18: A hexagonal single-layer MoS_2 nanocrystal. The image is a cut-out from the insert. The Mo-edge is identified from the characteristic reconstructed edge structure. The ball models show topviews of the S-edge and the Mo-edge, respectively.

These DFT calculations show that the most stable structures at the Mo-edge are S saturated structures corresponding to the two models shown in figure 5.17 and that these structures have almost the same stability [24, 26, 62].

The sulfur-saturated Mo-edge is demonstrated to be the most stable type of edge termination. This is also in accordance with the suggestion in a recent DFT study [63]. The less stable S-edge termination does, however, appear in MoS_2 nanoclusters shaped as truncated triangles, pentagons or hexagons. Figure 5.18 depicts an atom-resolved STM image of a hexagonal MoS_2 cluster and a close-up on the two types of edges. From the dots superimposed in the image, the Mo-edge is clearly identified with the characteristic, reconstructed geometry. The neighbouring edge is thus an S-edge. The edge protrusions at the S-edge are found to be in registry with the basal plane. Assuming again that the edge protrusions reflect the position of S atoms, the sulfur lattice at the S-edge is a simple continuation of the bulk lattice, in accordance with the ball model in figure 5.3. A sideview is shown in figure 5.19(a). DFT calculations also find that a such

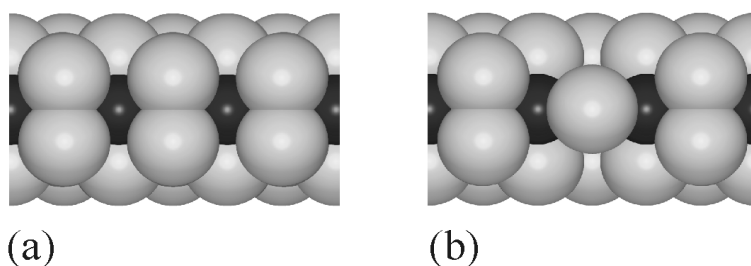


Figure 5.19: (a) A ball model representing a sideview of the S-edge in figure 5.3. S atoms are dimerized at the edges as in the calculated structures [24, 26]. (b) A single sulfur vacancy formed at the S-edge. The DFT calculations show that the remaining sulfur atom moves to the plane of the metal atoms.

saturated edge is the most stable structure at the S-edge under sulfiding conditions [24, 26, 62].

From the atom-resolved STM images, it is evident that there are more structural features at the MoS₂ edges which are not included in the geometrical model established above. Some of these structural details are illustrated in figure 5.20(d):

- A double periodicity of the sulfur atoms at the Mo-edge (scan (a)).
- Only an *odd* number of sulfur atoms is observed at the Mo-edges on the MoS₂ *triangles*. This is surprising, since the crystal structure of MoS₂ does not restrict this number. An *even* number of sulfur atoms is only observed on the Mo-edges if the MoS₂ crystallite is *non-triangular* (figure 5.22). In this latter case, no double periodicity of the sulfur atoms is found, indicating that the double periodicity is due to a geometric rather than an electronic effect.
- A bright brim running parallel to the Mo-edge. Scan (b) shows that the brim is associated with an apparent height increase of 0.3 Å relative to the S atoms in the basal plane lattice. The brim is located on the outermost S atoms on the basal plane lattice. A less intense bright brim is also observed at the S-edge (figure 5.18). This is the only additional structure on the S-edge.
- Behind the brim on the Mo-edge, a pairing of the S atoms is observed. The linescan (c) reveals that the S atoms are displaced laterally along the edge by 0.3 Å

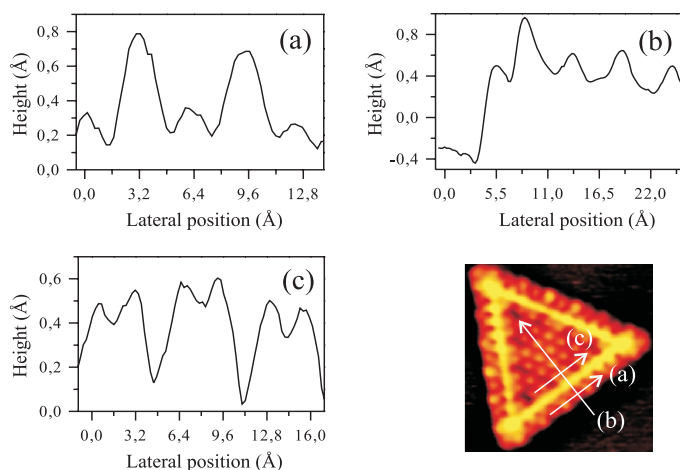


Figure 5.20: Linescans showing the detailed structure at the S saturated Mo-edge terminated MoS_2 triangle. (a) Linescan along the edge, (b) perpendicular to the edge, and (c) parallel to the edge behind the brim. The directions are indicated on the STM image.

To understand these structural features, an interplay with theoretical studies is currently in progress. More comprehensive DFT calculations are performed by M. Bollinger [54]. The aim is to obtain a detailed description of the electronic structure at the MoS_2 edges. In addition, the effect of the gold substrate, the corners on the clusters, and coadsorbed hydrogen on the edges are also included in the considerations. Hydrogen is present in the sulfidation procedure from the H_2S , and a partial hydrogenation of the MoS_2 edges has been observed by infrared spectroscopy [64].

From the preliminary calculations, it is found that surface electronic states are present at both the Mo- and S-edges, i.e. the electronic structure near the edges of the MoS_2 nanoclusters is different from bulk MoS_2 . These states account for the bright brims. At present, the influence of such localized edge states on the appearance of the edges in STM images is studied intensively.

5.2.6 Conclusion

In the past, it has been speculated that the MoS₂ clusters could exist in different shapes (hexagonal, truncated hexagonal, rhombohedral, etc.), but direct experimental evidence of such structures has been lacking [1]. Similarly, the lack of suitable experimental techniques to reveal the atomic-scale structure of the edges has led researchers to assume that the Mo and S atoms at the edges are located at the bulk-truncated atomic positions. The present STM results thus provide new insight into the morphology and catalytically important edge structures of MoS₂ nanoclusters. It has been shown that it is possible to synthesize MoS₂ nanoclusters and resolve their structure on the atomic scale. The first real-space images of the shape and edge structure of single-layer high MoS₂ nanocrystals are presented. It is concluded that under sulfiding conditions, the more stable edge termination is the Mo-edge saturated with S atoms in a reconstructed geometry.

5.3 Edge vacancies

In order to bind sulfur-containing molecules for further extrusion of the sulfur, it is generally believed that sulfur vacancies, i.e. coordinatively unsaturated metal sites, must be formed. Experimental and theoretical studies indicate that the basal plane of MoS₂ is inactive and that the vacancy formation is related to the edges of the catalyst particles [1, 24]. High pressures of hydrogen is used in the industrial process to strip off sulfur from the edges [1]. In the following, the first preliminary experiments to create such coordinatively unsaturated metal sites on the gold-supported MoS₂ nanoclusters are described.

5.3.1 Sulfur vacancy formation and structure

Sulfur vacancy formation by H₂ exposure is described by the overall reaction (5.1). Assuming equilibrium, a simple kinetic description provides an expression for the vacancy concentration at the edges:

$$\theta_{\star} = \frac{1}{1 + \frac{P_{H_2S}}{P_{H_2}} e^{E_S/kT}}, \quad (5.2)$$

where E_S is the energy cost for the vacancy formation, and P denotes the partial pressures of H₂S and H₂, respectively. This expression merely states

that a high vacancy concentration results in an environment of excess hydrogen, but only if the reaction is not too endothermic (or equivalently, if the temperature is high).

However, large hydrogen exposures up to 1100 L in a background pressure of 1.0×10^{-6} mbar with the sample kept at 673 K are found not to produce any sulfur vacancies. This could be due to the modest hydrogen pressure, which is at least thirteen orders of magnitude lower than that used under the industrial reaction conditions. Another possible explanation is the high dissociation energy of hydrogen, which is 4.52 eV/molecule [65]. Furthermore, the detailed mechanism in the vacancy formation involves a number of elementary steps such as dissociative adsorption of H_2 , diffusion of H atoms, so formation and desorption of H_2S can occur. Any of these steps could in principle inhibit the vacancy formation.

The energy involved in creating a S vacancy at Mo-edge is calculated within the DFT scheme to be $E_S \sim 0.6$ eV, which is a fairly high value. In order to surmount the corresponding reaction activation barrier, the sample is instead exposed to much more reactive atomic hydrogen. The predissociation of hydrogen and subsequent dosage is done by placing the sample in the vicinity of and with front against a hot tungsten filament in a background atmosphere of hydrogen (the chamber pressure is 1.0×10^{-6} mbar). As a result small doses of hydrogen atoms form [66].

After a such reductive treatment, neither the size nor the shape of the MoS_2 triangles are changed, i.e. neither sintering or reshaping occurs under the present conditions. However, atom-resolved images clearly demonstrate that sulfur vacancies are now formed at the edges. Typically one or two S atoms are stripped off, as illustrated in figure 5.21. From the STM images, the vacancies are found to be located on S sites along the reconstructed sulfur lattice at the Mo-edge (figure 5.17). The double periodicity and the brim at the edge, where the vacancies are formed, seem to have disappeared in figure 5.21. This is attributed to the close proximity of the two vacancies. The general observation is that the double periodicity as well as the brim structure are retained, although the brim intensity is reduced in the neighbourhood of a vacancy. Furthermore, the two sulfur-saturated edges in figure 5.21 demonstrate that the atomic hydrogen exposure does not alter the characteristic, structural features associated with this Mo-edge termination. Thus, it is likely that the STM are directly imaging catalytically active sites for the HDS reaction on the atomic-scale. Whether these vacancies are active or not, is still a question that remains to be answered. Adsorption experiments of simple test molecules are planned to study the reactivity of the MoS_2 clusters

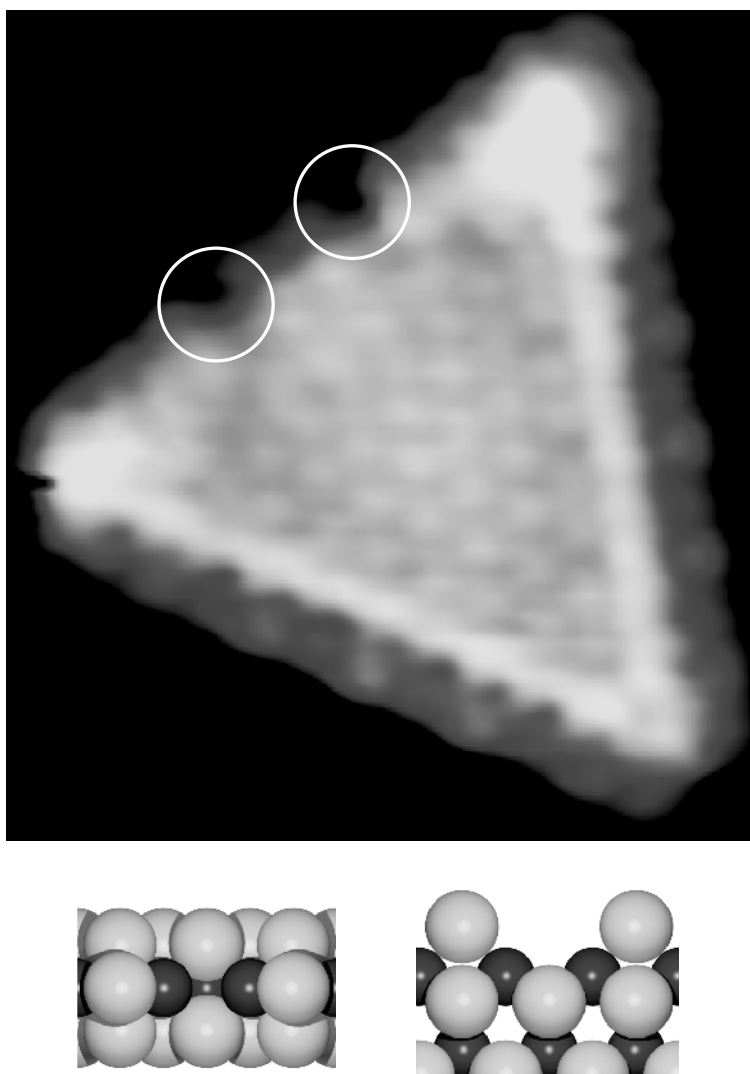


Figure 5.21: An atom-resolved STM image ($I_t = 1.12$ nA and $V_t = -8.5$ mV) of a single-layer MoS₂ nanocluster exposed to atomic hydrogen at 673 K. This treatment resulted in the formation of two S vacancies at the edges, indicated by the white circles. A model (a sideview and a topview) in which an S vacancy has been formed in the structure (d) in figure 5.17 is shown.

further.

It has been speculated that the CUS formation can be assisted by distortions of the edge lattice and that rapid edge diffusion can lead to agglomeration of sulfur vacancies [1]. From a sterical point of view, such vacancy clusters would be favourable for adsorption of larger organosulfur molecules. Under the present reductive conditions, the STM results show that (i) no severe distortions are introduced in clusters with S-vacancies, (ii) the vacancy diffusion is quenched at room temperature, and (iii) only isolated, single vacancies are observed.

On the S-edge, the reduction procedure does not introduce any structural changes, as seen in the STM images. The vacancy formation on the S-edge is apparently associated with a higher activation barrier compared with the Mo-edge. Recent DFT calculations indicate, however, that the sulfur binding energy is lower at the sulfur-saturated S-edge ($E_S \sim 0.1$ eV) than at the Mo-edge ($E_S \sim 0.6$ eV) [24, 26, 62], i.e. single sulfur vacancies (illustrated in figure 5.19) should be more easily formed on the S-edge (figure 5.19(b)) than on the Mo-edge (figure 5.17). On the other hand, these calculations also show that hydrogen adsorption at the S-edge resulting in the formation of SH groups are energetically even more favourable than the vacancy formation [24]. Thus, it is suggested that hydrogen stabilizes sulfur at the S-edge by the formation of SH groups. In the STM images, no structural changes are observed before and after hydrogen exposure. This could be due to the fact that hydrogen has already saturated the S-edge during the synthesis.

In conclusion, the model study has established a new picture of catalytically active sites in the form of sulfur vacancies at the MoS₂ edges. The vacancies are created only at the Mo-edge by *in situ* treatment with atomic hydrogen. It should be added that it still remains to be investigated whether these vacancy sites are active towards HDS.

5.4 CoMoS nanoclusters

In the most commonly used HDS catalysts, Co or Ni are added to increase the activity. It has been established that these promoter atoms are located at the edges of the MoS₂ crystallites. In this section, the catalyst model system consisting of gold-supported MoS₂ nanoclusters will be extended to include the Co-promoter atoms. The main finding in the present section is atomically resolved STM images of sulfided Co-Mo nanoclusters. These images reveal that an addition of Co to the well-characterized triangular

MoS₂ clusters induces a morphological transition into hexagonally truncated triangles, and it is found that Co-promoter atoms stabilize the S-edge termination. Based on the STM results, a structural model is proposed for the position of Co at the edges of single-layer CoMoS nanoclusters.

5.4.1 Preparation of CoMoS nanoclusters

Several approaches have been investigated in the attempt to synthesize sulfided Co-Mo nanoclusters. In this section, the procedure, which is found to be the more efficient in achieving the bimetallic sulfide phase, will be described. The standard preparation is used as a starting point in the synthesis. Initially, a core of sulfided molybdenum is produced by e-beam evaporating metallic Mo onto the Au(111) substrate while dosing gaseous H₂S. In this way MoS₂ embryos are formed, and the idea is subsequently to cap these nanoclusters with Co in order to facilitate edge substitution [47]. The herringbone pattern on Au(111) acts to disperse deposited Co into a regular array of islands with narrow size distribution, as observed for the deposition of Mo (figure 5.6). While maintaining the H₂S flux, Co and Mo are co-deposited onto the initial embryos confined on the Au(111) reconstruction template. The metal coverages are $\approx 10\%$ for Mo and $\approx 4\%$ for Co, respectively. Finally, the intermixed Co-Mo sulfide nanoclusters are crystallized by postannealing at 673K for 15 minutes in the H₂S atmosphere. Further experimental details are described in section 5.2.1.

5.4.2 Cluster structures

STM images show that the co-deposition of Co and Mo in H₂S and the subsequent crystallization result in two phases: (1) large cobalt sulfide islands formed by a step flow growth mode at the Au(111) step edges (figure 5.22), and (2) crystalline CoMoS nanoclusters formed on the Au(111) terraces (figure 5.23). The STM images in figure 5.22 show (a) a large island grown at a Au(111) step edge together with (b) an atom-resolved image. This type of island structures are associated with a cobalt sulfide phase, since the same structures are observed when *only* Co is deposited and subsequently sulfided on Au(111). Cobalt sulfide exists in a multitude of phases with different stoichiometry and crystallographic structure, e.g. CoS, CoS₂, Co₃S₄ or Co₉S₈. The latter is the thermodynamically most stable cobalt sulfide under typical HDS reaction conditions. A detailed characterization of the observed cobalt sulfide phase has not yet been performed.

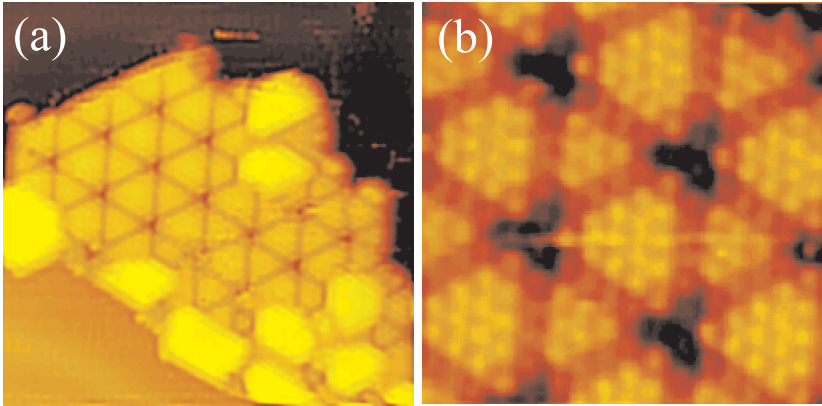


Figure 5.22: (a) An STM image ($152 \times 186 \text{Å}^2$) showing a large cobalt sulfide island formed at a Au(111) step edge. The small, bright clusters are assigned to encapsulated MoS_2 crystallites. (b) A close-up on a cobalt sulfide island ($50 \times 54 \text{Å}^2$).

The following discussion will address the structure of the nanoclusters formed on the Au(111) terraces. The main new finding is that the nanoclusters are predominantly shaped as *hexagonally truncated triangles* (figure 5.23) as opposed to the *equilateral triangles* of MoS_2 (figure 5.8). This change in morphology is attributed to the incorporation of cobalt in the MoS_2 structure, and it is suggested that the resulting hexagonally truncated triangles are associated with a Co-MoS_2 , or equivalently, a CoMoS phase.

Atomically resolved STM images of the CoMoS cluster (figure 5.24) reveal that protrusions on the basal plane are arranged in a hexagonal symmetry with a lattice spacing of $3.15 \pm 0.10 \text{Å}$. This is again identical to the (0001) basal plane of the MoS_2 nanocrystals. The height of the clusters is $2.1 \pm 0.3 \text{Å}$, corresponding to the height of a single-layer MoS_2 slab. Thus, it is concluded that the internal structure of the CoMoS clusters corresponds to that of single-layer MoS_2 .

The hexagonal morphology implies that both the Mo-edge and the S-edge terminations are present in the CoMoS cluster in figure 5.24. The identity of the two types of edges in the CoMoS clusters is inferred from atom-resolved STM images. At the longer edges, the protrusions are *out* of registry with the protrusions on the basal plane. As in the case of

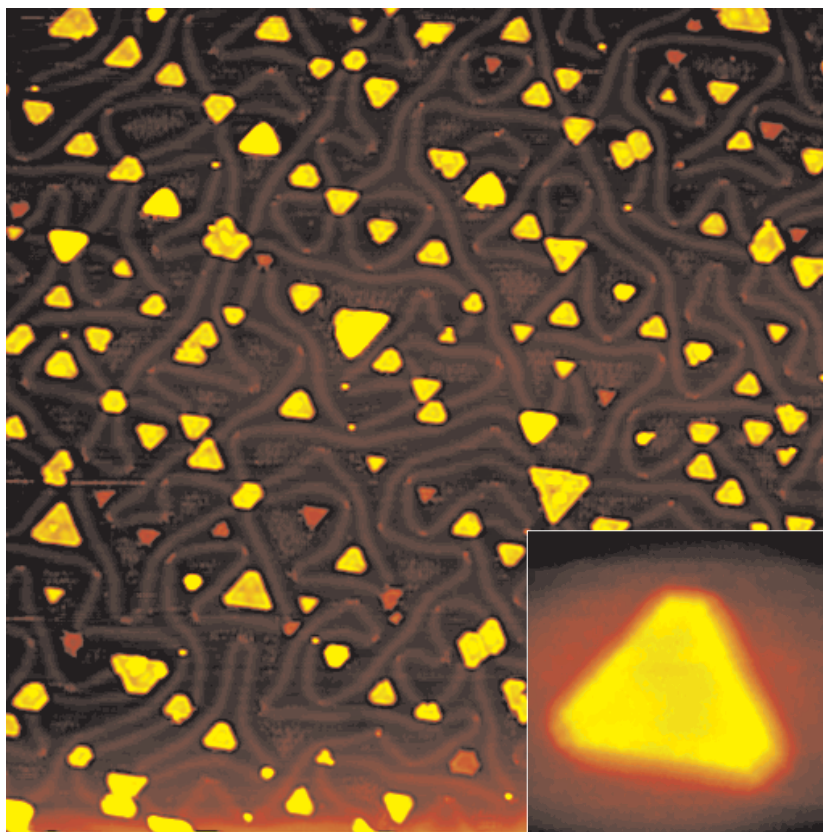


Figure 5.23: An STM image ($969 \times 1057 \text{Å}^2$) showing sulfided Co-Mo clusters on Au(111) annealed to 673 K. The insert shows a close-up ($68 \times 74 \text{Å}^2$) on the predominant structure on the terraces, the hexagonally truncated triangle. This cluster shape constitutes a total of 70% of the crystalline nanoclusters. The mean cluster size is $\sim 700 \text{Å}^2$.

the MoS₂ triangles, these edges are associated with Mo-edges where the S atoms are arranged in the reconstructed geometry. The Co-promoter atoms thus appear to have little effect on the Mo-edges. The short edges are S-edges, according to the MoS₂ crystal structure. Adapting again the simple assumption that protrusions reflect the positions of S atoms, superimposed grids reveal that sulfur atoms at the S-edges are *in* registry with the S atoms in the basal plane. The S atoms, however, appear to be displaced ~ 0.5 Å perpendicularly away from the S-edges compared to the bulk-truncated positions. Thus, it is concluded that addition of cobalt stabilizes the S-edges relative to the situation of pure MoS₂ triangles. Based on a Wulff-type construction argument, the ratio of the free edge energies for the CoMoS nanoclusters γ_S/γ_{Mo} is found to lie in the range from 1.3 to 1.7, under the present sulfiding conditions.

5.4.3 Model for the CoMoS clusters

Is it possible from the atom-resolved STM images to determine where the cobalt atoms are located in the CoMoS nanoclusters? The bright brim structure behind the outermost rows of sulfur atoms at the S-edges appears very intense on the CoMoS cluster, as compared to the S-edges in pure MoS₂ nanocrystals (figure 5.18). The large apparent height of ~ 1.0 Å of the brims relative to the basal plane is tentatively attributed to a change in the electronic structure caused by Co atoms being substituted at the S-edges, as indicated in the ball model in figure 5.25. There appears to be no difference in the way the Mo-edges are imaged for the CoMoS clusters compared to the MoS₂ clusters, which further supports the picture that Co is substituted into, and thus only stabilizes the S-edges. In figure 5.24, three very bright (~ 1.0 Å) spots are observed to be arranged in a triangular symmetry on the basal plane of the CoMoS clusters. The three bright spots are found to occupy the positions of basal plane sulfur atoms. This strongly suggests that a single Co impurity has substituted a Mo atom within the basal plane, and again induces an enhanced electron density at the three neighbouring sulfur atoms, which are consequently imaged brighter. A similar triangular defect structure has been investigated theoretically on the (0001) surface of bulk MoS₂ in the case of substitution with donor atoms having a larger number of valence electrons than Mo (e.g. Co) [67].

Based on the present STM observations, a structural model is proposed for the cobalt-substituted S-edge, as depicted in the ball model in figure 5.25. In the model, Co atoms are substituted into Mo positions at the S-edge. A *tetrahedral* environment of Co is produced if the outermost S

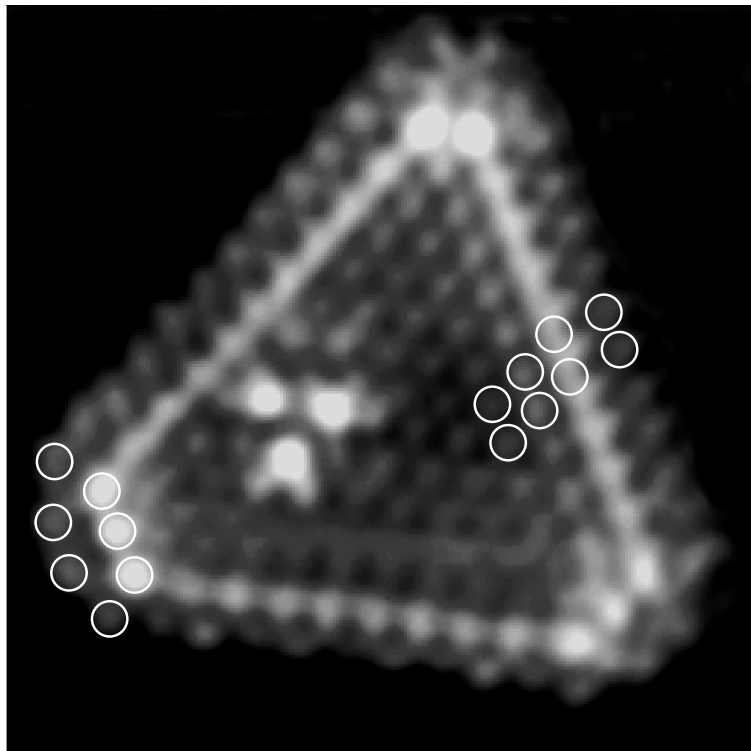


Figure 5.24: An atom-resolved STM image of a CoMoS nanocluster. The circles indicate the positions of S atoms. The mean lengths are $\sim 30 \text{ \AA}$ of the Mo-edge and $\sim 12 \text{ \AA}$ of the S-edge, respectively. Size $48 \times 53 \text{ \AA}^2$. $I_t = 1.95 \text{ nA}$ and $V_t = -430 \text{ mV}$. Notice that a double period is associated with the the lower Mo-edge, where the number of S atoms is odd, as in figure 5.9. At the two other Mo-edges, the number of S atoms is even, and these edges do not exhibit a double period.

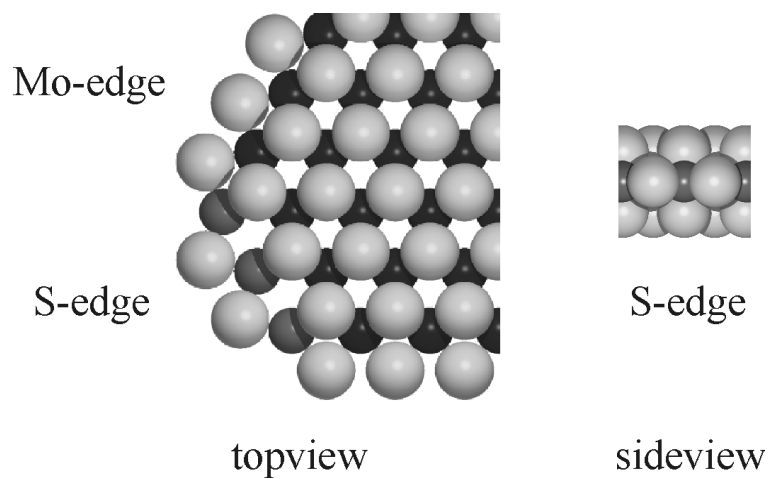


Figure 5.25: A ball model of the proposed CoMoS edge structure. A topview of one corner of the cluster is shown to the left. A sideview of the Co substituted S-edge is shown to the right. Color code: Mo (black), Co (dark grey) and S (light grey).

atoms are assumed to be monomer sulfur atoms, as is the case for the Mo-edge. It is likely that the Co relaxes slightly away from the substitutional Mo positions. This could explain why the monomer sulfur atoms are seen to be slightly displaced outwards perpendicular to the edge in the STM image (Fig. 3(c)). The possibility that only a fraction of the Mo atoms on the S-edge are replaced by Co atoms is excluded on the basis of STM images showing clusters with longer S-edges (up to 6 atoms wide). In these images, an edge structure with a periodicity of only one lattice constant is observed, indicating that the edge is fully substituted by Co.

This model is consistent with other spectroscopy data on supported CoMoS structures. From *in situ* Extended X-ray Absorption Fine Structure (EXAFS) spectroscopy and Mössbauer Emission Spectroscopy (MES) measurements, the local environment of substituted Co atoms has previously been inferred. It is shown that the average coordinations are $N_{Co-S} \approx 5$ and $N_{Co-Mo} \approx 2$. Similarly, the average distances from Co to the nearest neighbour atoms are determined to be $d_{Co-S} \approx 2.2$ Å and $d_{Co-Mo} \approx 2.9$ Å [1]. In the literature, a structural model of CoMoS in which Co atoms are substituted on the Mo-edge in a tetragonal, pyramidal-like geometry has been favored [1]. This configuration is ruled out on the basis of the STM images, since Co is seen to exclusively affect the S-edge, where the tetragonal, pyramidal-like is not likely to occur.

The position of promoter atoms in CoMoS has also been treated in theoretical studies using DFT calculations [24, 68]. These studies are inspired by the EXAFS and MES measurements quoted above. In both DFT studies it is concluded that Co substitution of Mo on the S-edge is energetically favorable, in agreement with the present experimental observations.

From studies of the industrial HDS catalyst, it is found that part of the Co forms a Co_9S_8 phase, which is the thermodynamically most stable configuration of cobalt sulfide under typical reaction conditions. The formation of the promoted, active phase of Co, Mo and S may therefore be impeded, resulting in a loss of activity. Similarly, it is also observed that the phase separation of the sulfides of Co and Mo is very pronounced under UHV conditions. Whereas MoS_2 is formed in small clusters highly dispersed on the terraces, the cobalt sulfide preferentially grows by step flow in large islands at the Au(111) step edges. In the presence of S, Co is apparently much more mobile on the surface than Mo, and it is likely that the apparent immiscibility of the separate sulfides impedes the formation of CoMoS. In section 4, it is speculated that the step flow growth involves the creation of highly diffusive cobalt-sulfide complexes.

In conclusion, no direct knowledge of the morphology and edge ter-

minations in the cobalt-promoted catalyst has been available until now. This section reports the synthesis of a model system consisting of cobalt-substituted single-layer MoS₂ clusters that are associated with a CoMoS phase. A model suggesting the position of the Co-promoter atoms is presented on the basis of atom-resolved STM images, which provide the first detailed real space pictures of a CoMoS structure.

5.5 Summary and outlook

This chapter has demonstrated a new way of obtaining detailed atomic-scale information of model systems, which are of interest in HDS catalysis. MoS₂ or CoMoS nanoclusters, single-layer in height and $\sim 30\text{\AA}$ wide, are synthesized using Au(111) as a template. The clusters are characterized by STM, providing insight into the morphology (shape) and the detailed edge structures of the nanoparticles.

The catalytically important edge structures of the MoS₂ particles are found to deviate from simple continuations of the bulk crystal. An interplay with theoretical studies indicates that some of the structural features at the edges, as observed by STM, are due to localized electronic states. Such states may be important for the activity and selectivity of the HDS catalyst particles. This has not previously been emphasized.

Preliminary experiments have been performed in order to elucidate the catalytic properties of the model systems. An *in situ* treatment with atomic hydrogen creates S vacancies at the Mo-edges of the MoS₂ nanoclusters. Such sites are interesting since they are believed to be the active elements in HDS catalysis. The results motivate further studies. The promoting effect of Co substituted into the edges of MoS₂ is expected to increase the number of S vacancies under reductive conditions. If this is the case for the CoMoS model system, will S vacancies form at the S-edges or does Co act by destabilizing the S atoms on the Mo-edges? Furthermore, what is the preferred adsorption site for simple S-containing molecules like thiophene (C₄H₄S)? Do they attach at the S vacancies? STM studies are currently intensively pursued to address such fundamental questions, and it is the hope that these efforts will shed more light on elementary processes in the desulfurization reactions.

It would also be interesting to perform reactivity measurements in batch flow reactors, as demonstrated by Niemantsverdriet and co-workers [31], in order to demonstrate that the model systems are really catalytically active. In this respect, it is important to notice that the cluster

morphology in the MoS₂ and CoMoS model systems may change under reaction conditions, where the clusters are exposed to high gas pressures. Recently, a high pressure STM with the ability to scan surfaces *in situ* in gas atmospheres up to ~ 1 atm has been developed in our laboratory [69]. This equipment would be useful in studying the cluster morphology when the HDS model systems are exposed to more realistic reaction atmospheres than the present UHV conditions. Finally, the influence of the substrate should also be considered. Usually, a highly porous γ -Al₂O₃ is used as a support in the industrial HDS catalysts. There is a large expertise in our group on STM studies of metal clusters on thin Al₂O₃ film, grown on-top of NiAl(110) [70]. If the sulfide model systems can be synthesized on this flat oxide support, it provides a way of reducing the material gap.

The present results are also interesting from a more general point of view. Up to now there has been much focus on metal and semiconductor nanoclusters, whereas the knowledge about transition metal sulfide nanoclusters is limited. These clusters are, besides as catalysts, important as, e.g., lubricants [71, 72] and models of the active parts of some enzymes [73]. The approach presented here demonstrates a new way of obtaining atomic-scale information on inorganic clusters deposited on conducting substrates and should in general be applicable to other cluster systems.

References

- [1] H. Topsøe, B. S. Clausen, and F. E. Massoth, in *Hydrotreating Catalysis, Science and Technology, vol. 11*, edited by J. R. Anderson and M. Boudart (Springer Verlag, Berlin, 1996).
- [2] H. Topsøe, K. G. Knudsen, L. S. Byskov, J. K. Nørskov, and B. S. Clausen, *Studies in Surface Science and Catalysis* **121**, 13 (1999).
- [3] J. W. Gosselink, *CATTECH* **2**, 127 (1998).
- [4] E. G. Derouane, *CATTECH* **3**, 104 (1999).
- [5] *Chemical & Engineering News* **78**, 40 (2000).
- [6] L. S. Byskov, PhD thesis, Technical University of Denmark, Denmark, 1999.
- [7] R. Prins, V. H. J. de Beer, and G. A. Somorjai, *Catal. Rev.-Sci. Eng.* **31**, 1 (1989).
- [8] R. Prins, in *Hydrotreating reactions in Handbook of Heterogenous Catalysis*, edited by G. Ertl, H. Knözinger, and J. Weitkamp (VHC Verlagsgesellschaft mbH, Weinheim, 1997).
- [9] R. R. Chianelli and M. Daage, *Advances in Catalysis* **40**, 177 (1994).
- [10] J. Grimbolt, *Catalysis Today* **41**, 111 (1998).
- [11] D. D. Whitehurst, T. Isoda, and I. Mochida, *Advances in Catalysis* **42**, 345 (1998).
- [12] T. G. Parham and R. P. Merrill, *J. Catal.* **85**, 295 (1984).
- [13] B. S. Clausen, H. Topsøe, R. Candia, J. Villadsen, B. Lengeler, J. Als-Nielsen, and F. Christensen, *J. Phys. Chem.* **85**, 3868 (1981).
- [14] J. A. Wilson and A. D. Yoffe, *Adv. Phys.* **18**, 193 (1969).
- [15] R. G. Dickinson and L. Pauling, *J. Am. Chem. Soc.* **45**, 1466 (1923).
- [16] H. Topsøe and B. S. Clausen, *Catal. Rev.-Sci. Eng.* **26**, 395 (1984).
- [17] T. F. Hayden and J. A. Dumesic, *J. Catal.* **103**, 366 (1987).
- [18] S. J. Tauster, T. A. Pecoraro, and R. R. Chianelli, *J. Catal.* **63**, 515 (1980).

- [19] M. Salmeron, G. A. Somorjai, A. Wold, R. R. Chianelli, and K. S. Liang, *Chem. Phys. Lett.* **90**, 105 (1982).
- [20] M. Daage and R. R. Chianelli, *J. Catal.* **149**, 414 (1994).
- [21] H. Topsøe, R. Candia, N.-Y. Topsøe, and B. S. Clausen, *Bull. Soc. Chim. Belg.* **93**, 783 (1984).
- [22] C. J. H. Jacobsen, E. Törnqvist, and H. Topsøe, *Catal. Lett.* **63**, 179 (1999).
- [23] J. K. Nørskov, B. S. Clausen, and H. Topsøe, *Catal. Lett.* **13**, 1 (1992).
- [24] L. S. Byskov, J. K. Nørskov, B. S. Clausen, and H. Topsøe, *J. Catal.* **187**, 109 (1999).
- [25] C. Wivel, R. Candia, B. S. Clausen, S. Mørup, and H. Topsøe, *J. Catal.* **68**, 453 (1981).
- [26] L. S. Byskov, B. Hammer, J. K. Nørskov, B. S. Clausen, and H. Topsøe, *Catal. Lett.* **47**, 177 (1997).
- [27] G. A. Somorjai, *Catal. Lett.* **15**, 25 (1992).
- [28] J. A. Rodriguez, S. Y. Lin, J. Hrbek, H. H. Huang, and G.-Q. Xu, *J. Phys. Chem.* **100**, 14476 (1996).
- [29] J. P. G. Clark and C. M. Friend, *J. Chem. Phys.* **111**, 6991 (1999).
- [30] J. G. Kushmerick and P. S. Weiss, *J. Chem. Phys.* **102**, 10094 (1998).
- [31] A. M. de Jong, V. H. J. de Beer, J. A. R. van Veen, and J. W. Niemantsverdriet, *J. Vac. Sci. Technol. A* **15**, 1592 (1997).
- [32] J. C. Muijsers, T. Weber, R. M. van Hardeveld, H. W. Zandbergen, and J. W. Niemantsverdriet, *J. Catal.* **157**, 698 (1995).
- [33] A. M. de Jong, V. H. J. de Beer, J. A. R. van Veen, and J. W. Niemantsverdriet, *J. Phys. Chem.* **100**, 17722 (1996).
- [34] M. J. Bozack, L. Muehlhoff, J. N. Russell, W. J. Choyke, and J. T. Yates, *J. Vac. Sci. Technol. A* **5**, 1 (1987).
- [35] B. Hammer and J. K. Nørskov, *Nature* **376**, 238 (1995).
- [36] J. V. Barth, H. Brune, G. Ertl, and R. Behm, *Phys. Rev. B* **42**, 9307 (1990).

- [37] D. D. Chambliss, R. J. Wilson, and S. Chiang, *Phys. Rev. Lett.* **66**, 1721 (1991).
- [38] D. D. Chambliss, R. J. Wilson, and S. Chiang, *J. Vac. Sci. B* **9**, 933 (1991).
- [39] J. A. Strocio, D. T. Pierce, R. A. Dragoset, and P. N. First, *J. Vac. Sci. Technol. A* **10**, 1981 (1992).
- [40] B. Voigtländer, G. Meyer, and N. M. Amer, *Phys. Rev. Lett.* **44**, 10354 (1991).
- [41] A. W. Stephenson, C. J. Baddely, M. S. Tikhov, and R. M. Lambert, *Surf. Sci.* **398**, 172 (1998).
- [42] R. J. Needs, M. J. Godfrey, and M. Mansfield, *Surf. Sci.* **242**, 215 (1991).
- [43] V. Fiorentini, M. Methfessel, and M. Scheffler, *Phys. Rev. Lett.* **71**, 1051 (1993).
- [44] J. Jacobsen, K. W. Jacobsen, and J. K. Nørskov, *Surf. Sci.* **317**, 8 (1994).
- [45] S. Narasimhan and D. Vanderbilt, *Phys. Rev. Lett.* **69**, 1564 (1992).
- [46] A. J. Leavitt and J. T. P. Beebe, *Surf. Sci.* **314**, 23 (1994).
- [47] A. Christensen, A. V. Ruban, P. Stoltze, K. W. Jacobsen, H. L. Skriver, and J. K. Nørskov, *Phys. Rev. B* **56**, 5822 (1997).
- [48] W. G. Cullen and P. N. First, *Surf. Sci.* **420**, 53 (1999).
- [49] M. Weimer, J. Kramar, C. Bai, and J. D. Baldeschwieler, *Phys. Rev. B* **37**, 4292 (1988).
- [50] S. N. Magonov and M.-H. Whangbo, *Adv. Mater.* **5**, 355 (1994).
- [51] K. Kobayashi and J. Yamauchi, *Phys. Rev. B* **51**, 17085 (1995).
- [52] A. Altibelli, C. Joachim, and P. Sautet, *Surf. Sci.* **367**, 209 (1996).
- [53] K. K. Kam and B. A. Parkinson, *J. Phys. Chem* **86**, 463 (1982).
- [54] M. Bollinger, private communication.
- [55] G. Wulff, *Z. Kristallogr.* **34**, 449 (1901).

- [56] W. K. Burton, N. Cabrera, and F. C. Frank, *Trans. R. Soc. A* **243**, 299 (1951).
- [57] W. L. Winterbottom, *Acta Metallurgica* **15**, 303 (1967).
- [58] F. Grey and J. Bohr, *Europhys. Lett* **18**, 717 (1992).
- [59] L. Margulis, G. Salitra, R. Tenne, and M. Talianker, *Nature* **365**, 113 (1993).
- [60] G. Seifert, H. Terrones, M. Terrones, G. Jungnickel, and T. Frauenheim, *Phys. Rev. Lett.* **85**, 146 (2000).
- [61] P. Raybaud, J. Hafner, G. Kresse, and H. Toulhoat, *Surf. Sci.* **407**, 237 (1998).
- [62] P. Raybaud, J. Hafner, G. Kresse, S. Kasztelan, and H. Toulhoat, *J. Catal.* **189**, 129 (2000).
- [63] L. S. Byskov, J. K. Nørskov, B. S. Clausen, and H. Topsøe, *Catal. Lett.* **64**, 95 (2000).
- [64] N.-Y. Topsøe and H. Topsøe, *J. Catal.* **139**, 641 (1993).
- [65] *CRC Handbook of Chemistry and Physics*, 72 ed., edited by D. R. Lide (CRC Press, Boston, USA, 1991).
- [66] K. H. Rieder and W. Stocker, *Phys. Rev. Lett.* **57**, 2548 (1986).
- [67] M.-H. Whangbo, J. Ren, S. N. Magonov, H. Bengel, B. A. Parkinson, and A. Suna, *Surf. Sci.* **326**, 311 (1995).
- [68] P. Raybaud, J. Hafner, G. Kresse, S. Kasztelan, and H. Toulhoat, *J. Catal.* **190**, 128 (2000).
- [69] E. Lægsgaard, P. Thostrup, L. Österlund, P. B. Rasmussen, I. Stensgaard, and F. Besenbacher, in preparation.
- [70] K. H. Hansen, T. Worren, S. Stempel, E. Lægsgaard, M. Bäumer, H.-J. Freund, F. Besenbacher, and I. Stensgaard, *Phys. Rev. Lett.* **83**, 4120 (1999).
- [71] T. Spalvins, *J. Vac. Sci. Technol. A* **5**, 212 (1987).
- [72] L. Rapoport, Y. Bilik, Y. Feldman, M. Homyonfer, S. R. Cohen, and R. Tenne, *Nature* **387**, 791 (1997).

- [73] E. I. Stiefel, in *Transition Metal Sulfur Chemistry, Biological and Industrial Significance*, edited by E. I. Stiefel and K. Matsumoto (ACS symposium series 653, Washington DC, USA, 1995).

Chapter 6

Dansk resumé

Denne afhandling omhandler en række eksperimentelle undersøgelser vedrørende fundamentale aspekter af heterogen katalyse. Det beskrevne arbejde er udført i STM-gruppen på Institut for Fysik og Astronomi ved Aarhus Universitet. I dette kapitel vil afhandlingens hovedresultater blive opsummeret, og den sammenhæng, de indgår i, vil blive uddybet for læsere uden indgående kendskab til katalyse og overfladefysik.

Begrebet katalyse blev indført i 1835 af den svenske kemiker Berzelius for at beskrive kemiske reaktioner, hvis reaktionshastighed forøges ved tilstedeværelsen af en substans, som ikke forbruges under selve reaktionen. Den teknologiske anvendelse af dette fænomen er steget markant op igennem det 20. århundrede, så katalyse i dag spiller en afgørende rolle for samfundsøkonomien. Den kemiske industri og olieraffinering er i høj grad baseret på anvendelsen af katalysatorer, og i den senere tid har katalysen fundet yderligere anvendelse indenfor eksempelvis bioteknologi samt i løsningen af energi- og miljøproblemer. Dette bevirker, at der i øjeblikket satses meget på både anvendt og grundvidenskabelig forskning i katalyse.

I langt de væsentligste af de ovenfor omtalte områder katalyseres en gasfase reaktion på overfladen af et fast stof (heterogen katalyse). Oftest foregår de katalytiske reaktioner under ekstreme betingelser i reaktorer med tryk op til flere hundrede bar og ved temperaturer op til flere hundrede grader celcius. De heterogene katalysatorer er typisk komplekse materialer, bestående af porøse piller med et højt overfladeareal ($\sim 100 \text{ m}^2/\text{g}$). På overfladen af disse "bærer"-materialer imprægneres det aktive katalysatormateriale (f. eks. et metal) i form af partikler med en udstrækning af størrelsesordenen en nanometer (figur 1.1(a)), hvormed det aktive overfladeareal

maksimeres. Denne kompleksitet af katalysatorerne besværliggør en detaljeret karakterisering af katalytiske reaktioner og forklarer også, hvorfor katalysatorudviklingen hovedsageligt er baseret på empiri.

Selvom katalysatorteknologien har været etableret i årtier, er det kun grundet de senere års udvikling af eksperimentelle og teoretiske metoder i overfladevidenskab, at en detaljeret forståelse af de overfladeprocesser, der udgør de basale reaktioner i katalytiske processer, er muliggjort. En katalytisk reaktion forløber ved, at molekyler fra gasfasen adsorberer på den faste overflade (figur 1.1(b)). Bindinger i de adsorberede molekyler brydes måske herved. Adsorbaterne diffunderer rundt på katalysatorens overflade, og kan, når de mødes, danne de ønskede produkter, som til sidst desorberer fra overfladen. Når energibarrieren for de enkelte trin langs reaktionsvejen på overfladen er mindre end energibarrieren for den direkte reaktion i gasfasen, betegnes reaktionen som værende katalyseret.

Der er i øjeblikket en meget livlig international aktivitet omkring fundamentale studier af sådanne elementære processer i vekselvirkningen mellem gasser og faste overflader. Det er i denne sammenhæng arbejdet i denne afhandling indgår. Studierne er grundvidenskabelige og bidrager til de samlede bestræbelser på at etablere en detaljeret forståelse af heterogene katalyse.

Eksperimenterne, som er beskrevet i afhandlingen, er udført under yderst idealiserede forhold på overfladerne af perfekte enkelt-krystaller under ultra højt vakuum, for dermed at have kontrol med strukturen og renheden af de undersøgte overflader. Den eksperimentelle teknik, som overvejende er anvendt i undersøgelserne, er skanning tunnel mikroskopet (STM). Med dette mikroskop udmåles en overflades konturer ved at scanne en uhyre spids nål over overfladen. En nøjere beskrivelse af mikroskopets virkemåde udelades her! Det væsentlige er, at mikroskopet muliggør en afbildning af overflader med en så høj opløsning, at strukturer og processer kan studeres på det atomare niveau.

Afhandlingen omfatter STM studier indenfor tre forskellige emner. I den resterende del af kapitlet vil hvert enkelt emne kortfattet blive diskuteret, og hovedresultaterne opsummeres.

Det første emne, som er beskrevet i kapitel 3, drejer sig om ilt adsorption på Pt(110)-(1×2) overfladen (figur 3.1). Platin er et af de mest benyttede metaller i katalysatorer. Eksempelvis er platin en af de aktive bestanddele i bilkatalysatorer, hvor CO oxideres til CO₂, og NO_x reduceres til N₂. Iltets vekselvirkning med platin er et væsentligt led i disse reaktioner, og et indgående kendskab til ilt adsorption på platin overflader er derfor nødvendigt for at opnå en detaljeret forståelse af selv så simple

reaktioner. Kapitlet beskriver de strukturer, som frembringes ved den dissociative adsorption af ilt. Med STM observeres en mængde strukturer, der udviser en så høj grad af kompleksitet, at kun et tæt samspil med teoretiske DFT studier har muliggjort at etablere et mikroskopisk billede. Et af resultaterne er, at en meget tæt iltfase kan dannes (figur 3.13). Dette er overraskende, eftersom O atomer normalt vekselvirker repulsivt på metal overflader resulterende i lave mætningskoncentrationer af ilt. Årsagen, til at Pt(110)-(1×2) overfladen kan stabilisere den tætte iltfase, er, at Pt atomer relaxerer ud af overfladen. Dette påvirker overfladens elektroniske struktur, så iltatomerne binder kraftigere til overfladen, og O-O frastødningen dermed effektivt reduceres. Disse forskydninger af Pt atomerne giver i STM billederne anledning til lyse striber langs Pt-rækkerne i overfladen (figur 3.2). Grundet langtrækkende vekselvirkninger mellem striberne dannes spontant en nanostruktur med en udstrækning over en mesoskopisk længdeskala (figure 3.4). Disse resultater danner basis for videre studier af simple overfladereaktioner såsom oxidationen af CO til CO₂ og dannelsen af vand.

Foruden en høj reaktivitet af en katalysator, er det lige så væsentligt, at katalysatormaterialet er stabilt. Udskiftning af katalysatorer er ofte forbundet med store omkostninger. Under længerevarende brug eller meget ekstreme reaktionsbetingelser deaktiveres en katalysator. Dette kan ske ved, at katalysatorpartiklerne sintrer, d.v.s. gror, sammen til større partikler, hvorved aktivt overfladeareal effektivt mistes. Sintring afhænger kraftigt af den omgivne gasatmosfære, men den fundamentale viden herom er ret begrænset. For at komme en nærmere en forståelse, beskriver kapitel 4 et modelstudie af adsorbaters påvirkning af metal atomers diffusivitet på en overflade. Diffusionen af Pt adatomer pådampet den rene Pt(110)-(1×2) overflade har tidligere været studeret i detalje i gruppen og danner derfor et naturligt udgangspunkt for de nærværende undersøgelser. De pådampede Pt adatomer ligger i grøftene af overfladen (figur 4.1) og diffunderer endimensionalt frem og tilbage. Indsigt i diffusionsprocessen opnås ved at optage mange, hundredevis eller tusindvis, på hinanden følgende STM billeder af et område af overfladen med atomar opløsning. Når sådanne “STM-film”¹ efterfølgende afspilles, giver de et levende indtryk af de atomare processer, som foregår på overfladen, og de giver ydermere mulighed for at ekstrahere kvantitativ information om diffusionsprocessen. I eksperimenterne beskrevet i kapitel 4 lukkes brint ind i vakuumkammeret under optagelsen af STM-film. I filmene observeres det direkte, at adsorberet brint forøger Pt adatomernes diffusivitet ved dannelse af “lysere” Pt-

¹Eksempler på STM-film findes på: <http://www.ifa.au.dk/camp/stmoldpub.htm>

H komplekser (figur 4.3). Diffusiviteten af sådanne komplekser er forøget med to størrelsesordner sammenlignet med diffusiviteten af Pt adatomer på den rene overflade. Et kompleks beskrives som et Pt adatom med et brint atom adsorberet ovenpå. Dette billede er etableret ved at sammenholde resultaterne fra STM eksperimenter og DFT studier, og demonstrerer igen styrken i et sådant samspil.

Kapitel 5 drejer sig om STM studier af MoS₂ nanokrystaller på Au(111) overfladen som et modelsystem for afsvovlingskatalysatorer. Disse katalysatorer benyttes i olieindustrien til at fjerne svovl fra råolien. Ny miljølovgivning i det meste af den vestlige verden pålægger olieraffinaderierne at nedbringe svovlkoncentrationen i olieprodukter markant indenfor en kort årrække. For at nå denne målsætning skal nye og mere reaktive katalysatorer introduceres, og det giver anledning til en stor aktivitet i udforskningen af disse katalysatorer. Trods en enorm indsats, er en lang række fundamentale spørgsmål endnu ubesvaret. Det vides, at de aktive dele katalysatorerne består MoS₂ nanokrystaller med små mængder af Co atomer adderet til krystallitternes kanter for at forøge aktiviteten (figur 5.4). Desuden har man fundet ud af, at aktiviteten er relateret til netop disse kanter. Hvilken struktur kanterne har, hvordan strukturen ændres ved tilstedeværelsen af Co promoteratomer, og hvordan kantstrukturene er relateret til de katalytiske egenskaber, er spørgsmål, der diskuteres intenst i øjeblikket. For at få en sådan detaljeret indsigt, er STM benyttet til at studere modelsystemer for afsvovlingskatalysatorer. Ved at bruge den kemiske inerte Au(111) overflade som "bærer"-model, dannes MoS₂ nanokrystaller ved at deponere Mo på overfladen i en H₂S atmosfære. STM studier af nanokrystallerne har givet ny information vedrørende deres form og detaljerede kantstrukturer (figur 5.8 og 5.9). MoS₂ nanokrystallerne har en trekantet ligevægtsform under sulfiderende betingelser, og S atomerne på siderne af nanotrekanten er arrangeret i en rekonstrueret geometri (figure 5.17). Desuden er et model system for den Co promoterede katalysatorpartikel blevet dannet. I dette tilfælde ændrer MoS₂ partiklerne form (figur 5.24), og Co inkorporeres i kanterne som vist i figur 5.25. Tidligere har sådan strukturel information ikke været tilgængelig. Modelsystemerne lægger op til videre studier af elementære reaktioner i afsvovlingsprocessen. De første eksperimenter er udført og har givet en direkte indsigt i strukturen af S vakanser på kanterne (figur 5.21). Sådanne vakanser formodes at udgøre de positioner, hvor afsvovlingsprocessen sker.